



LUND UNIVERSITY

Deviations from the London model in superconductors

Campillo, Emma

2022

Document Version:

Publisher's PDF, also known as Version of record

[Link to publication](#)

Citation for published version (APA):

Campillo, E. (2022). *Deviations from the London model in superconductors*. Lund.

Total number of authors:

1

Creative Commons License:

Unspecified

General rights

Unless other specific re-use rights are stated the following general rights apply:

Copyright and moral rights for the publications made accessible in the public portal are retained by the authors and/or other copyright owners and it is a condition of accessing publications that users recognise and abide by the legal requirements associated with these rights.

- Users may download and print one copy of any publication from the public portal for the purpose of private study or research.
- You may not further distribute the material or use it for any profit-making activity or commercial gain
- You may freely distribute the URL identifying the publication in the public portal

Read more about Creative commons licenses: <https://creativecommons.org/licenses/>

Take down policy

If you believe that this document breaches copyright please contact us providing details, and we will remove access to the work immediately and investigate your claim.

LUND UNIVERSITY

PO Box 117
221 00 Lund
+46 46-222 00 00



Deviations from the London model in superconductors

EMMA CAMPILLO MUÑOZ

DEPARTMENT OF PHYSICS | FACULTY OF SCIENCE | LUND UNIVERSITY



Deviations from the London model in superconductors

By Emma Campillo Muñoz



LUND
UNIVERSITY

THESIS FOR THE DEGREE OF DOCTOR OF PHILOSOPHY

Thesis Advisors: Prof. Elizabeth Blackburn, Prof. Edward M. Forgan,

Dr. Rasmus Westerström

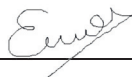
Faculty Opponent: Dr. Sebastian Mühlbauer

To be presented, with the permission of the Faculty of Science, Lund University, for public criticism in the Rydberg Lecture Hall at the Department of Physics on Friday, the 13th of May 2022 at 9:15.

Organization LUND UNIVERSITY Department of Physics Box 118 SE-221 00 LUND Sweden		Document name DOCTORAL DISSERTATION	
		Date of disputation 2022-05-13	
Author(s) Emma Campillo		Sponsoring organization	
Title and subtitle Deviations from the London model in superconductors			
Abstract <p>Using Small-Angle Neutron Scattering (SANS) we have studied the flux line lattices of the first heavy-fermion superconductor to be discovered, CeCu₂Si₂, the well-known high-temperature superconductor YBa₂Cu₃O_{7-x}, along with Ca-doped variants of this compound, and several topological superconductor candidates that have attracted a lot of attention in the last few years, such as PbTaSe₂, Au₂Pb and β-Bi₂Pd. Unconventional superconductors, with pairing mechanisms and properties that are not accounted for within BCS theory, are a subject of continuing interest. One example is heavy-fermion materials, in which the charge carriers respond as if they had a mass many times that of a free electron. We find that CeCu₂Si₂ shows a strong increase of scattered intensity from the flux lines as the applied magnetic field is increased towards the edge of the superconducting phase. In the standard theories, this intensity should drop steadily towards zero. This indicates that the superconductivity in this material is not destroyed by the same mechanism as in most all other superconductors but is instead destroyed by Pauli paramagnetic effects (PPE), which act to break up the Cooper pairs by favouring parallel alignment of the spins, increasing the relative strength of the magnetization in the vortex cores. This behaviour had previously been observed in CeCoIn₅. To better understand the behaviour of CeCu₂Si₂ and other Pauli limited superconductors, we present a physically-based expression for the size and magnetization of the vortex cores in Pauli-limited superconductors. For many years, high-temperature superconductors have attracted significant attention as they may be key for the use of superconductors in our everyday life. In the high-T_c superconductors, like YBa₂Cu₃O_{7-δ} (YBCO), the doping level can be used to tune the observed properties. Usually, δ is the doping control parameter in YBCO, which varies the occupancy of the oxygen chains running along the b-axis of the crystal. The (<i>d</i>-wave) superconductivity in YBCO develops primarily from the CuO₂ planes, but <i>s</i>-wave superconductivity also develops from the chains, which can be seen in the distortion of the vortex lattice. We study the temperature and field dependence of this anisotropy and SANS intensity from the vortex lattice up to 25 T using a newly developed formula for SANS time-of-flight (TOF) experiments. Furthermore, we can dope the yttrium site with calcium instead, resulting in a higher hole concentration than fully over-doped YBCO, pushing the field scale down closer to the magnetic fields we can apply in experiment. We include in this work some of the specific effects of doping YBCO with calcium and how it lowers the characteristic critical fields. Topological materials have attracted a lot of attention due to their novel quantum states and their possible applications to quantum computation. A key property is the appearance of Majorana bound states in the vortex core. When the Bogoliubov quasiparticles associated with the superconducting state can be constructed as superpositions of electron and hole states such that the bound quasiparticle is its own anti-quasiparticle (i.e. a Majorana particle), in the bulk, these quasiparticles are dispersive Majorana fermions, and in the vortex core they lead to bound states that obey non-Abelian statistics, and can (in theory) be used as qubits. In this thesis we report SANS experiments performed on three different topological superconductor candidates, PbTaSe₂, Au₂Pb and β-Bi₂Pd. For the latter, we discuss the anisotropy of the vortex lattice and the temperature dependence of the SANS intensity by rotating the sample with respect to the magnetic field direction and shed some light on the superconducting gap nature of β-Bi₂Pd.</p>			
Key words superconductivity, neutron scattering, SANS, vortex lattice, condensed matter physics			
Classification system and/or index terms (if any)			
Supplementary bibliographical information		Language English	
ISSN and key title		ISBN 978-91-8039-207-5 (print) 978-91-8039-208-2 (pdf)	
Recipient's notes		Number of pages 101	Price
		Security classification	

I, the undersigned, being the copyright owner of the abstract of the above-mentioned dissertation, hereby grant to all reference sources the permission to publish and disseminate the abstract of the above-mentioned dissertation.

Signature



Date 2022-03-28

Deviations from the London model in superconductors

By Emma Campillo Muñoz



LUND
UNIVERSITY

A doctoral thesis at a university in Sweden takes either the form of a single, cohesive research study (monograph) or a summary of research papers (compilation thesis), which the doctoral student has written alone or together with one or several other author(s).

In the latter case the thesis consists of two parts. An introductory text puts the research work into context and summarizes the main points of the papers. Then, the research publications themselves are reproduced, together with a description of the individual contributions of the authors. The research papers may either have been already published or are manuscripts at various stages (in press, submitted, or in draft).

Cover illustration front: Illustration of different magnetic fields passing through a superconducting sample with a collage pictures taken at ILL, PSI and EXED/HFM.

Created by Andrea Navas Olivé.

Cover illustration back: Collage of pictures taken at ILL, PSI and EXED/HFM.

Created by Andrea Navas Olivé.

© 2022 Emma Campillo and the respective publishers.

Faculty of Science, Department of Physics, Division of Synchrotron Radiation Research

ISBN: 978-91-8039-207-5 (print)

ISBN: 978-91-8039-208-2 (pdf)

Printed in Sweden by Media-Tryck, Lund University, Lund 2022



A mis padres, a Adolfo y a María Leticia.

*La inspiración existe,
pero tiene que encontrarte trabajando.*

-Pablo Picasso-

Acknowledgements

I am writing these words the night before my submission, and, during this last week, thousands of memories have appeared on my mind. I am relieved I am writing these words on my laptop and not on paper; otherwise, everything would be covered by tears (of happiness, of course!). I apologize in advance if the acknowledgements are too long, but this journey has also been long.

First and foremost, I would like to acknowledge my supervisor, Elizabeth Blackburn. Someone once told me that when choosing a good PhD program, the project was not as important as choosing a good advisor. Now, I cannot agree more with this statement. Elizabeth, I have no words to thank everything you have done for me. Since I first moved to Birmingham, you have always cared about me, you always have nice words to calm me down in my worst moments, and you always have taken me seriously. You have helped me feel confident, not only as a researcher but also as a person. Thank you for trusting me, first in Birmingham and then moving to Lund. I can affirm, without a doubt, that completing this PhD with you has been one of the best decisions in my life.

My next words are for Ted Forgan, whose enthusiasm and passion for science are as big as his patience and energy. Even retired, you have been a crucial part of this thesis, and I cannot feel more grateful that you decided to dedicate your time to teaching me and to share your knowledge to pursue all the work reflected in this thesis. I am going to miss our Friday meetings and all your puns.

Both of you are perfect examples of how a good supervisor should be. I am proud to have been part of the Birmingham group and somehow inaugurated the new group in the Synchrotron Radiation Division. *Thank you* is a really tiny expression to express how grateful I feel.

It has been a great honour to be part of the Synchrotron Radiation Division. When

Acknowledgements

people ask me how I feel in my department, my answer always is lucky. It is so rewarding to be surrounded by a healthy atmosphere, and people are always happy to share fika and have a calm conversation. I would like to thank in particular to my co-supervisor, Rasmus Westerström, and the members of my group, Ahmed and Denis, for being excellent colleagues and helping me during my experiments (I'm not angry, I'm thinking!), Annika, for sharing our secret hot chocolates and Oskar, I do not doubt that your experience in Lund will be promising.

I would like to translate special thanks to Lingjia Shen. Lingjia, you have been like my big brother in science. After all your advice, after all the hours working together in experiments and after the world decided to go upside down, you became an important figure to me. I once heard someone say you'll go far, now I am sure you will. It has been really nice to have the chance to start in Sweden with you and, somehow, we are finishing this stage together. I wish you the best. (You are going to call me *guapi*, but I cannot read this without crying).

It is true that when I decided to move to Lund, I felt very lost, so I want to highlight all the work that Patrik Wirgin and Anne Petersson have done for me, replying to absolutely all my questions and solving any query I had. Also, thank you to the previous and current heads of the division for all the effort done, especially during these last two years. The good thing about completing the thesis in Lund is that you always feel surrounded by friends, so I want to send a big thanks to all my colleagues of the SLJUS division, especially to Hanna, Sandra, Virginia and Sanna, who have been one of my most important supports. You were always willing to help me, no matter what.

As an old member of the Condensed Matter Group in Birmingham, I would like to take this opportunity to thank all the people that helped me during my stay there. Thank you to Mingee Chung, Chris Muirhead, Gary Walsh, Michael Parkes, Jon Perris (definitely, science is magic that works!) and Mark Colclough, who transmitted to me his passion for teaching. I want to send a big thanks to Randeep and Erik, when you both explained to me what was needed to face this PhD even before starting it. You described what I wished to do for the next five years without knowing.

I am not only grateful for all the people I met at the universities but also for all the people I met during experiments. ILL and PSI have been my second home and the places

Acknowledgements

where I learned most, where I had the privilege to play with science. For this reason, I want to express my gratitude to Bob Cubitt, Jon White, Michel Bonnaud, Victorien Joyet and Markus Zolliker who have always been willing to try any idea we had in mind, no matter how difficult or time-consuming it was. Also, thank you to our collaborators Alex Holmes, Alistair Cameron, Hazuki Furukawa, Minoru Soda, Oleksandr Prokhnenko, Maciej Bartkowiak, Markus Bleuel, Yamali Hernandez, Hermann Suderow, Isabel Guíllamón, Nina-Juliane Steinke and Oliver Stockert, for being always collaborative, reply all my emails and providing the necessary samples for this thesis. Also I would like to thank to the collaborators who have been helping us closely during the preparation of our experiments or in other projects that are not included in this thesis as Ketty Beauvois, Bachir Ouladdiaf, Lucile Mangin-Thro, Andrew Wildes, Martin Boehm, Paul Steffens and Ingo Hoffmann. Thank you all for offering me the opportunity to start my research career with your help.

Living in new places has always been one of my passions, but travelling means that many friendships will be lost in time and distance. However, I always keep in mind that it is better to miss people than never to have met them. I want to thank all the people who have helped me since I started his journey, long before these last four and a half years.

Vivir en lugares nuevos siempre ha sido una de mis pasiones, pero, viajar significa que habrán amistades que se perderán en el tiempo y en la distancia. Sin embargo, siempre tengo presente que es mejor extrañar a las personas que nunca haberlas conocido. Sólo por eso, me gustaría dar las gracias a todas las personas que me han ayudado desde que comencé este viaje, mucho antes de estos últimos cuatro años y medio.

Para empezar, a los profesores de mi colegio durante la secundaria, José María y Javier, por haberos sentido orgullosos de mí. Conseguíais que no me sintiera tan mal conmigo misma y eso me ayudaba a seguir trabajando. Quiero hacer una mención especial a los profesores que empezaron a sembrar en mí, durante los años decisivos de Bachillerato. A Joya, por protegerme y ayudarme en uno de los momentos más difíciles de mi vida. A Cari, por ser una de las profesoras que más me motivó a esforzarme e ir más allá de mis límites. Te prometí que algún día te nombraría cuando me diesen un gran premio. Éste puede que sea uno de los mayores logros de mi vida y quiero agradecértelo. A Juan, por ser otro de los profesores que conseguía que diera todo de mí y uno de los culpables de esta tesis.

Tú fuiste, junto a Víctor, uno de los profesores que encendió la mecha para que eligiera estudiar física. Víctor, como ya he dicho, tú empezaste a hablarme de la universidad con pasión y estabas completamente seguro que disfrutaría estudiando una carrera de ciencias. A todos, os doy las gracias de corazón.

Durante mis años como estudiante de física tuve muchas dudas, ¿seré suficiente? ¿Valgo para esto? ¿Soy inteligente? ¿Podré ser investigadora? ¿Qué rama de física estudiaré?

Y algunas de las personas que empezaron a iluminar ese camino de dudas, fueron los entonces estudiantes de doctorado Víctor, Miriam, Irene y en especial, Miguel, que me descubrieron que no es necesario ser un genio para ser un buen investigador y mi verdadera pasión: la cuántica. Miguel, gracias por tutorizarme y quería dedicar parte de los agradecimientos a la energía y confianza que depositaste en mí en esos momentos de completa indecisión. Tus palabras fueron clave para que yo pudiera avanzar.

Tras mi paso por Madrid, tengo que mencionar a mis amigos de la residencia RESA. Cuando me sentía sola o aburrida de estudiar, la hora de la comida y la cena se convertían en un soplo de aire fresco. Gracias por todos los momentos juntos, por las horas de estudio compartidas y por ser la pequeña familia en la que me podía refugiar. Quiero hacer una mención especial a Teseo, al que deseo de corazón un brillante futuro.

A Eider, quien me ha enseñado mucho más de lo que cree y de quien me siento muy orgullosa de lo lejos que ha llegado, gracias por estar siempre al otro lado del teléfono para mandarme un abrazo virtual y por preocuparte siempre por mí.

A Andrea, la autora de la espectacular portada de esta tesis y una de las personas más maravillosas que tengo a mi lado, te agradezco que te sientas tan feliz de mis logros como yo de los tuyos. Ambas sentimos que estamos avanzando de la mano en este mundo de la investigación. Es un verdadero placer tenerte como amiga y jamás dudes de lo extraordinaria que eres.

Tras finalmente decidirme por la materia condensada, mi decisión me llevó a Bilbao y a conoer a uno de los mejores supervisores que he tenido el placer de tener: Michele. Tú me enseñaste en qué consistía la investigación y los hábitos de trabajo para avanzar en un proyecto. Por ello, te doy las gracias por abrirme paso en este mundo.

A la pequeña familia que me llevó de Bilbao, Maialen, Naiara, Leire, Nagore y Garatzi, que me hicieron sentir bienvenida y acogida; y a Janire, con la que he seguido en contacto

Acknowledgements

durante estos años y siempre me ha animado a volar. A todas, eskerrik asko.

También quiero agradecer las horas compartidas con el servicio de RESA y de Atalaia, sobre todo con Charo, Julián, Anita, Eva y Zigor, que me animaban a estudiar y perseverar, aún cuando me sentía triste por estar lejos de mi familia.

Big thanks to all the friends I had to say goodbye sadly, but they were always supportive and caring when I needed them, Megan and Alex Pattison. To all the new friends I found in Sweden: Lisa, you were my first friend here and the one who always makes me smile, and I hope to have more time to visit you; Rosa, thanks for all your support and for kidnapping me every time I needed a break. Big thanks also to Camilla, who welcomed me when I first arrived at Lund and offered me the place I considered my home during these last years.

Gracias a mis amigas, Teresa y Elena Sánchez. Fuisteis las primeras verdaderas amigas que tuve y que por fortuna aún conservo.

Gracias a Dana y Victoria, amigas luchadoras que no conocen la palabra *rendición* y que consiguen que no me sienta tan lejos de ellas cada vez que hablamos por Skype. Pronto será vuestro turno de defender vuestras tesis y espero que os sintáis tan plenas y felices como me siento yo ahora mismo escribiendo estas palabras.

Gracias a Julia y a Elena Seoane, por estar siempre junto a mí cada día. Sorprendentemente, nuestra amistad se ha hecho mucho más fuerte a lo largo de los años y ahora no soy capaz de hablar con vosotras sin mandaros un pódcast de al menos cinco minutos. Jamás me habéis dejado sola, y, sobre todo durante la pandemia, me habéis hecho sentir fuerte. Me siento profundamente afortunada de teneros como amigas. Sé que es una mala costumbre que tengo, pero os agradezco todo el tiempo que habéis compartido conmigo. Si tuviera que comparar nuestra amistad con un alimento, sin duda sería con el caviar.

Creo que no hubiera empezado este camino de la misma forma sin la persona que lo ocasionó todo: Jorge. Empezamos este camino juntos, siendo muy jóvenes, y ahora estamos empezando a vivir la vida con la que tanto habíamos soñado. Nada de esto habría sido posible sin tu ayuda (sin ir más lejos, fuiste tú quien me presentó a Elizabeth) y sin ese gran corazón de oro que tienes. Me siento muy afortunada de tenerte en mi vida y muy orgullosa de todo lo que has conseguido hasta ahora. Espero verte llegar muy lejos.

Llegando ya al final, quiero darle las gracias una de las personas a las que va dedicada

esta tesis, a Adolfo Bastida Pascual. Desde el primer día que entré en tu despacho al borde de las lágrimas, tú sabías de lo que era capaz. Tú has sido testigo de todas y cada una de las veces que he sentido dudas y no me sentía capaz de continuar. Te doy las gracias por creer en mí, incluso cuando ni yo misma lo hacía. Te doy las gracias por las horas dedicadas a enseñarme a luchar. Te doy las gracias por seguir siendo mi tutor y mi aliado en la batalla. Te doy las gracias, en definitiva, por demostrarme que yo sí estaba a la altura de este sueño. Ojalá algún día, alguien me dedique estas mismas palabras en su tesis doctoral, porque eso significará que estaré dedicándome al mejor trabajo del mundo. Gracias, siempre.

Por último pero no menos importante. gracias a toda mi familia, en especial a mis tías y a mis abuelas. Sé lo difícil que ha sido tenerme lejos pero a pesar de todo, siempre me habéis apoyado en mi decisión y sé que os sentís orgullosos de mí.

A mi hermana Irene, no sólo quiero agradecerle el tiempo juntas sino mostrarle que esta tesis es un ejemplo de que los sueños se cumplen, pero no sin esfuerzo.

Y, finalmente, a mis padres. Manolo, Loli, gracias por todo vuestro sacrificio. No sólo material, sino por el dolor que supone tenerme a kilómetros de distancia y no poder abrazarme cuando he tenido un mal día, no poder consolarme cuando he tenido un problema o en definitiva, por no tenerme cerca. Sin embargo, jamás me habéis sentido tan feliz como lo estoy ahora. Estos últimos días no paro de recordar, todas aquéllas ocasiones en las que salía del colegio llorando y me repetíais que en la universidad descubriría otra vida. No estabáis errados. La etapa más feliz de mi vida ha sido, y sigue siendo, la universidad, y espero que así sea por muchos años. Por ello, os doy las gracias, porque a pesar de la incertidumbre, me habéis apoyado en mi sueño. Os quiero mucho.

Thank you all.

Gracias a todos.



Emma

Contents

ABSTRACT	I
POPULAR SCIENCE SUMMARY	III
POPULÄRVETENSKAPLIGA SAMMANFATTNINGAR	VII
RESUMEN DE DIVULGACIÓN CIENTÍFICA	XI
LIST OF PUBLICATIONS	I
LIST OF ABBREVIATIONS	V
1. BASIC THEORETICAL CONCEPTS OF SUPERCONDUCTIVITY	1
1.1. Phenomenology and London Theory	1
1.2. Ginzburg-Landau Theory	3
1.3. The Abrikosov flux lattice	4
1.4. Microscopic BCS Theory	6
1.5. Unconventional Superconductivity	8
2. SMALL-ANGLE NEUTRON SCATTERING	11
2.1. Elemental neutron scattering	11
2.1.1. Differential scattering cross section	12
2.2. Magnetic scattering	13
2.2.1. Magnetic scattering of the flux-line lattice	13
2.2.1.1. Flux-line lattice form factor	15
2.3. Small-Angle Neutron Scattering	17
2.3.1. SANS Instrumentation	17

2.3.1.1.	TOF instrumentation	18
2.3.2.	FLL form factor analysis	18
2.3.2.1.	FLL form factor analysis for TOF instruments	20
2.4.	Bayesian reduction of the flux-line lattice	21
2.4.1.	Application of Bayes' theorem to FLL processing	22
2.4.2.	Visualization of the vortex lattice	24
2.4.3.	Calculation of the form factor by Bayesian method	27
3.	STUDY OF PAULI-PARAMAGNETIC EFFECTS IN HEAVY-FERMION SUPERCONDUCTORS	29
3.1.	Pauli-limited Superconductivity	29
3.2.	Heavy-fermion superconductors	30
3.3.	Cerium-based heavy-fermion superconductors: CeCu_2Si_2	32
3.4.	Pauli paramagnetism and the vortex lattice in superconducting CeCu_2Si_2	38
3.5.	Modelling of VL behaviour in Pauli-limited superconductors	41
3.6.	Summary	53
4.	HIGH-MAGNETIC FIELD STUDIES ON THE HIGH-TEMPERATURE SUPERCONDUCTOR YBCO	55
4.1.	Previous SANS studies on YBCO	56
4.2.	High field SANS studies on $\text{YBa}_2\text{Cu}_3\text{O}_7$ and $\text{Ca}_x\text{Y}_{1-x}\text{Ba}_2\text{Cu}_3\text{O}_7$	61
4.3.	Summary	67
5.	SMALL-ANGLE NEUTRON SCATTERING STUDIES ON TOPOLOGI- CAL SUPERCONDUCTOR CANDIDATES	69
5.1.	Topological superconductor candidates	72
5.1.1.	PbTaSe_2	72
5.1.1.1.	SANS experiment on PbTaSe_2	73
5.1.2.	Au_2Pb	75
5.1.2.1.	SANS experiment on Au_2Pb	76
5.1.3.	$\beta\text{-Bi}_2\text{Pd}$	77
5.2.	VL Bending and characteristic lengths in $\beta\text{-Bi}_2\text{Pd}$	81

CONTENTS

5.3. Summary	85
CONCLUSIONS	87
BIBLIOGRAPHY	89

CONTENTS

Abstract

Using Small-Angle Neutron Scattering (SANS) we have studied the flux line lattices of the first heavy-fermion superconductor to be discovered, CeCu_2Si_2 , the well-known high-temperature superconductor $\text{YBa}_2\text{Cu}_3\text{O}_7$, along with Ca-doped variants of this compound, and several topological superconductor candidates that have attracted a lot of attention in the last few years, such as PbTaSe_2 , Au_2Pb and $\beta\text{-Bi}_2\text{Pd}$.

Unconventional superconductors, with pairing mechanisms and properties that are not accounted for within BCS theory, are a subject of continuing interest. One example is heavy-fermion materials, in which the charge carriers respond as if they had a mass many times that of a free electron. We find that CeCu_2Si_2 shows a strong increase of scattered intensity from the flux lines as the applied magnetic field is increased towards the edge of the superconducting phase. In the standard theories, this intensity should drop steadily towards zero. This indicates that the superconductivity in this material is not destroyed by the same mechanism as in most all other superconductors but is instead destroyed by Pauli paramagnetic effects (PPE), which act to break up the Cooper pairs by favouring parallel alignment of the spins, increasing the relative strength of the magnetization in the vortex cores. This behaviour had previously been observed in CeCoIn_5 . To better understand the behaviour of CeCu_2Si_2 and other Pauli limited superconductors, we present a physically-based expression for the size and magnetization of the vortex cores in Pauli-limited superconductors.

For many years, high-temperature superconductors have attracted significant attention as they may be key for the use of superconductors in our everyday life. In the high- T_c superconductors, like $\text{YBa}_2\text{Cu}_3\text{O}_{7-\delta}$ (YBCO), the doping level can be used to tune the observed properties. Usually, δ is the doping control parameter in YBCO, which varies the occupancy of the oxygen chains running along the \mathbf{b} -axis of the crystal. The (d -

wave) superconductivity in YBCO develops primarily from the CuO_2 planes, but s -wave superconductivity also develops from the chains, which can be seen in the distortion of the vortex lattice. We study the temperature and field dependence of this anisotropy and SANS intensity from the vortex lattice up to 25 T using a newly developed formula for SANS time-of-flight (TOF) experiments. Furthermore, we can dope the yttrium site with calcium instead, resulting in a higher hole concentration than fully over-doped YBCO, pushing the field scale down closer to the magnetic fields we can apply in experiment. We include in this work some of the specific effects of doping YBCO with calcium and how it lowers the characteristic critical fields.

Topological materials have attracted a lot of attention due to their novel quantum states and their possible applications to quantum computation. A key property is the appearance of Majorana bound states in the vortex core. When the Bogoliubov quasiparticles associated with the superconducting state can be constructed as superpositions of electron and hole states such that the bound quasiparticle is its own anti-quasiparticle (i.e. a Majorana particle), in the bulk, these quasiparticles are dispersive Majorana fermions, and in the vortex core they lead to bound states that obey non-Abelian statistics, and can (in theory) be used as qubits. In this thesis we report SANS experiments performed on three different topological superconductor candidates, PbTaSe_2 , Au_2Pb and $\beta\text{-Bi}_2\text{Pd}$. For the latter, we discuss the anisotropy of the vortex lattice and the temperature dependence of the SANS intensity by rotating the sample with respect to the magnetic field direction and shed some light on the superconducting gap nature of $\beta\text{-Bi}_2\text{Pd}$.

Popular science summary

Most common electrical wiring is made from conducting materials, like copper, and offers resistance to current. This resistance leads to a significant loss of the total energy produced in the world. However, quantum physics can give us a hand to get around this problem.

There are several materials, like lead and aluminium, that radically change their electrical and magnetic characteristics when their temperature drops close to absolute zero (-273.15°C). They lose all resistance to the current flow. These materials are known as superconductors. The materials remain in their superconducting state unless we apply high magnetic fields above a certain upper critical field or we increase the temperature above a particular critical temperature where superconductivity is destroyed. Another particular effect of such materials is that they are able to expel the magnetic field applied to them (Meissner effect) or just allow magnetic flux to enter as small tubes or flux lines. In the latter case, the material is not superconducting inside the flux lines while the rest of the material stays superconducting up to larger fields, or with larger applied currents than materials that expel all the magnetic flux.

Superconductivity is one of the most exotic physical phenomena yet observed, and has attracted a lot of attention due to its many applications. For example medicine in magnetic resonance imaging (MRI), the development of maglevs (magnetic levitation trains), for building guides for focussing the particles' trajectory in CERN, and they are even being used for building devices that could contain the huge amount of energy generated by nuclear fusion.

To study superconductors, we looked at the small tubes of magnetic flux that develop inside these superconductors when they are put in a magnetic field. These tubes form a regular arrangement, the flux line lattice. We then use neutron scattering to diffract off

the flux-line lattice, because the size and arrangement of those resulting flux lines tell us about the underlying superconductivity. In short, we need to lower the temperature to achieve superconductivity, and we need to apply a magnetic field to "see it with neutrons."

Even though superconductivity was first discovered over 100 years ago, there are still many open questions. While conventional superconductors are well explained by the Bardeen–Cooper–Schrieffer (BCS) theory, a large number of unconventional superconductors, named 'heavy-fermion', 'high-temperature' and 'topological' superconductors behave differently, and in this thesis this is exploited. One of the materials that we studied is CeCu_2Si_2 , the first heavy fermion superconductor to be discovered in 1979. A first question could be what does heavy fermion mean?

In a superconductor, the charge carriers (usually electrons) pair up to form a Cooper pair. In a heavy fermion material, the charge carriers behave as though they have a mass many times that of a free electron, pushing all the energy scales in the materials lower. BCS theory cannot be applied to materials like this, and so a lot of questions remain over the superconducting state. We studied CeCu_2Si_2 because it shows a very unusual increase in intensity of neutrons scattered by the flux lines towards the edge of the superconducting phase, whereas in most other superconductors, this intensity drops towards zero, indicating that the superconductivity is not destroyed in the same way as in conventional superconductors.

In the case of high-temperature superconductors, the materials remain in their superconducting state up to temperatures around 80 K (-193,15°C) and it is predicted that magnetic fields up to 100 T are still not sufficient to destroy superconductivity. This is the case for $\text{YBa}_2\text{Cu}_3\text{O}_7$ (YBCO), where the study of its flux-line lattice has been constrained by instrumental limits, since achievable magnetic fields used in neutron scattering do not exceed 17 T and only instruments with single-energy (monochromatic) neutron beams were used. In our studies, we have not only been able to measure the diffracted intensity from the flux-line lattice of this material up to 25 T but we have also developed a new way of measuring the diffracted flux-line intensity using instruments that work with multiple-energy (multichromatic) neutrons.

Last but not least, a new kind of superconductivity has emerged from the study of materials, which are topological superconductors. The peculiarity of these superconduct-

tors is that they can contain states called Majorana fermions, a particle that is its own antiparticle (an identical particle but with opposite charge). The novelty of this is that Majorana fermions have not been observed in nature yet, and the discovery of a natural topological superconductor could mean not only a revolution inside condensed matter physics but also for particle physics and quantum computing. For this reason, many groups, including ours, have been studying the superconducting properties of materials that are possible candidates to be natural topological superconductors, like PbTaSe_2 , Au_2Pb and $\beta\text{-Bi}_2\text{Pd}$.

Neutron scattering has opened a window to the study of one of the most mysterious phenomena in condensed matter physics and allows us to investigate some magnetic characteristics that are not possible to study with other scattering techniques. This thesis is just one example of the many possibilities that this type of technique can offer to unravel knotty problems in superconductivity and take a step forward in science.

Populärvetenskapliga sammanfattningar

De flesta vanliga elektriska ledningar är gjorda av ledande material, såsom koppar, och ger motstånd mot ström. Denna resistans leder till en signifikant förlust av den totala energin som produceras i världen. Dock kan kvantfysik hjälpa oss att komma runt problemet.

Det finns flera material, såsom bly och aluminium, som radikalt ändrar sin elektriska och magnetiska karaktäristik när deras temperatur sjunker nära absoluta nollpunkten ($-273,15^{\circ}\text{C}$). De förlorar all resistans mot strömflödet. Dessa material kallas supraledare. Materialen stannar i sitt supraledande tillstånd såvida vi inte lägger på höga magnetiska fält över ett visst övre kritiskt fält eller om vi ökar temperaturen över en särskild kritisk temperatur där supraledningen förstörs. En annan särskild effekt hos sådana material är att de kan driva ut det magnetiska fältet som läggs över dem (Meissnereffekten) eller bara tillåta magnetiskt flöde att komma in i små rör eller flödeslinjer. I det senare fallet är materialet inte supraledande inuti flödeslinjerna medan resten av materialet förblir supraledande upp till större fält, eller med större pålagda strömmar än material som driver ut allt magnetiskt flöde.

Supraledning är en av de mest exotiska fysikaliska fenomen som observerats och har fått mycket uppmärksamhet tack vare sina många applikationer. Till exempel medicin i magnetisk resonansavbildning (MRI), utvecklingen av maglevtåg (magnetiskt svävande tåg), byggandet av ledningar som fokuserar partiklarnas bana i CERN, och dessutom används de för att bygga apparater som kan innehålla den stora mängden energi som genereras genom kärnfusion.

För att studera supraledare har vi tittat på de små rören av magnetiskt flöde som

utvecklas inuti dessa supraledare när de placeras i ett magnetiskt fält. Dessa rör bildar ett regelbundet arrangemang, flödeslinjegittret. Vi använder sedan neutronspridning för att sprida från flödeslinjegittret, eftersom storleken och arrangemanget av de resulterande flödeslinjerna avslöjar den underliggande supraledningen. Kort och gott behöver vi sänka temperaturen för att uppnå supraledning, och vi behöver lägga på ett magnetiskt fält för att ”se” det med neutroner.

Trots att supraledning upptäcktes för första gången över 100 år sedan så finns det fortfarande många öppna frågor. Medan konventionella supraledare förklaras väl av Bardeen-Cooper-Schrieffer-teorin (BCS-teorin) så finns det ett stort antal okonventionella supraledare, så kallade ’tungfermion-’, ’högtemperatur-’ och ’topologiska’ supraledare, som uppför sig annorlunda, och i denna avhandling utnyttjas detta.

En av materialen som vi studerade är CeCu_2Si_2 , den första tungfermionsupraledaren som upptäcktes 1979. En första fråga kanske kan vara vad tung fermion betyder?

I en supraledare parar laddningsbärarna (vanligtvis elektroner) ihop sig och bildar ett Cooperpar. I ett tungfermionsupraledarmaterial uppför sig laddningsbärarna som om de hade en massa flera gånger större än den hos en fri elektron och trycker ner energiskalorna i materialet. BCS-teorin kan inte appliceras på sådana material, och därför återstår många frågor rörande det supraledande tillståndet. Vi studerade CeCu_2Si_2 eftersom det visar en mycket ovanlig ökning i intensitet från neutroner som sprids av flödeslinjerna mot kanten på supraledningsfasen, medan denna intensitet sjunker mot noll i de flesta andra supraledare, vilket indikerar att supraledningen inte förstörs på samma sätt som i konventionella supraledare.

I fallet med högtemperatursupraledare förblir materialet i sitt supraledande tillstånd upp till temperaturer omkring 80 K ($-193,15^\circ\text{C}$) och det förutses att magnetiska fält upp till 100 T fortfarande inte är tillräckligt för att förstöra supraledningen. Detta är fallet för $\text{YBa}_2\text{Cu}_3\text{O}_7$ (YBCO), där studien av dess flödeslinjegitter har begränsats genom instrumentella begränsningar, då uppnåbara magnetiska fält som används i neutronspridning inte överstiger 17 T och endast instrument med neutronstrålar med en energi (monokromatiska strålar) användes. I våra studier har vi inte bara kunnat mäta den spridda intensiteten från detta materials flödeslinjegitter upp till 25 T, utan vi har även utvecklat ett nytt sätt att mäta den spridda flödeslinjeintensiteten genom att använda instrument

med neutroner med flera energier (multikromatiska strålar).

Sist men inte minst har en ny typ av supraledning framkommit ur materialstudien, där materialen är topologiska supraledare. Egenheten hos dessa supraledare är att de kan innehålla tillstånd som kallas Majoranafermioner, en partikel som är sin egen antipartikel (en identisk partikel men med motsatt laddning). Nyheten med detta är att Majoranafermioner inte har observerats i naturen ännu, och upptäckten av naturliga topologiska supraledare kan innebära inte bara en revolution inom den kondenserade materiens fysik, utan även för partikelfysik och kvantdatorvetenskap. Av denna anledning har många grupper, inklusive vår, studerat de supraledande egenskaperna hos material som är positiva kandidater till att bli naturliga topologiska supraledare, såsom PbTaSe_2 , Au_2Pb och $\beta\text{-Bi}_2\text{Pd}$.

Neutronspridning har öppnat ett fönster mot studien av en av de mest mystiska fenomenen inom den kondenserade materiens fysik och låter oss undersöka några magnetiska karaktäristika som man inte kunnat studera med andra spridningstekniker. Denna avhandling är bara ett exempel på de många möjligheter som denna typ av teknik kan erbjuda för att reda ut knepiga problem inom supraledning och ta ett steg framåt i vetenskapen.

Resumen de divulgación científica

El cableado eléctrico más común está hecho de materiales conductores, como el cobre, y ofrece resistencia a la corriente. Esta resistencia provoca una pérdida importante de la energía total producida en el mundo. Sin embargo, la física cuántica puede echarnos una mano para sortear este problema.

Hay varios materiales, como el plomo y el aluminio, que cambian radicalmente sus características eléctricas y magnéticas cuando disminuyen su temperatura cerca del cero absoluto ($-273,15^{\circ}\text{C}$). Pierden toda resistencia al flujo de corriente. Estos materiales se conocen como superconductores. Los materiales permanecen en su estado superconductor a menos que apliquemos campos magnéticos elevados por encima de un determinado campo crítico superior o que aumentemos la temperatura por encima de una determinada temperatura crítica en la que se destruye la superconductividad. Otro efecto particular de estos materiales es que son capaces de expulsar el campo magnético que se les aplica (efecto Meissner) o simplemente permiten la entrada del flujo magnético en forma de pequeños tubos o líneas de flujo. En este último caso, el material no es superconductor dentro de las líneas de flujo, mientras que en el resto del material sigue siendo superconductor hasta campos mayores, o soportan corrientes mayores que los materiales que expulsan todo el flujo magnético.

La superconductividad es uno de los fenómenos físicos más exóticos que se han observado hasta ahora, y ha atraído mucha atención debido a sus múltiples aplicaciones. Por ejemplo, en la medicina, en las imágenes por resonancia magnética (IRM), en el desarrollo de maglevs (trenes de levitación magnética), en la construcción de guías para redirigir la trayectoria de las partículas en el CERN, e incluso se están utilizando para construir dispositivos que podrían contener la enorme cantidad de energía generada por la fusión nuclear.

Para estudiar los superconductores, nos fijamos en los pequeños tubos de flujo magnético que se desarrollan en el interior de estos superconductores cuando se les aplica un campo magnético. Estos tubos forman una disposición regular, la red de líneas de flujo. A continuación, utilizamos la dispersión de neutrones para difractar la red de líneas de flujo, porque el tamaño y la disposición de esas líneas de flujo resultantes nos informan sobre la superconductividad subyacente. En resumen, hay que bajar la temperatura para conseguir la superconductividad, y hay que aplicar un campo magnético para "verlaçon neutrones".

Aunque la superconductividad se descubrió por primera vez hace más de 100 años, todavía hay muchas cuestiones abiertas. Mientras que los superconductores convencionales se explican bien mediante la teoría de Bardeen-Cooper-Schrieffer (BCS), un gran número de superconductores no convencionales, denominados superconductores de "fermiones pesados", de "alta temperatura" y "topológicos" se comportan de forma diferente, y en esta tesis exploramos este tema.

Uno de los materiales que estudiamos es el CeCu_2Si_2 , el primer superconductor de fermiones pesados descubierto en 1979. Una de nuestras primeras preguntas sería ¿qué son los fermiones pesados?

En un superconductor, los portadores de carga (normalmente electrones) se emparejan para formar un par de Cooper. En un material fermiónico pesado, los portadores de carga se comportan como si tuvieran una masa muchas veces superior a la de un electrón libre, lo que hace que todas las escalas de energía de los materiales sean más bajas. La teoría BCS no puede aplicarse a este tipo de materiales, por lo que quedan muchos interrogantes sobre su estado superconductor. Decidimos estudiar el CeCu_2Si_2 porque muestra un aumento muy inusual de la intensidad de los neutrones dispersados por las líneas de flujo muy cerca del límite de la fase superconductora, mientras que, en la mayoría de los demás superconductores, esta intensidad cae hacia cero, lo que indica que la superconductividad no se destruye de la misma manera que en los superconductores convencionales.

En el caso de los superconductores de alta temperatura, los materiales permanecen en su estado superconductor hasta temperaturas alrededor de los 80 K (-193,15°C) y se ha predicho que los campos magnéticos de hasta 100 T siguen sin ser suficientes para destruir la superconductividad. Este es el caso del $\text{YBa}_2\text{Cu}_3\text{O}_7$ (YBCO), el estudio de su red de líneas de flujo se ha visto restringido por los límites instrumentales, ya que los campos

magnéticos alcanzables utilizados en la dispersión de neutrones no superan los 17 T y sólo se utilizaron instrumentos con haces de neutrones de una sola energía (monocromáticos). En nuestros estudios, no sólo hemos podido medir la intensidad difractada de la red de líneas de flujo de este material hasta 25 T, sino que también hemos desarrollado una nueva forma de medir la intensidad difractada de las líneas de flujo utilizando instrumentos que trabajan con neutrones de energía múltiple (multicromáticos).

Por último, pero no menos importante, ha surgido un nuevo tipo de superconductividad a partir del estudio de los materiales, que son los superconductores topológicos. La peculiaridad de estos superconductores es que pueden contener estados llamados fermiones de Majorana, una partícula que es su propia antipartícula (una partícula idéntica pero de carga opuesta). La novedad es que los fermiones de Majorana no se han observado aún en la naturaleza, y el descubrimiento de un superconductor topológico natural podría suponer no sólo una revolución dentro de la física de la materia condensada, sino también para la física de partículas y la computación cuántica. Por esta razón, muchos grupos, incluido el nuestro, han estado estudiando las propiedades superconductoras de materiales que son posibles candidatos a ser superconductores topológicos naturales, como PbTaSe_2 , Au_2Pb y $\beta\text{-Bi}_2\text{Pd}$.

La dispersión de neutrones ha abierto una ventana al estudio de uno de los fenómenos más misteriosos de la física de la materia condensada y nos permite investigar algunas características magnéticas que no son posibles de estudiar con otras técnicas de dispersión. Esta tesis es sólo un ejemplo de las muchas posibilidades que este tipo de técnica puede ofrecer para desentrañar problemas espinosos en la superconductividad y dar un paso adelante en la ciencia.

List of publications

I have prepared this thesis myself, based in part on work that has appeared in the following publications, in which I have contributed to the experiments, the analysis of the experimental data and writing of the papers:

I Analysis of time-of-flight SANS data on mesoscopic crystals such as flux line lattices

E. Campillo, E. Blackburn, E. M. Forgan, M. Bartkowiak, O. Prokhnenko, P. Smeibidl

Submitted to Journal of Applied Crystallography (2022)

I developed and optimized the code and the method explained in the paper. I carried out the data analysis using this code and and I was the main responsible for the manuscript writing.

II Unconventional superconductivity in the nickel chalcogenide superconductor TiNi_2Se_2

E. Jellyman, P. Jefferies, S. Pollard, E. M. Forgan, E. Blackburn, E. Campillo, A. T. Holmes, R. Cubitt, J. Gavilano, Hangdong Wang, Jianhua Du and Minghu Fang

Phys. Rev. B 101, 134523 (2020)

I did the Bayesian analysis of the neutron diffraction data and reviewed and commented on the manuscript.

III Observations of the effect of strong Pauli paramagnetism on the vortex lattice in superconducting CeCu_2Si_2

E. Campillo, R. Riyat, S. Pollard, P. Jefferies, A. T. Holmes, R. Cubitt, J. S. White, J. Gavilano, Z. Huesges, O. Stockert, E. M. Forgan, and E. Blackburn

Phys. Rev. B 104, 184508 (2021)

I took part in most of the SANS experiments covered in the paper, did all the data analysis, took part in the development of the theoretical model and its testing and was the main responsible for the manuscript writing. After publication, I spotted an error in one part of the data reduction. This error does not alter the conclusions of the paper. The draft erratum proposed to Phys. Rev. B is attached to the paper. The results presented in the thesis are all corrected.

IV A phenomenological model of vortex lattice behavior in Pauli-limited superconductors

E. Campillo, E. M. Forgan and E. Blackburn

In manuscript

I took part in the development of the theoretical model and its testing on several materials and I was the main responsible for the manuscript writing.

V Deviations from the extended London model at high magnetic fields in $\text{YBa}_2\text{Cu}_3\text{O}_7$

E. Campillo, M. Bartkowiak, R. Riyat, E. Jellyman, A. S. Cameron, A. T. Holmes, O. Prokhnenko, W.-D. Stein, A. Erb, E. M. Forgan and E. Blackburn

arXiv:2203.01705

Submitted to Physical Review B (2022)

I developed and optimized the codes used to analyze the data, carried out the data analysis and was the main responsible for the manuscript writing.

VI High magnetic field studies of the Vortex Lattice structure in Ca-doped YBCO

A. S. Cameron & E. Campillo, A. Alshemi, L. Shen, H. Kawano-Furukawa, A. T. Holmes, R. Cubitt, N. J. Steinke, C. D. Dewhurst, A. Erb, E. M. Forgan and E. Blackburn

In manuscript

I carried out all of the experimental work on the 15% doped sample, including experiment design, analysed the TOF data and supervised the analysis of the monochromatic data. Together with Alistair Cameron, who led the work on the 4% doped sample, I was responsible for the writing and preparation of the manuscript.

VII Field Dependence of Superfluid Density in β -PdBi₂

M. Soda, N. Kagamida, S. Mühlbauer, E. M. Forgan, E. Campillo, M. Kriener, H. Yoshizawa and H. Kawano-Furukawa

J. Phys. Soc. Jpn. 90, 104710 (2021)

I did the Bayesian analysis of the neutron diffraction data and I contributed to the manuscript discussion.

VIII Penetration Depth and Coherence Length in the Superconductor β -PdBi₂

M. Soda, N. Kagamida, E. Campillo, E. M. Forgan, E. Blackburn, S. Mühlbauer, R. Cubitt, H. Suderow, I. Guillamón, E. Herrera, H. Yoshizawa, and H. Kawano-Furukawa

J. Phys. Soc. Jpn. 91, 034706 (2022)

I independently proposed and designed the experiment carried out at ILL. I carried out the full analysis of this part of the data. We agreed to publish in conjunction with our collaborators from Ochanomizu University. I did part of the SANS data analysis and I contributed to the manuscript writing and discussion.

Publications to which I contributed that are not included in this thesis:

IX Magnetic microphase inhomogeneity as a thermodynamic precursor of ground-state phase separation in weakly coupled spin- $\frac{3}{2}$ chains

L. Shen, E. Campillo, E. Young, C. Bulbucan, R. Westerström, M. Laver, P. J. Baker and E. Blackburn

Phys. Rev. B 103, 134420 (2021)

X Inhomogeneous spin excitations in weakly coupled spin- $\frac{1}{2}$ chains

L. Shen, E. Campillo, O. Zaharko, P. Steffens, M. Boehm, K. Beauvois, B. Ouladdiaf, Z. He, D. Prabhakaran, A. T. Boothroyd and E. Blackburn

Phys. Rev. Research 4, 013111 (2022)

List of Abbreviations

BCS	Bardeen–Cooper–Schrieffer
DOS	Density of States
FF	Form Factor
FLL	Flux-line lattice
GL	Ginzburg-Landau
HFM/EXED	High Field Magnet and the Extreme Environment Diffractometer
HFS	High Field Structure
HZB	Helmholtz-Zentrum Berlin
IFS	Intermediate Field Structure
ILL	Institute Laue-Langevin
LFS	Low Field Structure
NIST	National Institute of Standards and Technology
PPE	Pauli Paramagnetic Effect
PSI	Paul Scherrer Institute
QCP	Quantum Critical Point
QPT	Quantum Phase Transition
SANS	Small-Angle Neutron Scattering
SC	Superconductivity/Superconductor
SDW	Spin Density Wave
TOF	Time of Flight

VL	Vortex Lattice
WHH	Werthamer-Helfand-Hohenberg
YBCO	$\text{YBa}_2\text{Cu}_3\text{O}_{7-\delta}$

CHAPTER 1

Basic Theoretical Concepts of Superconductivity

Superconductivity was first observed by Kamerlingh Onnes [1] in 1911. He observed that for some materials the electrical resistance went to zero at a certain critical temperature T_c , which depends on the metal. Then, Meissner and Ochsenfeld discovered the perfect diamagnetism of the superconducting state [2]. They observed that a magnetic field in a superconducting sample is expelled when it is cooled down T_c . This effect is only possible when the current carriers have a charge of $e^* = 2e$. This behaviour is confirmed because of the observation of persistent currents. When the Meissner-Ochsenfeld effect is present we observe that the magnetic field is totally expelled from the sample and consequently the relationship between magnetization produced in the sample \mathbf{M} and the magnetic field induced by external currents, \mathbf{H} , becomes $\mathbf{M} = -\mu_0\mathbf{H}$ and the magnetic susceptibility is $\chi = -1$.

1.1. PHENOMENOLOGY AND LONDON THEORY

Assuming a phenomenological thermodynamic theory and taking into account the Meissner effect where $\mathbf{B} = 0$, $\mathbf{M} = -\mathbf{H}$, we know that the transition from the normal

state to the superconducting state is produced when the Gibbs free energies in the normal and superconducting state coincide at a specific temperature T :

$$G_S(H_c(T)) = G_N(H_c(T)) \Rightarrow G_N(H_c) - G_S(H) = \mu_0 \frac{H_c^2 - H^2}{2}. \quad (1.1)$$

From this equation we can deduce that the entropy difference between the superconducting state and the normal state is

$$S_S(H_c, T) - S_N(H, T) \leq 0, \quad (1.2)$$

and in addition, this gap in the entropy can be translated as a first order transition and we see that this transition is more stable when the superconducting state is more ordered than the normal one. At a critical temperature our critical magnetic field is $H_c = 0$, the entropy difference is zero and the phase transition is not first order.

The first theory for describing the electrodynamics of superconductors was developed by F. London and H. London in 1935. They assumed that a fraction of the conduction electrons became superfluid, and could move with no resistance. Assuming that n_S is the density of superconducting electrons, this idea led to the development of the London equations, which relate the electrical current density inside a superconductor, \mathbf{j}_S , to the magnetic potential, \mathbf{A} , by

$$\mathbf{j}_S = -\frac{n_S e^{*2}}{m^*} \mathbf{A} = n_S e^* \langle \mathbf{v}_S \rangle \quad (1.3)$$

where m^* is the mass of the superconducting quasiparticles. Assuming a zero net momentum in the ground state, $m^* \langle \mathbf{v} \rangle_S + e^* \mathbf{A} = \langle \mathbf{p}_S \rangle = 0$, and taking the curl of Eq. (1.3) with the Maxwell equation $\nabla \wedge \mathbf{B} = \mu_0 \mathbf{j}$ we obtain

$$\nabla^2 \mathbf{B} = \frac{\mathbf{B}}{\lambda^2}, \quad (1.4)$$

implying that the external magnetic field is screened out from the interior of the sample. $\lambda_L = \sqrt{m^*/\mu_0 n_S e^{*2}}$ is the characteristic length known as the London penetration depth, in which the applied magnetic field exponentially decays to zero.

Assuming that the London hypothesis is correct, at $T = T_C$ we expect no superconducting carriers in the phase transition.

1.2. GINZBURG-LANDAU THEORY

Aiming to describe the evolution of the superconducting carriers and the superconducting current, the Ginzburg-Landau (GL) theory introduces a pseudo-wavefunction as an order parameter denoted by ψ , where the density of superconducting electrons which appears in the London equations would be described by $n_S = |\psi(x)|^2$. From the expression of the free energy and including expansion coefficients $\alpha(T)$ and $\beta(T)$, the GL free energy density when we apply a magnetic field is represented by

$$f_s(T) = f_n(T) + \frac{\hbar^2}{2m^*} \left| \left(\frac{\hbar}{i} \nabla + e^* \mathbf{A} \right) \psi \right|^2 + \alpha(T) |\psi|^2 + \frac{\beta(T)}{2} |\psi|^4, \quad (1.5)$$

resulting in the differential equation for ψ

$$-\frac{\hbar^2}{2m^*} \left(\nabla + \frac{e^* i}{\hbar} \mathbf{A} \right)^2 \psi + \beta |\psi|^2 \psi = -\alpha(T) \psi. \quad (1.6)$$

and the current operator would be written by

$$\mathbf{j}_S = \frac{i\hbar e^*}{2m^*} (\psi_A \nabla \psi_A^* - \psi_A^* \nabla \psi_A) - \frac{e^{*2}}{m^*} |\psi(x)|^2 \mathbf{A}. \quad (1.7)$$

We can observe that the first term corresponds to a paramagnetic current, meanwhile the second corresponds to a diamagnetic one. Taking into account that this theory is only true when the paramagnetic term is zero in the presence of a vector potential, the state of minimum energy fulfils $\psi_A \nabla \psi_A^* - \psi_A^* \nabla \psi_A = 0$, and we can apply first-order perturbation theory to obtain the wavefunction of the ground state

$$|\Psi_A\rangle = |\Psi_{A=0}\rangle + \sum_{n \neq 0} \frac{\langle \Psi_n | H_A | \Psi_{A=0} \rangle}{E_n - E_A} |\Psi_n\rangle, \quad (1.8)$$

where the second term is non-zero when $E_n - E_A > 0$. This means that there will be an energy gap around the Fermi energy, E_F . The GL effective mass is $m^* = 2m_e$, where m_e is the mass of the electron and $e^* = 2e$, being e the electron charge. With this choice $|\psi(x)|^2$ can be interpreted as the density of pairs of electrons in the ground state and the GL parameter m^* is the mass of the pair of electrons.

The GL theory gives rise to a characteristic length ξ , also named the GL coherence length, which defines the distance over which $\psi(\mathbf{r})$ can vary without energy increase,

$$\xi(T) = \frac{\hbar}{|2m^*\alpha(T)|^{1/2}}. \quad (1.9)$$

Both coherence length, $\xi(T)$, and penetration depth $\lambda(T)$, which can be expressed as $\lambda(T) = \sqrt{m^*\beta/\mu_0 e^{*2}\alpha(T)}$, diverge at T_c with the same dependence. However, the ratio between the two quantities, $\kappa = \lambda(T)/\xi(T)$ is temperature independent.

1.3. THE ABRIKOSOV FLUX LATTICE

In many superconductors the \mathbf{B} ($\mu_0\mathbf{H} = -\mathbf{M}$) field remains zero until it reaches a critical field H_c and the superconductivity is destroyed (Figure 1.1(a)). We will denote such examples as Type I superconductors. However, many other materials, known as type II superconductors, own two critical fields, labeled as the lower critical field, H_{c1} , and the upper critical field H_{c2} (Figure 1.1). Unlike type I, type II superconductors allow the

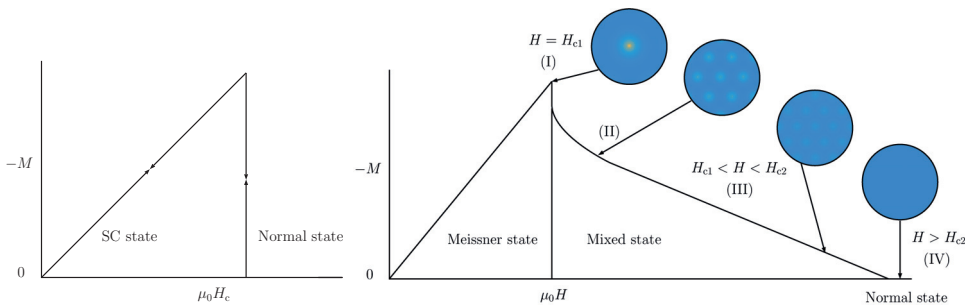


Figure 1.1: (Left) Schematic magnetization curve for type I superconductors. (Right) Schematic magnetization curve for type II superconductors. (I) At H_{c1} the first flux line penetrates the superconductor. (II) For higher fields, more flux lines appear and start to overlap when increasing the field and the bulk magnetization start to increase. (III) Close to H_{c2} the flux lines overlap to each other entering the normal state (IV).

magnetic field to enter into the sample in the form of vortices, between H_{c1} and H_{c2} . This last domain is called the mixed state (Figure 1.1(b)).

Abrikosov was the first to give an explanation of the transition between these two critical fields using the GL equations. Indeed, he described the difference between type I and type II superconductors as $\kappa < 1/\sqrt{2}$ and $\kappa > 1/\sqrt{2}$ respectively.

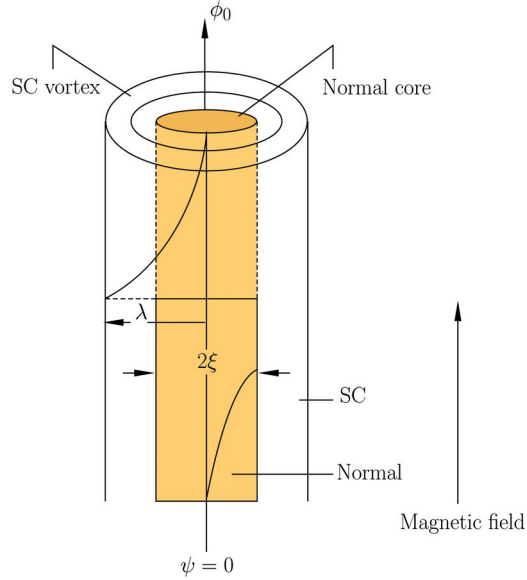


Figure 1.2: Structure of a vortex line.

In the mixed state the magnetic flux penetrates the superconductor in a regular array of flux tubes, each carrying a quantum flux $\Phi_0 = hc/2e$. As shown in Figure 1.2, within each unit cell, a superconducting current vortex concentrates the flux towards the center of the vortex and consequently, $|\psi|^2$ goes down to zero in the centers of the vortices. Abrikosov was the first to provide an explanation for this arrangement of the penetrating field in the form of a triangular or a squared lattice of vortices. This is usually known as the Abrikosov flux lattice or flux line lattice (FLL).

1.4. MICROSCOPIC BCS THEORY

Just as described in Eq. (1.8), it is necessary to have an energy gap, a macroscopic wavefunction to describe the superconducting carriers and a potential that keeps the two electrons coupled. This potential, proposed by Fröhlich, mediates the interaction by phonons, using the Thomas-Fermi model

$$V(\mathbf{q}) = \frac{4\pi e^2}{q^2 + q_{TF}^2} \left(1 + \frac{\omega_{\mathbf{q}}^2}{\omega^2 - \omega_{\mathbf{q}}^2} \right), \quad (1.10)$$

where \mathbf{q} is the momentum transfer and $\hbar\omega_{\mathbf{q}} = \epsilon(\mathbf{k} + \mathbf{q}) - \epsilon(\mathbf{k})$ is the energy difference close to the Fermi surface.

From this point, Cooper proposed a system that was formed by a pair of electrons and a blocked Fermi sphere. This means that the electrons inside the sphere act as motionless electrons and do not interact, so they are not involved in the resolution of the problem. Then, we look for a wavefunction for the pair of electrons, where at the minimum state of energy the total momentum is zero,

$$\Psi(\mathbf{r}_1, \mathbf{r}_2) = \sum_{\mathbf{k}} g(\mathbf{k}) e^{i\mathbf{k}\mathbf{r}_1} e^{-i\mathbf{k}\mathbf{r}_2}. \quad (1.11)$$

Taking into account the antisymmetry of the wavefunction with respect to the electron exchange, we introduce the antisymmetric spin singlet with a sum of $\cos(\mathbf{k} \cdot (\mathbf{r}_1 - \mathbf{r}_2))$. However, other types of interactions can permit different pairing symmetries.

Following this argument, the pairing Hamiltonian which describes the interaction between two electrons is given by

$$H_{e-e} = \sum_{\mathbf{k}, \sigma} \epsilon(\mathbf{k}) c_{\mathbf{k}, \sigma}^\dagger c_{\mathbf{k}, \sigma} + \frac{1}{2} \sum_{\mathbf{k}, \mathbf{k}', \mathbf{q}, \sigma, \sigma'} c_{\mathbf{k}+\mathbf{q}, \sigma'}^\dagger c_{\mathbf{k}-\mathbf{q}, \sigma}^\dagger c_{\mathbf{k}', \sigma'} c_{\mathbf{k}, \sigma} V_{\mathbf{k}, \mathbf{k}'}(\mathbf{q}). \quad (1.12)$$

To find the ground state in Eq. (1.12), the creation and annihilation operators are introduced for an electron with momentum \mathbf{k} and spin σ , $c_{\mathbf{k}\sigma}^\dagger$ and $c_{\mathbf{k}\sigma}$ respectively, so the Hamiltonian can be expressed in second quantisation notation as

$$\mathcal{H}_{\text{BCS}} = \sum_{\mathbf{k}, \sigma} \epsilon_{\mathbf{k}} n_{\mathbf{k}, \sigma} - V \sum_{\mathbf{k}, \mathbf{k}'} c_{\mathbf{k}'\uparrow}^\dagger c_{-\mathbf{k}\downarrow}^\dagger c_{-\mathbf{k}\downarrow} c_{\mathbf{k}\uparrow}. \quad (1.13)$$

Now to solve the energy spectrum of \mathcal{H}_{BCS} , we look for a wavefunction that will be the sum of all the pairs that we need. If $|0\rangle$ is the empty state, i.e. the quantum state which has no particles on it, then

$$|\Psi_N\rangle = \sum_{\mathbf{k}_1, \dots, \mathbf{k}_{N/2}} \underbrace{g(\mathbf{k}_1, \dots, \mathbf{k}_{N/2})}_{g(\mathbf{k}_1) \dots g(\mathbf{k}_{N/2}) \equiv \text{No pair correlation}} c_{-\mathbf{k}_{N/2}\downarrow}^\dagger c_{\mathbf{k}_{N/2}\uparrow}^\dagger \dots c_{-\mathbf{k}_1\downarrow}^\dagger c_{\mathbf{k}_1\uparrow}^\dagger |0\rangle. \quad (1.14)$$

As we can observe, we do not obtain any information about the system from this wavefunction, so BCS theory proposed that the system will not have a fixed number of particles, that is, there is a spontaneous symmetry breaking and the ground state takes the form of

$$|\Psi\rangle_{\text{BCS}} = \prod_{\mathbf{k}} (u_{\mathbf{k}} + v_{\mathbf{k}} c_{\mathbf{k}\uparrow}^\dagger c_{-\mathbf{k}\downarrow}^\dagger) |0\rangle, \quad (1.15)$$

with

$$\left. \begin{aligned} u_{\mathbf{k}}^2 &= \frac{1}{2} \left(1 + \frac{\epsilon_{\mathbf{k}}}{\sqrt{\Delta^2 + \epsilon_{\mathbf{k}}^2}} \right) \\ v_{\mathbf{k}}^2 &= \frac{1}{2} \left(1 - \frac{\epsilon_{\mathbf{k}}}{\sqrt{\Delta^2 + \epsilon_{\mathbf{k}}^2}} \right) \end{aligned} \right\} \quad (1.16)$$

where $|u_{\mathbf{k}}|^2 + |v_{\mathbf{k}}|^2 = 1$ and Δ is the BCS superconducting gap and the order parameter of the system.

Diagonalizing the expression Eq. (1.13), the eigenvalues of the Hamiltonian are

$$E_{\mathbf{k}} = \sqrt{\Delta^2 + \epsilon_{\mathbf{k}}^2}. \quad (1.17)$$

If the sample is in the normal state, then $\Delta = 0$, and the energy for adding an electron to an empty state would be $+\epsilon_{\mathbf{k}}$ and if an electron is removed (or a hole is created) then the energy would be $-\epsilon_{\mathbf{k}}$. In the superconducting state the excitation energies become modified by $+E_{\mathbf{k}}$ (or $-E_{\mathbf{k}}$) for adding (or removing) a quasiparticle. Because $+E_{\mathbf{k}}$ is greater than Δ and $-E_{\mathbf{k}}$ is lower than $-\Delta$, the minimum energy to make an excitation is 2Δ . At $T = 0$, Bardeen, Cooper and Schrieffer found that the superconducting gap is related to the critical temperature by

$$2\Delta(0) = 3.52k_B T_c. \quad (1.18)$$

1.5. UNCONVENTIONAL SUPERCONDUCTIVITY

Over the past few years, many superconductors have been described with pair bound states that differ from those in BCS theory. Instead of using the zero angular momentum, $l = 0$, s -wave state, they arise from $l = 1$ and $l = 2$ bound states. These kinds of material are known as unconventional superconductors and some examples that present this type of pairing mechanism are the so-called heavy fermion materials, such as UPt₃, UBe₁₃, or CeCu₂Si₂ (we will discuss them in depth in Chapter 3).

If we consider the electron-phonon coupling previously described and the construction of a two-electron bound state wavefunction from plane waves, we can still achieve the antisymmetry of the two-electron wavefunction with either singlet or triplet spin pairing, depending on whether we choose to write the orbital wavefunction as a sum of even or odd functions of $(\mathbf{r}_1 - \mathbf{r}_2)$. Then, it is possible to find some materials with this non-BCS coupling, even when the electron-phonon coupling is not strong.

In BCS theory we have the order parameter given by the energy gap at the Fermi surface Δ , and it has the same value for all vectors of reciprocal space, $\Delta_{\hat{R}\mathbf{k}} = \Delta_{\mathbf{k}}$, conserving any symmetry operator in the point group. That means that we can apply any rotation to our Brillouin zone, and the order parameter Δ will be invariant under such a permutation. This means that unconventional superconductivity is associated with $\Delta_{\hat{R}\mathbf{k}} \neq \Delta_{\mathbf{k}}$ for at least one symmetry operation.

Taking as an example a two-dimensional square Brillouin zone and the definition of Δ , the most common pairing symmetries are given by

$$\Delta_{\mathbf{k}} = \Delta \quad (s), \quad (1.19a)$$

$$\Delta_{\mathbf{k}} = \Delta[\cos(k_x a_0) + \cos(k_y a_0)]/2 \quad (s^- \text{ or nodal } s\text{-wave}), \quad (1.19b)$$

$$\Delta_{\mathbf{k}} = \Delta[\cos(k_x a_0) - \cos(k_y a_0)]/2 \quad (d_{x^2-y^2}), \quad (1.19c)$$

$$\Delta_{\mathbf{k}} = \Delta \sin(k_x a_0) \sin(k_y a_0) \quad (d_{xy}), \quad (1.19d)$$

where here a_0 is the crystal lattice constant of the square lattice and the limits of the first Brillouin zone are $-\pi/a_0 \leq k_x \leq \pi/a_0$ and $-\pi/a_0 \leq k_y \leq \pi/a_0$, (Figure 1.3).

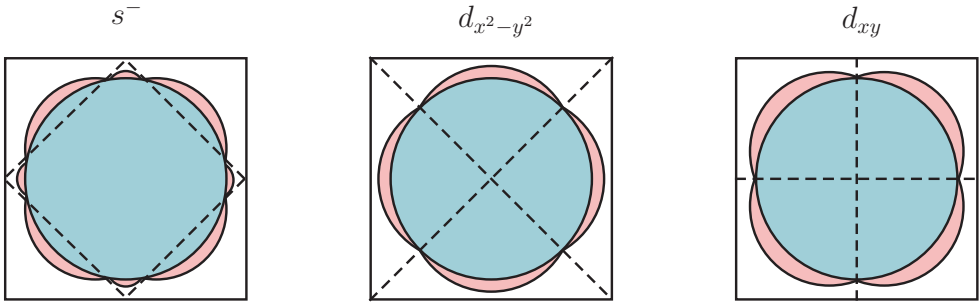


Figure 1.3: Three extra symmetry pairings for a tetragonal sample. The s -nodal s^- (left) with eight nodes of the gap function, and the two d -pairing, $d_{x^2-y^2}$ (middle) and d_{xy} (right), both of them with four gap nodes.

Either the conventional s -pairing (Eq. (1.19a)) and the s -nodal pairing (Eq. (1.19b)) are constant under all possible symmetry rotations. However, the two gap functions in Eq. (1.19c) and Eq. (1.19d) are unconventional pairing symmetries because they change the sign of the gap under a rotation. Because the gap functions have the same symmetry as d spherical harmonic functions, $d_{x^2-y^2}$ and d_{xy} , they are usually known as d -wave gap functions, and the gap function vanishes at four different points (four-fold).

CHAPTER 2

Small-angle neutron scattering

Long range ordered magnetic structures such as flux-line lattices from type-II superconductors, skyrmions and spin structures where the repeat length is too large for conventional neutron diffraction instruments can be resolved by using Small-Angle Neutron Scattering (SANS) [3]. In our case, SANS experiments cannot only provide us information of the characteristic lengths of the superconductors but also the pairing symmetry of the superconducting gap [4].

In this chapter, we will explore the theory behind flux-line lattice neutron scattering and the different techniques used for obtaining the underlying physical information.

2.1. ELEMENTAL NEUTRON SCATTERING

The position of atoms in real space is described by a basis of three primitive vectors $\mathbf{r} = n_1\mathbf{a}_1 + n_2\mathbf{a}_2 + n_3\mathbf{a}_3$, being n_i integers. In reciprocal space, this is expressed as $\mathbf{G} = m_1\mathbf{b}_1 + m_2\mathbf{b}_2 + m_3\mathbf{b}_3$, where $\mathbf{a}_i\mathbf{b}_i = 2\pi\delta_{ij}$ and m_i are also integers.

In neutron scattering theory, the propagation vectors for the incident and diffracted neutrons are given by \mathbf{k}_i and \mathbf{k}_f , which are related by the momentum transferred, \mathbf{q} , such that

$$\mathbf{k}_f = \mathbf{k}_i + \mathbf{q}. \quad (2.1)$$

In elastic neutron scattering, energy is conserved, so $\mathbf{k}_i = \mathbf{k}_f$ and from the Laue condition, $\mathbf{G} = \mathbf{q}$, we can generate Bragg's law, expressed as

$$q = 2k \sin \theta \quad (2.2)$$

where 2θ is the scattering angle. If we consider the Bragg condition for plane spacings of length d with wavelength $\lambda_n = 2\pi/k$, then Bragg's law can be rewritten as $\lambda_n = 2d \sin \theta$. For a more visual interpretation of the scattering condition we construct the Ewald sphere as shown in Figure 2.1.

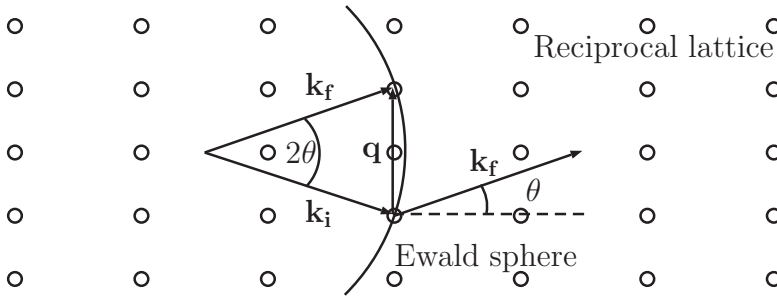


Figure 2.1: Ewald sphere construction, where the difference between the incident and diffracted scattering vectors is given by q . The radius is determined by the wavelength.

In elastic neutron scattering, the radius of the Ewald sphere is determined by the incident wavelength $\lambda = 2\pi/k$, and the surface lies at the end of the vector \mathbf{k}_i . The scattering condition will be fulfilled when the surface crosses two reciprocal lattice points.

2.1.1. Differential scattering cross section

The intensity from the diffracted pattern is proportional to the differential cross section, which describes the number scattered of neutrons into a solid angle per second, normalized by the incident flux,

$$\frac{d\sigma}{d\Omega} = \left| \sum_n b_n e^{i\mathbf{q}\cdot\mathbf{r}_n} \right|^2, \quad (2.3)$$

where n is the number of scattering objects (e.g. atoms or flux lines) and b_n is the scattering length for each one. For nuclear scattering, this scattering length is characterized for every

single element or ion. When calculating the nuclear scattering for a single unit cell and for all the unit cells of the crystal, we arrive at the nuclear differential scattering cross section

$$\frac{d\sigma}{d\Omega_{\text{nuclear}}} = \frac{(2\pi)^3}{V_0} N \sum_{\mathbf{Q}} \delta(\mathbf{q} - \mathbf{Q}) |F(\mathbf{q})|^2 \quad (2.4)$$

where $F(\mathbf{q}) = \sum_m b_N e^{i\mathbf{q}\cdot\mathbf{r}_N}$ is the nuclear structure factor, which will be proportional to the detected intensity; \mathbf{r}_N expresses all the positions inside the unit cell and the sum over the delta function covers all of the reciprocal lattice vectors \mathbf{Q} .

2.2. MAGNETIC SCATTERING

Since neutrons have a magnetic moment, they can also be used to detect the magnetic structure of a sample. Therefore, the scattering length can be split into two terms, one giving the nuclear contribution b_N and a second one denoting the magnetic component b_M , $b = b_N + b_M$ with $b_M = \hat{\sigma} \cdot b_M$, denoting the orientation of the neutron spin. The magnetic scattering length may be written as

$$b_M = \frac{V(\mathbf{q})}{4\pi\hbar^2/2m_n} f(\mathbf{q}) \quad (2.5)$$

where $f(\mathbf{q})$ is the Fourier transform of the electron density and $V(\mathbf{q})$ is the Fourier transform of the magnetic potential, which can be expressed in terms of the neutron gyromagnetic ratio $\gamma = 1.91$ and the nuclear magneton $\mu_N = e\hbar/2m_n$,

$$V(\mathbf{q}) = 4\pi\gamma\mu_N\mu_B\hat{\sigma} \cdot \hat{\mathbf{q}} \times (\hat{\mu} \times \hat{\mathbf{q}}), \quad (2.6)$$

where μ_B is the Bohr magneton, $\hat{\mathbf{q}}$ is the unitary vector of the scattering vector and $\hat{\mu}$ is the unitary vector of the magnetic moment. As we can observe from the last expression, only the component of μ which is perpendicular to \mathbf{q} will give scattering.

2.2.1. Magnetic scattering of the flux-line lattice

Type-II superconductors present a flux-line lattice with a large magnetic periodicity, which implies that it can be detected using neutron scattering Ref. [5].

As mentioned in Eq. (2.5), the magnetic potential will determine the magnetic scattering length expression. If we express the magnetic field that passes through the sample in the Abrikosov state as a Fourier series

$$B(\mathbf{r}) = \sum_{\mathbf{q}} |FF(\mathbf{q})| e^{i\mathbf{q}\cdot\mathbf{r}} \quad (2.7)$$

then the Fourier components of the magnetic field $|FF(\mathbf{q})|$ are known as the form factor. In reciprocal space, $B(\mathbf{q}) = A_0 t |FF(\mathbf{q})|$, where $A_0 = \phi_0/B$ is the area of one unit cell and t is the sample thickness. Knowing that the magnetic flux quantum is equivalent to $\phi_0 = h/2e$, the scattering length will be given by

$$b_{\text{FLL}} = \frac{\gamma}{4\Phi_0} A_0 t \hat{\sigma} |FF(\mathbf{q})|, \quad (2.8)$$

and the final differential scattering length from the flux-line lattice

$$\frac{d\sigma}{d\Omega_{\text{FLL}}} = (2\pi)^3 \left(\frac{\gamma}{4\Phi_0} \right)^2 A_{\text{sample}} t \sum_{\mathbf{Q}} \delta(\mathbf{q} - \mathbf{Q}) |FF(\mathbf{q})|^2. \quad (2.9)$$

However, the Bragg peaks are not pure δ -functions because of the imperfections of the sample and the limited instrumental resolution and they are usually approximated to a Gaussian function or to a Lorentzian.

For calculating the form factor, we rotate the sample with respect to the incident beam and then calculate the integrated intensity for a particular Bragg reflection. If the sample rotates around one of its axis, in the frame shown in Figure 2.2 the \mathbf{y} -axis, then the sample will rotate with an angular speed ω and the total number of scattered neutrons will be given by

$$N = \phi_n \int d\Omega \int dt \frac{d\sigma}{d\Omega} = I_0 \int \frac{dy dz}{k^2} \int \frac{dx d\sigma}{v d\Omega} \quad (2.10)$$

where ϕ_n is the incident neutron flux per area per time, and v is the space-velocity of the reflection moving across the Ewald sphere. Taking into account the Lorentz correction, which is introduced depending on how the sample is rocked, $v = q\omega \cos(\zeta)$, where ζ is the angle between the reciprocal lattice vector \mathbf{q} and the direction perpendicular to the rocking axis, commonly known as Lorentz factor (sketched in Figure 2.2).

By replacing Eq. (2.9) in Eq. (2.10) and normalizing by the sample area, the integrated intensity is related to the form factor by the Christen formula [6]

$$I = N\omega = 2\pi V \phi_n \left(\frac{\gamma}{4} \right)^2 \frac{\lambda_n^2}{\Phi_0^2 q_{hk} \cos(\zeta)} |FF(\mathbf{q}_{hk})|^2, \quad (2.11)$$

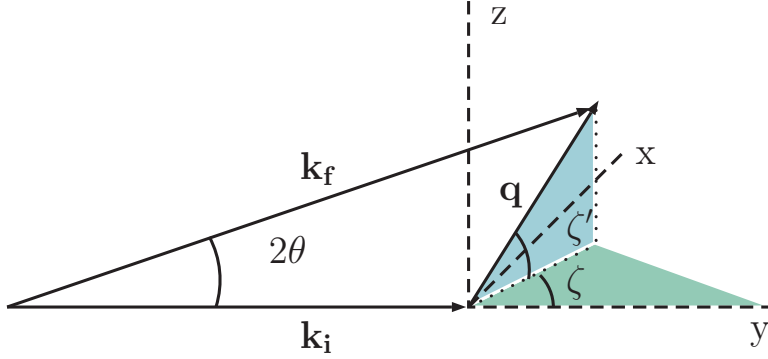


Figure 2.2: Reference frame for calculation of the Lorentz factor correction, ζ or ζ' , depending on the rocking direction.

where $\gamma = 1.91$ is the magnetic moment of the neutron in nuclear magnetons, λ_n is the chosen wavelength, V is the sample volume, q_{hk} is the magnitude of the scattering vector and $\cos(\zeta)$ is the Lorentz factor previously discussed. For a well-ordered vortex lattice, the magnitude of $FF(\mathbf{q}_{hk})$ is related to the penetration depth, λ , and coherence length, ξ , and performing measurements in absolute values, it is possible to estimate the characteristic lengths for a particular superconductor.

2.2.1.1. Flux-line lattice form factor

The FLL form factor provides information about the density of states (DOS) and the penetration depth of the system at a specific temperature.

For superconductors with large GL parameter $\kappa = \lambda/\xi \gg 1$ (where ξ is the coherence length) at not too large fields $H_{ext} \ll H_{c2}$ (and H_{c2} is the upper critical field) we may approximate the vortex fields by the London model. Making use of the London equation (Eq. (1.4)) and including the Fourier transform of the magnetic field in Eq. (2.7), a new standard expression is obtained depending on the applied magnetic field and the London penetration depth [7],

$$FF(q)_{\text{London}} = \frac{B}{1 + (\lambda q)^2}. \quad (2.12)$$

This equation disregards the effect of the finite size of the vortex cores and thus reduces the amplitude of the greater form factors. for $H \ll H_{c2}$, this effect is rectified multiplying

the London solution of Eq. (2.12) by a cut-off factor, initially introduced by Brandt [7–10],

$$FF(q)_{\text{Brandt}} = \frac{B}{1 + (\lambda q)^2} e^{-c(\xi q)^2}. \quad (2.13)$$

Here the constant c is typically between 1/4 and 2 [7]. For $(\lambda q)^2 \gg 1$ for all relevant fields the prefactor in Eq. (2.13) is reduced to $\phi_0 = (2\pi\lambda)^2$.

If we want to take into account very low fields $H \ll H_{c2}$, we have to derive the low-field cutoff factor from analytical solutions of the GL theory. Considering an isotropic superconductor, Clem proposed an analytical expression [7, 11] for large $\kappa \gg 1$,

$$FF(q)_{\text{Clem}} = B \frac{gK_1(g)}{1 + (\lambda q)^2} \quad (2.14)$$

where $g = \sqrt{2}\xi(q^2 + \lambda^{-2})^{1/2}$. Here ξ is the coherence length and $K_1(x) = K'_0(x)$ is a first order modified Bessel function. As we can observe, if the size of the core tends to zero, we recover the London expression of Eq. (2.12). The cutoff factor $gK_1(g)$ in Eq. (2.14) can be approximated by $\exp(-2\xi^2 q^2)$ or by $\exp(-\xi^2 q^2/4)$ [9] returning to the solutions suggested by the Brandt model [7].

Clem's analytical solution was extended by Hao [7, 12] to cover anisotropic superconductors and higher magnetic fields, resulting in a form factor given by

$$FF(q)_{\text{Hao}} = B \frac{f_\infty K_1 \left[\frac{\xi_\nu}{\lambda} (f_\infty^2 + \lambda^2 q^2)^{1/2} \right]}{(f_\infty^2 + \lambda^2 q^2)^{1/2} K_1 \left(\frac{\xi_\nu}{\lambda} f_\infty \right)} \quad (2.15)$$

where

$$\xi_\nu = \xi \left(\sqrt{2} - \frac{0.75}{\kappa} \right) (1 + b^4)^{1/2} [1 - 2b(1 - b)^2]^{1/2} \quad (2.16)$$

is the effective core radius of a single vortex and

$$f_\infty^2 = 1 - b^4 \quad (2.17)$$

represents the depression in the order parameter due to the overlap between vortex spots.

Here $b = B/B_{c2}$ and $\kappa = \lambda/\xi$ is the Ginzburg-Landau parameter.

2.3. SMALL-ANGLE NEUTRON SCATTERING

Several techniques can be used in the detection of vortex lattices in type-II superconductors, such as scanning tunneling microscopy (STM), scanning-SQUID microscopy, magnetic force microscopy (MFM) or muon spin rotation (μ SR). However, some of these are limited, either because they are only surface sensitive or because they are limited by small fields. Small-Angle Neutron Scattering (SANS) presents some advantages, because it is a bulk technique able to probe the vortex lattice distribution through the magnetization contrast created by the vortices and can be done under high external magnetic fields.

SANS is based on the fact that neutrons have a spin, and therefore, an associated magnetic moment that interacts with the magnetic field distribution generated by the VL of the superconducting sample. SANS is employed for structures on length scales between 10 \AA and 10^4 \AA which correspond to a scattering vector of about 10^{-1} \AA^{-1} and 10^{-4} \AA^{-4} . To have reasonable scattering angles we typically use wavelengths between 5 \AA and 15 \AA for our experiments.

2.3.1. SANS Instrumentation

Our experiments were performed at different research facilities. Most of them were performed on monochromatic instruments, such as D11 and D33 at ILL, SANS-I and SANS-II at SINQ and NG7 at NIST; but other experiments were performed in TOF instruments, in particular the HFM/EXED instrument at HZB.

Following [Figure 2.3](#), for a monochromatic SANS spectrometer, cold neutrons (with a wavelength between 0.2 and 2 nm) pass through a velocity selector, which consists of a drum that rotates with a certain speed and rotation angle, capable of selecting a specific wavelength and bandwidth. To define the divergence of the neutron beam, it is collimated before interacting with the sample. The sample is placed on a sample holder inside a suitable cryostat or magnet. Since the vortex spacing is about 10 - 400 nm , the scattering angle is usually no more than a degree so we usually rock the sample in two different

directions perpendicular to the neutron beam. The scattered neutrons are collected by a position sensitive detector and the unscattered beam is absorbed by a beamstop located at the centre of the detector. The collimation apertures and the detector are in vacuum to reduce air scattering and letting the scattered neutrons being unaffected by the neutron beam.

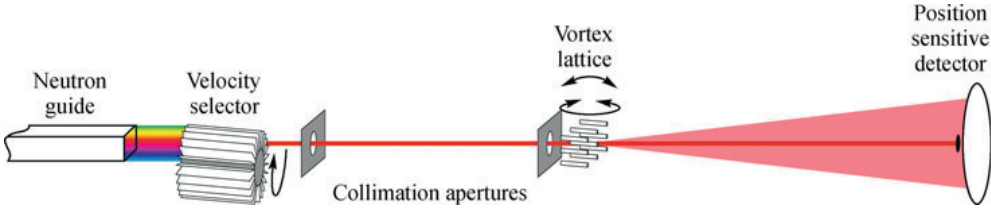


Figure 2.3: Scheme of a Small-Angle Neutron Instrument taken from [8].

2.3.1.1. TOF instrumentation

Some SANS instruments are instead operated in a time-of-flight (TOF) mode. In TOF instruments, the sample interacts with a pulse of multichromatic neutrons produced by a chopper and then the scattered neutrons are recorded at the detector at different times, depending on their velocity, and hence wavelength. With this technique, the scattering information is recorded at a single position of the detector. The accessible Q -range is wider than in the monochromatic case, reaching from 10^{-2} to 1 nm^{-1} [13]. However, the data analysis requires a different treatment which will be further explained in the next section.

2.3.2. FLL form factor analysis

To obtain the form factor it will be necessary to calculate the integrated intensity of one Bragg reflection. By rotating the sample, we rock the first-order FLL Bragg reflections through the Ewald sphere and collect intensities for every single angle we placed our sample, resulting in a rocking curve as shown in Figure 2.4. The rocking curve is usually fitted to either a Lorentzian or a Gaussian function. Typically, the rocking curve from the first-order Bragg reflections of the FLL is overlapped by unscattered neutrons or signal

coming from the crystal structure. To make the rocking curve clearer, we also perform some background measurements when the sample is not in the superconducting state, by measuring the intensity at the same rocking angles either above the critical temperature of the superconductor or at zero field, or more rarely, at fields greater than H_{c2} .

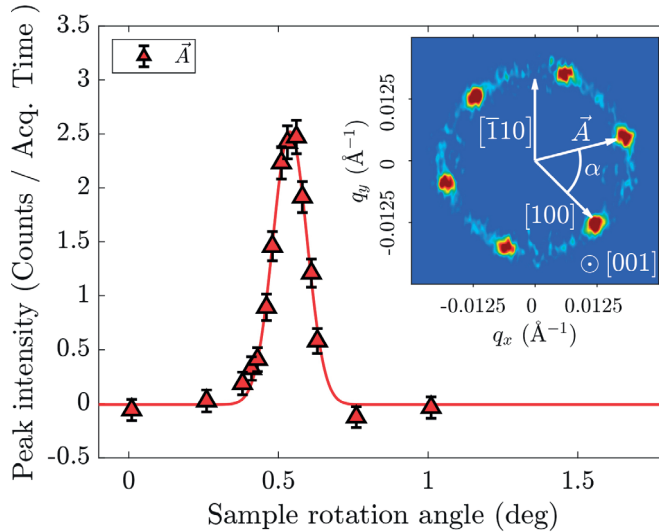


Figure 2.4: Example of a rocking curve from the Bragg reflection \vec{A} measured at 1.6 T and 130 mK, fitted to a Gaussian. (Inset) flux-line lattice diffraction pattern of CeCu_2Si_2 measured at 1.6 T and 130 mK, obtained by summing all intensities measured at different rocking angles (Paper III).

Once fitted, the obtained integrated intensity can be taken, along with the Lorentz correction information and the q -position of the Bragg reflection on the detector, and used in Eq. (2.11) to extract the form factor associated with it. Finally, in order to obtain a more accurate value of the form factor and to reduce the uncertainty, we average the values of the individual form factors obtained from all the first-order FLL Bragg reflections measured at a certain temperature and magnetic field. This subtraction and fitting is performed using GRASP, a program written in MATLABTM for the visualization of data and analysis of SANS experiments [14].

2.3.2.1. FLL form factor analysis for TOF instruments

As mentioned in Section 2.3.1.1, time-of-flight instruments do not have a velocity selector and a multichromatic neutron beam interacts with the sample. For this reason, there is no need to rotate the sample to catch the complete rocking curve, since first-order Bragg reflections are cut by different Ewald spheres defined by the wavelength of incident neutrons. Because of this, the procedure for calculating the form factor deviates from the monochromatic one and needs a redefined Christen equation which takes into account the dimensions of the TOF detector. This method is fully developed in Paper I.

For the Christen equation, Eq. (2.11), the total intensity detected is normalized to the total flux, $I/\phi_n\lambda_n^2$, in a single pixel of the detector is integrated over $qd\omega$, as we previously discussed in Eq. (2.10). However, in this case, we have to find out the integrated intensity contained in a spot (q_x, q_y) as a function of q , therefore, finding the density of detector pixels in q -space will make the integration possible over q_x, q_y .

Considering an incident neutron with wavelength $\lambda_n = 2\pi/k$, for SANS experiments, the distance between the sample and the detector pixel where the scattered neutron is detected is essentially constant, r , and from the lab frame q is given by Eq. (2.1). Defining the position of the detector pixel (x, y) , we can redefine q in the sample frame

$$q = k \left(\frac{x}{r} \right) \hat{x} + k \left(\frac{y}{r} \right) \hat{y} + k \left[\left(\frac{x}{r} \right)^2 + \left(\frac{y}{r} \right)^2 \right] \hat{z}. \quad (2.18)$$

If we rotate the sample with respect to the beam by an angle α , q' in the sample frame will be given by

$$q'_x = q_x \cos \alpha + q_z \sin \alpha, \quad (2.19a)$$

$$q'_y = q_y, \quad (2.19b)$$

$$q'_z = q_z \cos \alpha - q_x \sin \alpha, \quad (2.19c)$$

and considering that q_z and α are small, we arrive to

$$q'_x \approx q_x = k \left(\frac{x}{r} \right) \quad (2.20a)$$

$$q'_y = q_y = k \left(\frac{y}{r} \right) \quad (2.20b)$$

$$q'_z \approx q_z - q_x \sin \alpha. \quad (2.20c)$$

Hence the relationship between distances in the detector and the q -space pixels in sample frame will be

$$\frac{dq'_x}{dx} = \frac{k}{r} = \frac{dq'_y}{dy}. \quad (2.21)$$

For obtaining the intensity of a single q -space pixel, $I(q_{x,i}, q_{y,j})$, we first divide the foreground and the background by the direct beam separately and after that we then subtract the background. This subtraction, binnings and fittings are performed using Mantid [15].

A sum over q_x, q_y will depend on the size of the q -pixels and accordingly on the number of detector pixels, n , inside of a q -space area. If we sum over $\Delta q'_x \Delta q'_y$, it will correspond to the detector area $\Delta x \Delta y = \Delta q'_x \Delta q'_y r^2 / k^2$ and the number of pixels will be

$$n = \frac{\Delta x \Delta y}{\delta x \delta y} = \frac{\Delta q'_x \Delta q'_y r^2}{k^2 \delta x \delta y} \quad (2.22)$$

where $\delta x, \delta y$ are the dimensions of a single detector pixel and the expression summed over q_x, q_y gets independent of wavelength

$$I(q_z) = \sum_i^n \sum_j^n n \frac{I(q_{x,i}, q_{y,j})}{\phi_n \lambda_n^2} = \sum_i^n \sum_j^n \frac{\Delta q'_x \Delta q'_y}{4\pi^2} \left(\frac{r^2}{\delta x \delta y} \right) \frac{I(q_{x,i}, q_{y,j})}{\phi_n}. \quad (2.23)$$

giving a final q_z -dependent intensity, which, in turn, will depend on the maximum and minimum wavelengths of the beam, since $\delta q_z = (q_x^2 + q_y^2) \delta \lambda / 2\pi$. Finally, by fitting $I(q_z)$ by a Gaussian function with height I_{0,q_z} and width σ_{q_z} , this will give the suitable integrated intensity for calculating the form factor

$$FF_{\text{TOF}} = \left(\sqrt{2\pi} I_{0,q_z} \sigma_{q_z} \right) \frac{\Phi_0^2 A_{\text{sample}}}{2\pi V} \left(\frac{4}{\gamma} \right)^2. \quad (2.24)$$

Resolution considerations are discussed in [Paper I](#).

2.4. BAYESIAN REDUCTION OF THE FLUX-LINE LATTICE

When processing the flux-line lattice information, it is possible that there will be missing information because the lattice perfection is affected by pinning effects and thermal fluctuations. The broadening of the Bragg spots is also affected by the wavelength spread,

the beam size and the divergence. Usually, to visualize a flux-line lattice picture, we sum all the intensities contained in every pixel for all the angles we measure at, and we subtract the background measured at the same positions. However, this method presents several disadvantages. One of them is that Bragg spots closer to the rocking axis intersect the Ewald sphere over a wider range of angles compared to those reflections far away from the rotation axis. This makes the closer Bragg spots have stronger intensities than the rest, motivating the inclusion of the Lorentz factor previously mentioned in Eq. (2.11). Another problem that may arise is the use of unweighted sums. For some high-quality crystals, in which Bragg spots are only visible over a small number of angles, including angles with no scattered intensity to the sum will increase the noise level in the final picture. To avoid these problems a weighted sum can be included to reduce the amount of noise but this can cause problems for those reflections that never cut the Ewald sphere if they are too close to the rocking axis. One approach to overcome these problems is by applying Bayes' theorem to the flux-line lattice data reduction process [16].

2.4.1. Application of Bayes' theorem to FLL processing

From Bayes' theorem, for an event A with non-zero probability and where B is an event of which the conditional probability $P(B|A)$ is known, the conditional probability $P(A|B)$ is given by Bayes' theorem

$$P(A|B) = \frac{P(B|A)P(A)}{P(B)}, \quad (2.25)$$

where $P(A|B)$ is the likelihood of event A given B , $P(B|A)$ is likelihood of event B given A and $P(A), P(B)$ are the probabilities of observing A and B individually.

To apply this theorem to the optimized reduction of the FLL, we considered the FLL as a two-dimensional picture and define a correlation length along q_z

$$I_{3D}(q_x, q_y, q_z) = f(q_z)I_{2D}(q_x, q_y) \quad (2.26)$$

where $f(q_z)$ defines the rocking curve given by a Lorentzian where Γ is the FWHM

$$f(q_z) = \frac{1}{\pi} \frac{\frac{1}{2}\Gamma}{(\frac{1}{2}\Gamma)^2 + q_z^2} \quad (2.27)$$

or a Gaussian with width γ

$$f(q_z) = \frac{1}{\sqrt{2\pi}\gamma} \exp\left(-\frac{q_z^2}{2\gamma^2}\right). \quad (2.28)$$

Assuming a Lorentzian-shaped rocking curve and working with data already normalized and with the background subtracted, we have a set of 2D arrays of counts measured at a range of rocking angles, $\{\omega_j\}$, where the intensity of a single pixel for a particular angle is D_{ij} with error σ_{ij} . Taking into account all these terms, we want to calculate the probability of finding the integrated intensity I_i for a single pixel, given a set of q -values, $\{\mathbf{q}_i\}$ and experimental data $\{D_{ij}\}$.

As a result, from Eq. (2.26), the expected intensity measured at pixel i and frame j will be $f_{ij}I_i$ and the Bayes' theorem applied for a single pixel and frame

$$P(I_i|\{D_{i,j}\}, \mathcal{H}) = \frac{P(\{D_{i,j}\}|I_i, \mathcal{H})P(I_i|\mathcal{H})}{P(\{D_{i,j}\}|\mathcal{H})} \quad (2.29)$$

where \mathcal{H} represents our model, background and the rocking curve shape assumed, the likelihood is given by $P(\{D_{i,j}\}|I_i, \mathcal{H})$, the prior is $P(I_i|\mathcal{H})$ and $P(\{D_{i,j}\}|\mathcal{H})$ is treated as a normalizing constant.

Considering that both foreground and background have Poisson distributions, the data will have a probability distribution given by the convolution of both functions, approximately a Gaussian with mean $f_{i,j}I_{i,j}$ and variance $\sigma_{i,j}^2$

$$P(D_{i,j}|I_i, \mathcal{H}) = (2\pi\sigma_{i,j}^2)^{-1/2} \exp\left[-\frac{(D_{i,j} - f_{i,j}I_{i,j})^2}{2\sigma_{i,j}^2}\right] \quad (2.30)$$

and assuming that the prior is given also by a Gaussian of mean μ and variance ξ^2

$$P(I_i|\mathcal{H}) = (2\pi\xi^2)^{-1/2} \exp\left[-\frac{(I_i - \mu)^2}{2\xi^2}\right]. \quad (2.31)$$

Inserting Eq. (2.30) and Eq. (2.31) in Eq. (2.29) and optimizing $P(D_{i,j}|I_i, \mathcal{H})$, the value of I_i which maximizes $P(I_i|\{D_{i,j}\}, \mathcal{H})$ can be expressed as

$$I_i = I_0 + \sum_j w_{ij} \cdot D_{ij} \quad (2.32)$$

where I_0 is proportional to μ and can be treated as a constant for all pixels and the weights are given by the expression

$$w_{ij} = \frac{f_{ij}/\sigma_{ij}^2}{1/\xi^2 + \sum_j f_{ij}^2/\sigma_{ij}^2}. \quad (2.33)$$

As we previously mentioned, f_{ij} can be extrapolated from the Lorentzian function with FWHM Γ , $\{\sigma_{ij}\}$ is averaged over all angles and each pixel and ξ should be chosen to be wide enough to include all the expected values for the intensities.

To extend this last expression over multiple pixels, we treat all pixels as independent so that individual probabilities can be multiplied to find a complete probability for the whole detector. Since we are only interested in the visible Bragg reflections, we mask the regions without diffracted intensity to help the calculation and reduce noise.

By using this method, regions with large intensity will have a bigger impact on the final result than those with zero detected intensity.

2.4.2. Visualization of the vortex lattice

This Bayesian statistical treatment has been applied to several SANS diffraction patterns for different papers, in particular Figures 1 and 2 (a) in Paper III [18]; Figure 3 (b) in Paper II [19]; and Figures 2 (d)-(g) in paper Paper VII [17] (see Figure 2.5).

In Figure 2.5 (a) the diffraction pattern measured in β -Bi₂Pd at 0.87 K and 0.2 T is shown, as obtained by rocking about the horizontal axis. We can observe the difference in intensity between the on- and off-axis spots, where off-axis spots have a FWHM larger by a factor of $1/\cos\alpha$ (see Lorentz factor in Section 2.2.1). As mentioned before, those areas which fulfil the Bragg condition, i.e. those with visible spots with well-defined rocking curves (Figure 2.5 (b)-(c)), can be easily processed through Bayesian analysis.

Figure 2.6 represents the sum of all the weighting coefficients, w_{ij} , taken at different ω (about the vertical axis) and ϕ (about the horizontal axis) angles calculated from Eq. (2.33). As we explained, those areas where the Ewald sphere is expected to intersect with the reciprocal space of the crystal should have greater values than the rest. The areas that have been completely masked have no weighting contribution. One consequence from Eq. (2.33) is that if the rocking curves have a wide FWHM they can provide information on unseen Bragg spots. Another result, especially if the rocking curves are too narrow, is that they will produce a maximum in one of the frames but a minimum in the others.

By providing scans along the vertical and horizontal axis, we can get a complete set of information to reconstruct the full vortex lattice, as shown in Figure 2.5 (d)-(g).

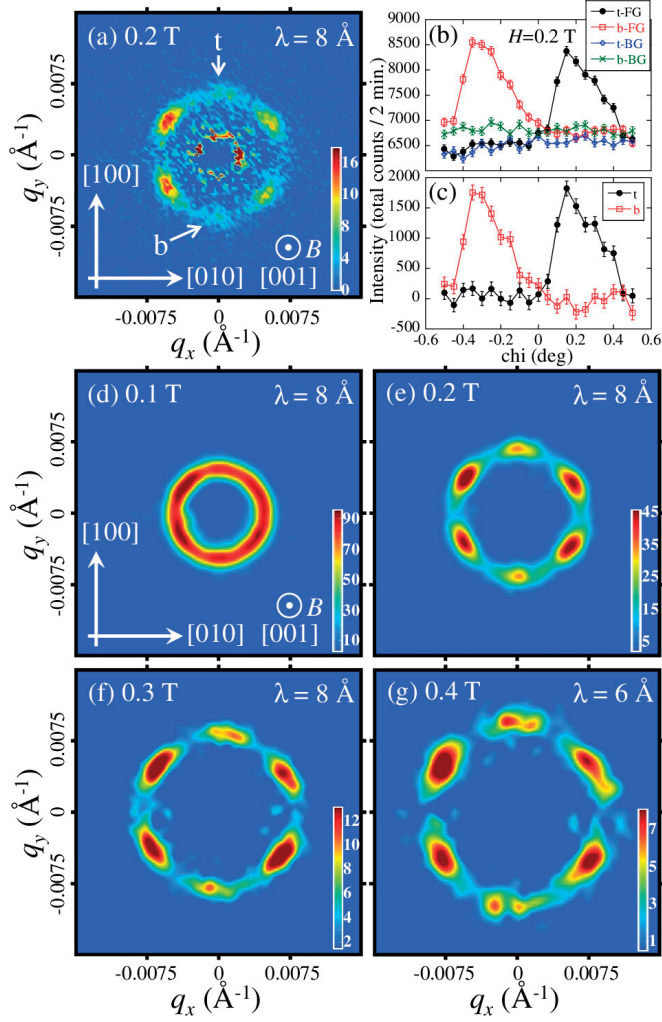


Figure 2.5: Example of a SANS pattern measured in β -Bi₂Pd at 0.87 K and 0.2 T nearly parallel to the c -axis of the sample. Smoothing and Bayesian analysis were not performed. (b) Rocking curves dependences of the FG ($T=0.87 \text{ K}$) and BG ($T=5.5 \text{ K}$) raw intensities at 0.2 T. The intensities correspond to the top, t , and bottom, b , spots. (c) Rocking curves dependences of t and b spot intensities at 0.87 K and 0.2 T after subtracting the background. (d)–(g) Typical Bayesian SANS patterns at 0.87 K from the VL in β -Bi₂Pd at (d) 0.1 T, (e) 0.2 T, (f) 0.3 T, and (g) 0.4 T [17]. Pictures have been smoothed after Bayesian analysis.

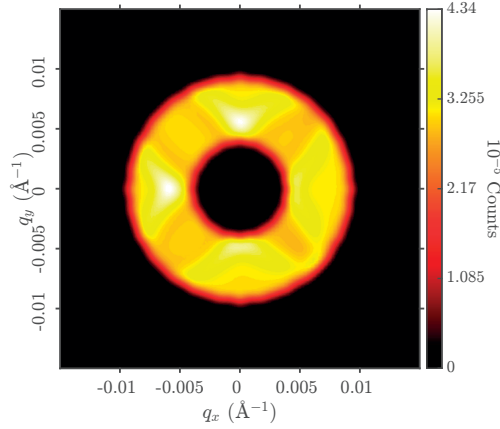


Figure 2.6: Sum of all the weighting contributions for all the ω_i and ϕ_i frames obtained from the Bayesian analysis of β -Bi₂Pd of Figure 2.5(a).

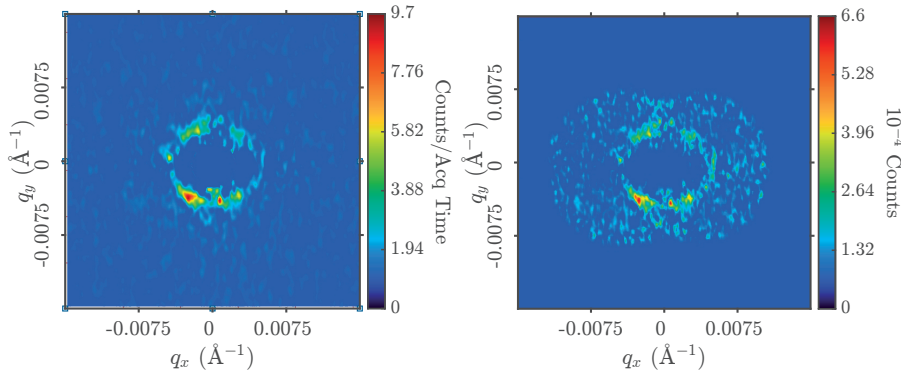


Figure 2.7: (Left) Sum of data taken over a range of ω angles in β -Bi₂Pd at 1.5 K and 0.1 T with the c -axis rotated 70° from the magnetic field. (Right) Result of Bayesian weighted sum of data in β -Bi₂Pd.

However, if the rocking curves are too wide and much broader than the measured range of angles and thus the spots are not well defined, as shown in Figure 2.7(Left), this will result in a whole range of angles with relevant information for the analysis, giving wrong weights to each frame and will end up in a failed Bayesian diffraction profile as shown in Figure 2.7(Right).

2.4.3. Calculation of the form factor by Bayesian method

Considering that the integrated intensity given by the Bayesian method should be identical to the one obtained from the rocking curve of the raw data, we proceed to calculate the form factor of CeCu_2Si_2 using both methods, as shown in Figure 2.8 (the form factor results of CeCu_2Si_2 will be explained in detail in Chapter 3).

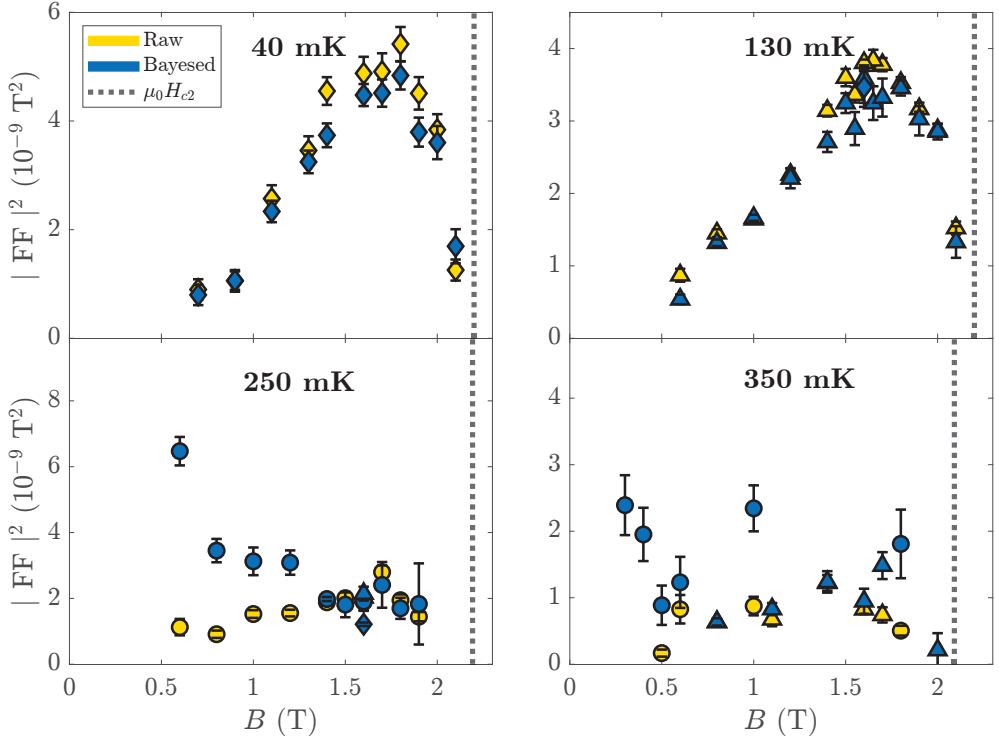


Figure 2.8: Comparison of calculated vortex lattice form factors in CeCu_2Si_2 at $T = 40, 130, 250$ and 350 mK using the classical method (Raw) and by Bayesian analysis (Bayesed). The symbol (Δ) corresponds to the data obtained at ILL in 2016, (\circ) corresponds to data obtained at ILL in 2018 and (\diamond) data were obtained at PSI in 2018. These experiments and their results will be further explained in Chapter 3.

We assume that the area under the rocking curve (Gaussian) is approximately given

by

$$A^{\text{rc}} = \frac{1}{2}h^{\text{rc}} \cdot \text{FWHM}^{\text{rc}}, \quad (2.34)$$

where A^{rc} is the approximate area under the rocking curve, h^{rc} is the height of the rocking curve and FWHM^{rc} is the full width at half maximum in radians. In the Bayesian case, we checked that the height of the given Gaussian had the same value as the height of the rocking curve, such that

$$A^{\text{q}} = \frac{1}{2}h^{\text{rc}} \cdot \text{FWHM}^{\text{q}}. \quad (2.35)$$

Therefore, to be able to compare both methods, it is necessary to perform the transformation

$$\frac{A^{\text{rc}}}{A^{\text{q}}} = \frac{\text{FWHM}^{\text{rc}}}{\text{FWHM}^{\text{q}}} = \frac{\text{FWHM}^{\text{rc}}}{|q| \tan(\text{FWHM}^{\text{rc}})} \approx \frac{\text{FWHM}^{\text{rc}}}{|q| \text{FWHM}^{\text{rc}}} = \frac{1}{|q|}. \quad (2.36)$$

As we can see in [Figure 2.8](#), the Bayesian method satisfactorily reproduces the form factor obtained at 40 mK and 130 mK inside the errorbars. However, the Bayesian program does not work correctly for the cases at 250 mK and 350 mK, where the signal was weaker, so we conclude that the Bayesian analysis can only be used when we have a well-defined VL, as previously indicated in [Section 2.4.2](#).

Study of Pauli-paramagnetic effects in heavy-fermion superconductors

3.1. PAULI-LIMITED SUPERCONDUCTIVITY

There exist several perturbations that can be involved in breaking up a Cooper pair. Typically there are two different ways to cause Cooper pair breaking and kill superconductivity, either orbital or spin-paramagnetic effects. The most common is the orbital case, where more flux lattice lines appear on increasing the field, so reducing the condensation energy. The orbital upper critical field can be obtained from the slope of the $H - T$ phase transition at T_c , given by $H_{c2}^{\text{orb}}(0) = -0.69|dH_{c2}/dT|_{T_c}T_c$ for the dirty limit and $H_{c2}^{\text{orb}}(0) = -0.73|dH_{c2}/dT|_{T_c}T_c$ for the clean limit [20].

When applying a magnetic field to certain superconductors, the Fermi surface splits into up- and down-spin electron bands due to the Zeeman effect. This Zeeman splitting of quasiparticles can be observed in type II superconductors when κ is very large, that is, the penetration depth is much greater compared with the value to the coherence length [21]. This Fermi surface or density of states separation causes so-called Pauli-paramagnetic pair breaking and contributes to the appearance of paramagnetic moments, which, in turn, affect the vortex state of superconductors and, eventually, act to reduce the upper

critical field as compared to the orbital value.

The new upper critical field H_P comes from the Zeeman energy that compensates the superconducting condensation energy, resulting in the Chandrasekhar-Clogston limit $H_P(0) = g^{-1/2}\Delta/\mu_B$ [22,23], where g is the Lande factor, μ_B is the Bohr magneton and Δ is the superconducting gap. When calculating H_{c2} in the BCS framework we end up with the Pauli-paramagnetically limited critical field, given by

$$H_P^{\text{BCS}}(0) = 1.84T_c. \quad (3.1)$$

However, for some materials, such as heavy-fermion superconductors, this limit does not hold, since both orbital and paramagnetic effects influence the upper critical field. To quantify the contribution of both effects we use the Maki parameter [24]:

$$\alpha = \sqrt{2} \frac{H_{c2}^{\text{orb}}(0)}{H_P(0)}. \quad (3.2)$$

When $\alpha > 1$, this suggests the presence of strong spin-paramagnetic effects at high fields [25].

Unconventional superconductors are good candidates to present Pauli-paramagnetic effects at high magnetic fields, especially close to the upper critical field, where there are minor orbital effects present [26].

3.2. HEAVY-FERMION SUPERCONDUCTORS

Contrary to what might be assumed, superconductivity can also arise from materials with magnetic degrees of freedom. Several heavy fermion materials have been shown to be superconducting both in the presence of different magnetic phases, or with magnetic phases adjacent to the superconductivity, such as, UPd_2Al_3 [27] or CeCoIn_5 [28].

Usually, heavy-fermion superconductors exhibit a specific heat with linear temperature dependence at low temperatures, $C \sim \gamma T$, a temperature-independent magnetic susceptibility, $\chi(0)$, and an electrical resistivity with an almost quadratic temperature dependence $\rho(T) = \rho_0 + AT^2$, indicating that they can be described as with Fermi liquids. However,

the Sommerfeld coefficient γ and $\chi(0)$ are between two or three orders of magnitude bigger than in normal metals and so the electronic states have far smaller energy scales than ordinary metals and effective masses, m^* , many times greater than the free electron mass, hence the name ‘heavy-fermion’. Altogether, this indicates that the quasiparticles involved are strongly interacting.

These characteristics may lead to a quantum-phase transition (QPT) at 0 K to nearby competing states. This transition is of second order (continuous) and happens at a quantum critical point (QCP). Usually, these phase transitions at absolute zero results from quantum fluctuations, driven by non-thermal controlling parameters, such as external pressure, magnetic field, chemical doping or a change in the electron density. In the vicinity of the critical pressure, critical magnetic field, critical stoichiometry, or electron concentration, the heavy fermion material will often show a clear deviation from the Fermi-liquid behaviour, commonly known as non-Fermi-liquid behaviour. In some of these compounds, a transition to the superconducting state also happens close to the QCP.

When a heavy fermion material becomes superconducting, if the heavier quasiparticles are involved, they will have a low Fermi velocity. It has been argued that this makes it difficult for these quasiparticles to escape their own polarization cloud and that Cooper pair formation mediated by the conventional phonon mechanism is unfeasible [29]. As previously mentioned, certain properties characteristic of non-Fermi liquids are sometimes observed, such as the resistivity deviation from the quadratic temperature dependence and a magnetic susceptibility much larger than in normal metals. Where this coexists with superconductivity, it can be indicative of unconventional superconductivity with an anisotropic order parameter in which the Fermi surface presents nodes where the superconducting gap goes to zero (see Section 1.5). Some properties, like the heat capacity, are defined by a power-law temperature dependence ($\propto T^n$) instead of the exponential dependence, $\exp(-\Delta/k_B T)$, typical of conventional isotropic *s*-wave superconductors.

The superconducting parameters are also affected by the heavy quasiparticles involved in the pairing mechanism, enlarging the penetration depth λ and simultaneously decreasing the characteristic coherence length ξ . The quasiparticle effective mass affects the critical fields, decreasing the lower critical field $H_{c1} \propto \lambda^{-2} \propto 1/m^*$ ($\sim 10^{-3}$ T) and increasing the upper critical field $H_{c2} \propto \xi^{-2} \propto m^{*2}$ ($\sim 1 - 10$ T). Heavy-fermion superconductors are

often strongly Pauli-limited, due to the presence of unpaired electrons in the vortex cores.

3.3. CERIUM-BASED HEAVY-FERMION SUPERCONDUCTORS: CeCu_2Si_2

The cerium-based heavy-fermion superconductors considered in this thesis are a series of tetragonal 122-compounds (see Figure 3.1) that usually show interaction between competing domains such as Landau Fermi liquids, non-Fermi liquid and unconventional superconductivity. In this kind of materials superconductivity often appears close to anti-ferromagnetic states.

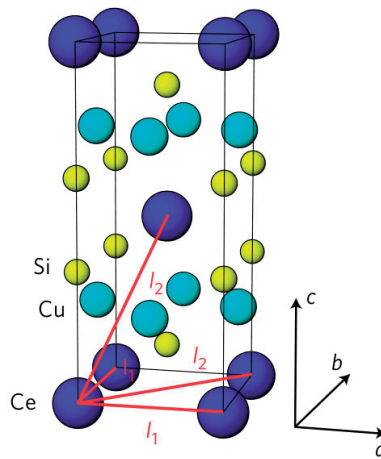


Figure 3.1: Tetragonal crystal structure of CeCu_2Si_2 (space group $I4/mmm$). Figure taken from [30].

They have attracted a lot of interest since the discovery of the first heavy-fermion superconductor, CeCu_2Si_2 , in 1979 [31]. The specific heat jump observed in Figure 3.2 was similar to the ones observed in other superconductors (this jump is proportional to the order parameter in BCS theory). In addition, below 1 K, the ac susceptibility is almost constant for all temperatures, while up to 1.5 K the resistivity has a linear dependence

with temperature and below 0.6 K it goes to zero. To confirm that these effects and the specific-heat jump indicated superconductivity, and not entry into an antiferromagnetic state, Steglich *et al.* repeated specific-heat, resistivity and ac susceptibility measurements, not only at 0 T, but also at 0.5 and 1 T [31]. They showed that the critical temperature was reduced for increasing field and there was no sign of a sudden drop of the critical field that could be related to an antiferromagnetic domain.

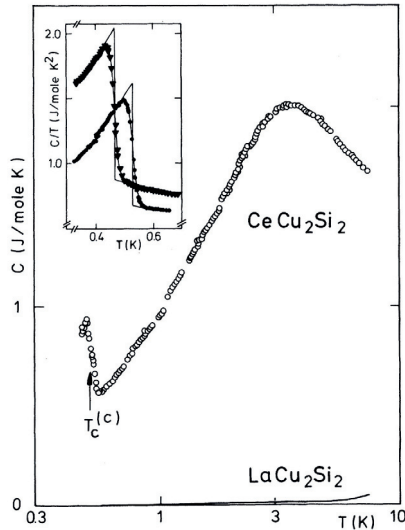


Figure 3.2: Molar specific heat of $CeCu_2Si_2$ at zero field from Ref. [31]. Arrow indicates the critical temperature first estimated. Two other specific-heat jumps at T_c from other two samples are shown in the inset.

The quantum criticality characteristic of heavy-fermion superconductors is also present in $CeCu_2Si_2$. The QCP of the system can be driven either with a change of the hydrostatic pressure or by the composition. When growing the sample, this could result in a superconducting (S-type) sample with a small excess of Cu or could result in an antiferromagnetic (A-type) sample when there is a slight deficit of Cu [30]. On the other hand, samples very close to 1:2:2 stoichiometry result in a ground state with competitive antiferromagnetic and superconducting domains (A/S-type) (Figure 3.3). Substituting Si by Ge generates a negative chemical pressure by which the coexistence between antiferromagnetic and the

superconducting domains can also be varied [32].

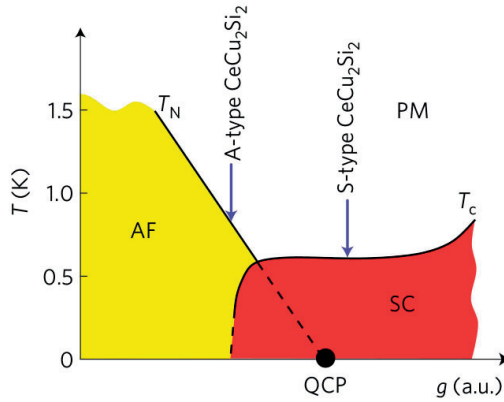


Figure 3.3: Schematic phase diagram as a function of temperature and coupling constant g (that can be hydrostatic pressure or composition) to tune the QCP of the system. Figure taken from [30].

The antiferromagnetic phase was found to be an incommensurate SDW associated with itinerant heavy fermion electrons in CeCu_2Si_2 and since then, this has been used to argue that antiferromagnetic excitations can be ascribed as the main driving force for the superconducting pairing. This was done in Ref. [30] by measuring the magnetic response of an S-type sample using inelastic neutron scattering techniques [30].

It can be observed in the left panel of **Figure 3.4** that a strong spin excitation gap at $\hbar\omega_{\text{gap}} \approx 0.2$ meV in the energy scans measured around the incommensurate propagation vector $\mathbf{Q}_{\text{AF}} = (0.215 \ 0.215 \ 1.458)$ in the superconducting state (at 0.07 K and 0 T). To make sure that this magnetic excitation is related to the superconducting state of the sample, different energy scans were done, one performed at an arbitrary \mathbf{Q} with the same modulus (left panel of **Figure 3.4**) and the other three energy scans measured at \mathbf{Q}_{AF} in the normal state of the sample (right panel of **Figure 3.4**). The absence of any spin excitation either above T_c or above B_{c2} , strongly indicates that the spin gap $\hbar\omega_{\text{gap}}$ is related to the superconducting state of CeCu_2Si_2 .

However, the microscopic nature of the pairing mechanism in CeCu_2Si_2 is still unclear. For many years, it was considered to be a d -wave superconductor from NMR studies [33]

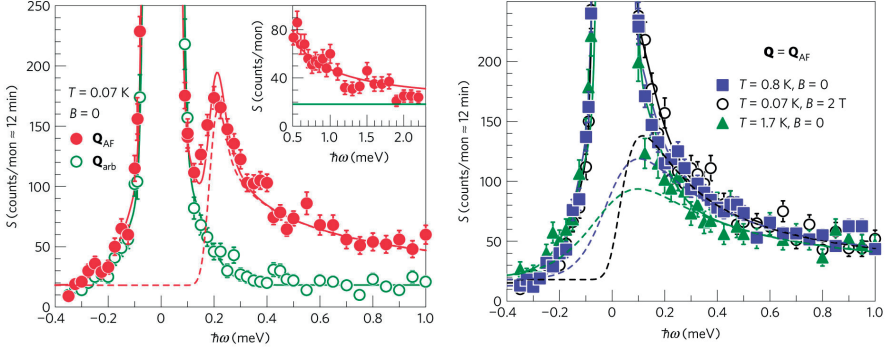


Figure 3.4: Energy transfer scans measured by inelastic neutron scattering at $\mathbf{Q} = \mathbf{Q}_{AF}$ in S-type $CeCu_2Si_2$ in the superconducting state (left) and the normal state (right). Figures taken from [30].

and because of the cubic dependence of the relaxation rate $1/T_1$ [34, 35]. However, this possibility was discarded when low temperature thermodynamic studies were performed on an S-type sample [36].

The specific heat (divided by T) was measured at various magnetic fields (shown in **Figure 3.5** (a)). Matching with the relaxation rate results previously found [34, 35], C_e/T exhibits a clear linear temperature dependence below T_c and shows a specific-heat jump of $\Delta C_e(T_c)/\gamma T_c \approx 1.2$, which is close to the value of 1.43 predicted by BCS theory. Nevertheless, below 0.1 K, the specific-heat deviates from its linear behaviour presenting a positive curvature. This could suggest a low quasiparticle density of states at low temperatures that cannot be reproduced by a nodal pairing mechanism. They provided a new point of view by using a multiband s -wave gap model to explain this odd behaviour of C_e/T . In **Figure 3.5** (b), they fitted the temperature variation of C_e/T using a two-BCS-gap model with $\Delta_1/k_B T_c = 1.76$ and $\Delta_2/k_B T_c = 0.7$ with 65% and 35% of the total density of states respectively.

When studying the specific-heat field dependence, C_e increases proportionally to H (**Figure 3.6**), instead of a square-root dependence, as is expected from nodal superconductors [37]. When focussing in the initial slope of $C_e(H)$, and following predictions from microscopic quasiclassical theory [38, 39], it can be expressed as $dC_e/dH|_{H \sim 0} =$

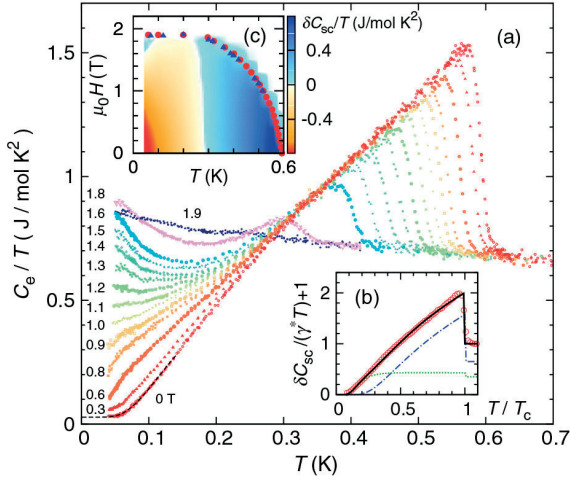


Figure 3.5: (a) Electronic specific heat of an S-type CeCu_2Si_2 single crystal divided by temperature, C_e/T , as a function of T measured in $H||[100]$. (b) Temperature variation of $\delta C_{\text{SC}}/\gamma^*T+1$ at $H=0$ and a fit using a two-gap BCS model. (c) $H-T$ phase diagram for $H||[100]$ obtained from specific-heat (circles) and magnetization (triangles) measurements. Figures taken from [36].

$[C_e(H_{c2}) - C_e(0)]/(\alpha H_{c2}^{\text{orb}})$, where H_{c2}^{orb} is the orbital upper critical field and α is a parameter that depends on the gap anisotropy and it is considered isotropic if $\alpha \sim 0.8$. From the initial slope α was found to be ~ 0.67 ; this can be related to an anisotropic gap structure or multi-band effects. The angular dependence of C_e was also measured by changing the ϕ angle between the magnetic field and the $[100]$ axis (inset in Figure 3.6) but no angular oscillation was seen, indicating an absence of line nodes. It was therefore concluded that CeCu_2Si_2 could be a candidate for a nodeless multiband superconductor.

In addition to the two-band model proposed in Ref. [36], odd behaviour was also seen at high fields, $H||[001]$, below 150 mK [40]. This change in the heat-capacity slope observed in Figure 3.5 and Figure 3.6 disappears on reaching H_{c2} , suggesting that this effect is related to superconductivity and may originate from the strong paramagnetic effects present in the sample, although there is no *direct* evidence of Pauli paramagnetic effects.

Other later studies have built on this work to explore the pairing mechanism. Heat

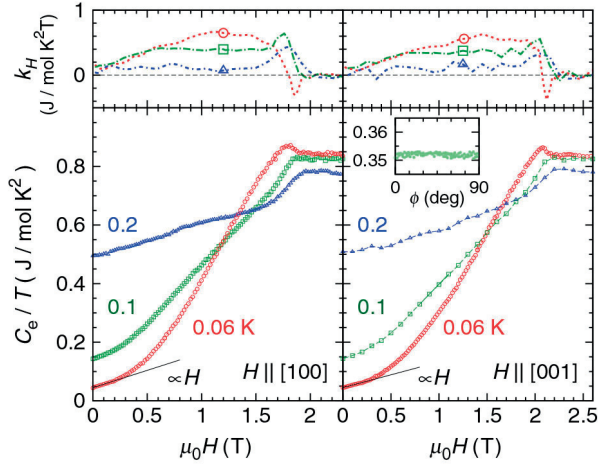


Figure 3.6: Field dependence of C_e/T and its slope, k_H , measured at 0.06 (circles), 0.1 (squares) and 0.2 K (triangles) with $H \parallel [100]$ and $H \parallel [001]$.

capacity studies by Yamashita *et al.* [41], combined with looking at the effect of impurities on the critical temperature, rule out any possibility of a nodal or sign-changing superconducting gap, and conclude that the only possible explanation is a fully gapped non-sign-changing s-wave state with possible multigaps. Their new data on new $C(T)$, $\lambda(T)$ and $\kappa(H)$ are in accordance with previous work [36,40]. However, other studies [42] point to a $d + d$ band-mixing pairing state, which agrees with fully gapped superconductivity and could explain either the behaviour of the superfluid density and heat-capacity measurements.

In the next sections we will focus not only on the study of the pairing mechanism in CeCu_2Si_2 using SANS, but also on the Pauli paramagnetic effect present in S-type CeCu_2Si_2 and its effect in the vortex lattice.

3.4. PAULI PARAMAGNETISM AND THE VORTEX LATTICE IN SUPER-CONDUCTING CeCu_2Si_2

SANS measurements of the vortex lattice (VL) allow information such as the penetration depth, coherence length, and the superconducting gap structure of a superconductor to be extracted. Since there were no previous studies on the vortex lattice of CeCu_2Si_2 using neutron scattering, we performed a SANS experiment at PSI in 2015 where the vortex lattice signal was first observed. Since then, we have carried out several experiments on this material at the D33 instrument of the Institut Laue-Langevin (ILL), and the SANS-I instrument at the Swiss spallation neutron source SINQ, Paul Scherrer Institute (PSI).

We used a S-type sample, the same one used in Ref. [30], with a volume $6 \times 6 \times 8 \text{ mm}^3$ and a total mass of 2.014 g. It has a critical temperature of $T_c \approx 0.6 \text{ K}$ and an upper critical field $B_{c2}(0) \approx 2.2 \text{ T}$ [30]. Its low resistivity indicates a high-quality sample with electron mean free path longer than the superconducting coherence length (see Paper III).

We performed two experiments at ILL in 2016 and 2018, which from now on we will refer to as ILL2016 and ILL2018. In experiment ILL2016 [43] the sample was mounted on an aluminium sample holder connected to the dilution refrigerator of a 17 T horizontal cryomagnet [16] (base temperature $\sim 130 \text{ mK}$), with the field applied parallel to the \mathbf{c} -axis of the sample. In experiment ILL2018 [44], the sample was mounted on a copper pin in a horizontal-field 8 T cryomagnet, with base temperature 70 mK. During this last experiment an antiferromagnetic and superconducting (A/S-type) CeCu_2Si_2 sample was also measured, but no vortex lattice signal was seen, possibly due to pinning effects.

For the experiments at PSI, labelled PSI2017 and PSI2018, the sample was mounted in both cases into a horizontal-field 11 T cryomagnet, with a base temperature of 40 mK. During the PSI2018 experiment, the \mathbf{c} -axis of the sample was misaligned from the magnetic field but this does not affect the measured intensity of the vortex lattice.

In Figure 3.7(Left), we show the field dependence of the form factor of the first order reflections from the VL at $T = 40, 130, 250$ and 350 mK . For these measurements, $B \parallel c$

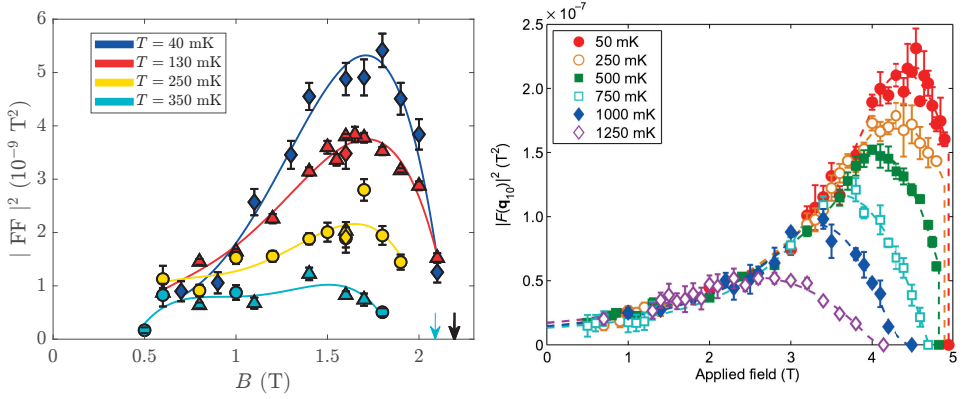


Figure 3.7: (Left) Field dependence of the squared form factor of CeCu_2Si_2 calculated from the first order diffraction spots with a well-defined rocking curve, for temperatures between 40 mK and 350 mK. The symbol (Δ) corresponds to the data obtained at ILL in 2016, (\circ) corresponds to data obtained at ILL in 2018 and (\diamond) data were obtained at PSI in 2018. \diamond data were measured with the sample rotated away from the $\mathbf{B} \parallel \mathbf{c}$ orientation but the integrated intensity is not affected from this change, as we can observe from the points at 1.6 T, 250 mK and 130 mK, that match with measurements from other experiments. The cyan arrow correspond to the value of $B_{c2}(T)$ for $T = 350$ mK and the black arrow covers all the upper critical fields for $T = 40, 130$ and 250 mK obtained from Ref. [45]. Solid lines are guides for the eye and the crossing of the lines is not real. Picture taken from Paper III [18]. (Right) Field dependence of the square of the FLL form factor for first-order Bragg reflections from CeCoIn_5 , for temperatures up to 1250 mK, provided for comparison. The dashed lines are guides to the eye. The points at which the FF goes to zero are obtained from measurements of H_{c2} . Picture taken from Ref. [46].

except at 40 mK, where there is an offset of 28 degrees of the c -axis with respect to the direction of the field. As shown in Figure 3.7(Left) this does not appear to affect the observed intensities. The form of the field-dependence changes with temperature, with Pauli paramagnetic effects visible over almost the entire field range.

In general, the form factor rises up to a maximum, and then begins to fall to zero on approaching B_{c2} , indicating strong PPE. For 40 mK and 130 mK the intensity falls steeply

on reaching ~ 2.1 T, showing a rapid variation on approaching the normal state. At 250 mK the form factor increases slightly with field, showing that PPE remain important but we do not observe a sudden decrease near B_{c2} . Meanwhile, at 350 mK the form factor is more constant as a function of field, but falling towards zero at low and high fields.

This kind of behaviour is also observed in CeCoIn₅ [46] (see Figure 3.7(Right)). However in this material, a first order transition into the normal state at B_{c2} is clearly observed at low temperatures, both in heat capacity and SANS. This is in contrast to the second order transition observed in CeCu₂Si₂, again both in heat capacity [36] and in our SANS data.

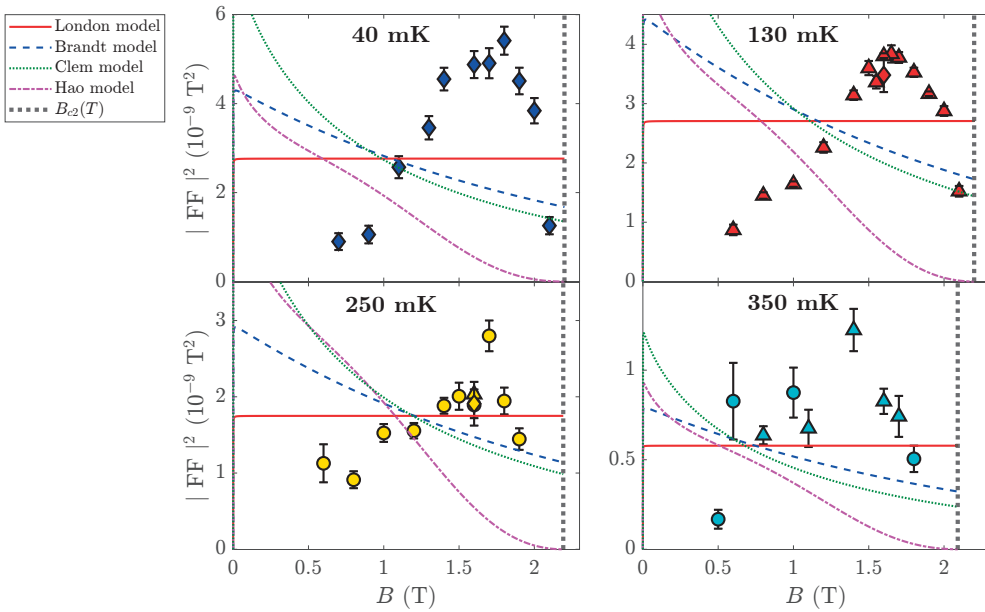


Figure 3.8: Comparison of measured and calculated vortex lattice form factors in S-type CeCu₂Si₂ at $T = 40, 130, 250$ and 350 mK using standard models [7, 18].

In both materials, the field-dependence cannot be described by the various standard models for the form factor associated with vortex lattices. For the case of CeCu₂Si₂, in Figure 3.8 we show the results of fitting these various models (see Eq. (2.12), Eq. (2.13), Eq. (2.14) and Eq. (2.15)) to the field dependent results at 40, 130, 250 and 350 mK. When the London penetration depth is instead used as a fitting parameter, it is evident that

none of the models agree with the data and all of them give unphysically low values for λ .

From the premise that standard solutions of London or GL equations are incapable of reproducing completely the behaviour of Pauli-limited superconductors, we decided to develop an analytical expression which will be able to reproduce the temperature and field dependence of the form factor with strong Pauli paramagnetic effects.

3.5. MODELLING OF VL BEHAVIOUR IN PAULI-LIMITED SUPERCONDUCTORS

In [Paper IV](#), to obtain a simple physically-based algebraic expression for the form factor in Pauli-limited superconductors, we looked for the main effects that Pauli paramagnetism has on the vortex lattice of CeCoIn₅ based on the results of first-principles computation by Machida and Ichioka [47].

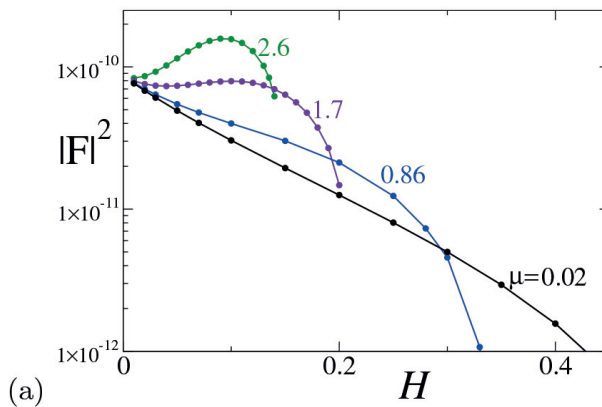


Figure 3.9: Calculated field dependence of CeCoIn₅ FLL form factor for $\mu = 0.02, 0.86, 1.7$, and 2.6 at $T = 0.1T_c$ in d -wave pairing. Picture taken from from Ref. [47].

In [Figure 3.9](#), the form factor is plotted against field for different μ values, which represent the strength of paramagnetic effects. For all μ values, all curves start at the

same London value, and after reaching a maximum, the form factor drops to zero towards B_{c2} . The case with very small Pauli paramagnetic contribution just falls exponentially with field, as expected from the analytical London model with the Brandt exponential cut-off. Therefore, in the Pauli-limited regime, we still expect contributions from

$$F(B) = \exp(-cq^2\xi^2)F_{\text{orb}}(B) \quad (3.3)$$

where F_{orb} is the London-Brandt analytical expression for the form factor given in Eq. (2.12), ξ is the orbital coherence length, q^2 is proportional to B by flux quantization and the constant c is a parameter expected to have a value between 0.25 and 0.5. A value for c of 0.44 was found in $\text{YBa}_2\text{Cu}_3\text{O}_7$ [48, 49] (see Appendix in Paper V), and we have used a value close to this.

The calculations for CeCoIn_5 assumed d -wave superconductivity. Ichioka provided us with additional unpublished microscopic-Eilenberg-theory calculations [50] performed for an isotropic s -wave superconductor with cylindrical isotropic Fermi surface, $T/T_c = 1$ and $\kappa = 100$, at different μ values to guide our model development. From this, we identified a quadratic behaviour of the core radius for fields below $0.2B_{c2}$ (see Figure 3.10 (Left)). Furthermore, we also estimated the strength of the magnetic moment in the centre of the core, by plotting the ratio between the magnetization of the core and the magnetization at B_{c2} in Figure 3.10 (Right). As we can see, the magnetization rapidly rises proportional to field, but with a value at least 10 times higher than the magnetization expected from normal electrons. This development of the magnetization clearly is a different effect from the increase of the magnetization expected from conventional superconductivity.

We arrived to the conclusion that Pauli-limiting leads to two main effects: (i) additional spin magnetization developing in the cores, even present at low fields, and (ii) the core radius growing with quadratic dependence with increasing field.

To better understand Pauli paramagnetic effects and compare them to the orbital behaviour, we simulated the vortex lattice arrangement and the magnetization of the vortex lines for CeCu_2Si_2 in Figure 3.11. As we can observe from the first row, in which we only take into account the London contribution, the vortices tend to overlap with each other due to the finite size of the core, and the form factor to suppress at large q or increasing field. Hence, from the second row in Figure 3.11, which corresponds to the

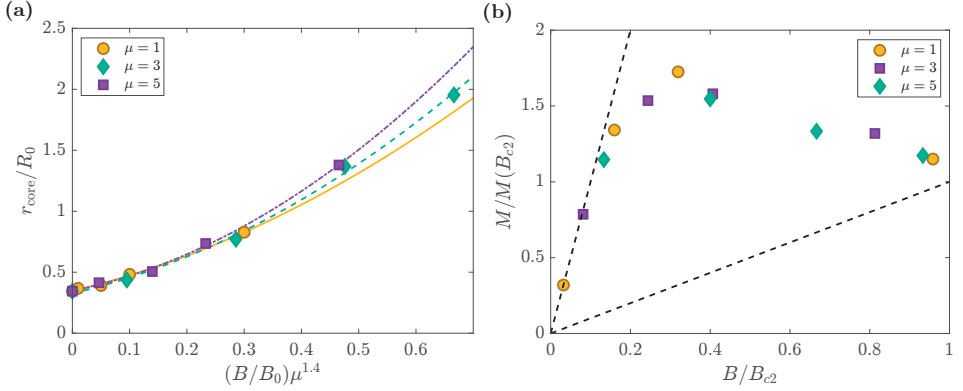


Figure 3.10: (a) Field dependence of the core radius for different values of μ . The core radius has been scaled to $R_0 = \hbar v_{F0}/2\pi k_B T_c$ [47, 50]. The magnetic field has been scaled to $B_0 = \hbar c/2|e|R_0^2$ [47, 50] and has also been multiplied by $\mu^{1.4}$ to be able to include r_{core} for different values of μ on the same scale. The quadratic fits to the $\mu = 1$ (yellow solid line), $\mu = 3$ (blue dashed line) and $\mu = 5$ (dotted and dashed purple line) values are included. (b) Field dependence of the magnetization in the centre of the core for different paramagnetic strengths, μ , normalized to the magnetization at B_{c2} .

London contribution only, the magnetization contrast between the inside and the outside of the cores will tend to flatten once approaching B_{c2} . This overlapping of the vortex lines will apply both for the orbital contribution and the paramagnetic contribution. However, when including the paramagnetic contribution, we expect the magnetization of the cores to be massively affected by the increasing field, resulting in a non-negligible magnetization contrast at fields close to the upper critical field.

Then, the Pauli paramagnetic contribution, F_{PM} , and also the small contribution from orbital currents F_{orb} will be affected by the size core cut-off depending on a now field-dependent coherence length, ξ_{PM} and the value of q :

$$F(B) = \exp(-cq^2\xi_{\text{PM}}^2)(F_{\text{orb}}(B) + F_{\text{PM}}(B)). \quad (3.4)$$

To describe the enhancement of the vortex cores, we introduced a new characteristic length labelled as the paramagnetic coherence length ξ_{PM} , given by a quadratic field-dependence

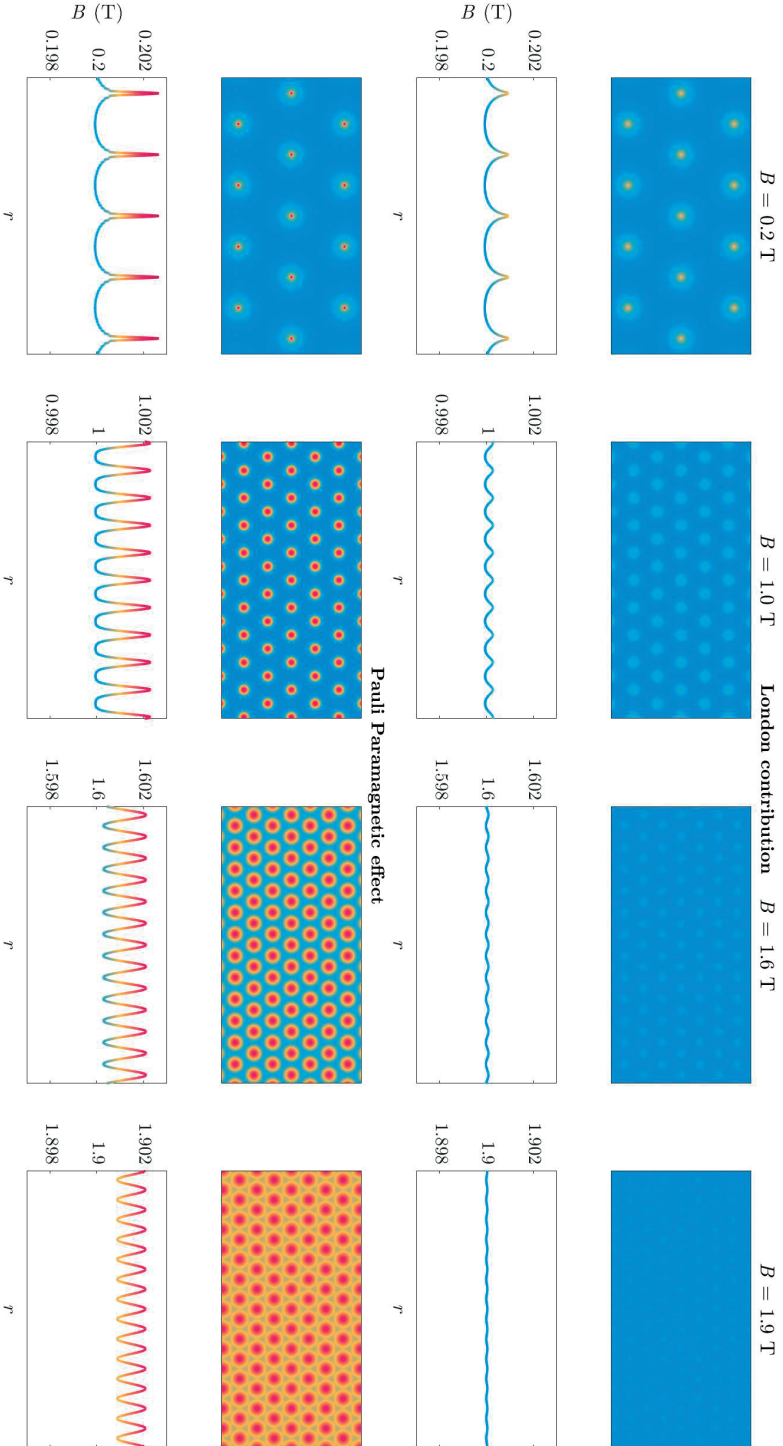


Figure 3.11: Simulation of the arrangement of the CeCu_2Si_2 vortex lattice at 40 mK with increasing field just taking into account the London contribution (top half) and including Pauli paramagnetic contributions (bottom half). For each field condition there is a 1D plot of B as a function of position, with a 2D colour plot above using the same position scale. The colours in the 1D and 2D plots are on the same scale.

of ξ_{PM} at low fields [50]:

$$\xi_{\text{PM}}^2(B, T) = \xi_{\text{orb}}^2(T) + \epsilon \left(\frac{\Phi_0}{2\pi B_{c2}(T)} \right) \left(\frac{B}{B_{c2}(T)} \right)^2, \quad (3.5)$$

where ξ_{orb} is the radius core in the absence of PPE and $B_{c2}(T)$ is the experimental upper critical field at temperature T . The $B_{c2}(T)$ factors have been included so that the fitting parameter ϵ will be ~ 1 and fairly temperature-independent if ξ_{PM} is comparable with the vortex spacing at $B = B_{c2}(T)$. ϵ can be interpreted as a correction of the size of the core when PPE are present.

For the value and temperature-dependence of the core size ξ_{orb} , we have to consider several effects. We expect that (i) the orbital core size will increase with temperature and also will make the paramagnetic form factor to increase, because of the increased volume of magnetised cores; (ii) the magnetization contrast between the inside and the outside of the cores it is also expected to fall for growing T and (iii) at high fields, that is large q^2 , will make ξ_{orb} to expand and hence ξ_{PM} , making the form factor fall as T increases, because of the Brandt cut-off.

As Kramer and Pesch pointed out [51], in clean type-II materials the core contracts strongly at low temperatures

$$\xi_{\text{orb}}(T) \sim \xi_{\text{BCS}}(T) \times T/T_c \quad (3.6)$$

where $\xi_{\text{BCS}}(T) = \hbar v_F / \pi \Delta(T)$ is the characteristic length developed in Bardeen-Cooper-Schrieffer theory. This is because $\Delta(r)$ is self-consistently determined by the wavefunctions in the core of the occupied unpaired states, and these are restricted to smaller r as the temperature is lowered.

In very clean materials the temperature dependence of the coherence length disappears when $\xi_{\text{orb}} \propto k_F^{-1}$. However, if the material is not perfectly clean, the core shrinkage stops below a temperature given by $T/T_c < \xi_{\text{BCS}}/\ell$ and the orbital coherence length becomes $\xi_{\text{orb}} \approx \xi_{\text{BCS}}^2/\ell$.

Taking the definition of the coherence length at zero temperature $\xi_{\text{BCS}}(T = 0) = \Phi_0 / 2\pi B_{c2}^{\text{orb}}(T = 0)$ and assuming $\xi_{\text{orb}}(T) \propto 1/\Delta(T)$, the temperature dependence of the orbital-limiting field will be given by

$$B_{c2}^{\text{orb}}(T) = B_{c2}^{\text{orb}}(0) \sum_i w_i \left(\frac{\Delta_i(T)}{\Delta_i(0)} \right)^2 \quad (3.7)$$

where $\Delta_i(T)$ are the different superconducting gaps present with their respective weights, w_i . We also have tried the standard WHH T -dependence [52], which gives the orbital-limiting field at lower temperatures in terms of its slope close to T_c , however it fails to reproduce the temperature dependence at higher fields, where the Pauli paramagnetic effects are stronger and it does not take into account possible multigap effects.

At $T = 0$ and at low fields, as shown in the bottom row of Figure 3.11, we expect zero spin susceptibility outside the flux lines so there will be a maximum magnetization contrast between the inside and the outside vortex cores. Hence we arrived to the conclusion that the paramagnetic contribution of the form factor will be proportional to the core magnetization. As we have seen in Figure 3.10, M inside the cores rises rapidly, proportional to magnetic field up to $\sim 0.1B_{c2}$ [50], with a field dependence $\mu_0 M \sim \chi_n \mu_0 H_{c2} \sim \chi_n B_{c2}$ and with χ_n as the Pauli susceptibility in the normal state at zero temperature. As we know from BCS theory, the quasiparticles are thermally excited above Δ with increasing temperature consequently rising $\mu_0 M$ outside the cores and decreasing the contrast, while χ_n will stay constant for all T . Assuming that Δ between the cores is not strongly suppressed by field, the spin susceptibility in this region is given by [53]

$$\frac{\chi_s(T)}{\chi_n} = \sum_i 2w_i \int_0^\infty dy \frac{\exp[(y^2 + \beta^2 \Delta_i^2(T))^{\frac{1}{2}}]}{\left\{ \exp[(y^2 + \beta^2 \Delta_i^2(T))^{\frac{1}{2}}] + 1 \right\}^2} \quad (3.8)$$

where $\beta = 1/k_B T$ and w_i is the weight of a band (if multi-band) having energy gap $\Delta_i(T)$. Hence the magnetization contrast $\mu_0 \delta M$ in the VL becomes $\sim [\chi_n - \chi_s(T)] B_{c2}$. When calculating the normalized superfluid density [54] we found that this gives the same temperature dependence as the integral in Eq. (3.8). Therefore, the magnetization contrast can be expressed in terms of the superfluid fraction $\rho_s(T)/\rho$ to give $\mu_0 \delta M \sim \chi_n B_{c2} \times \rho_s(T)/\rho$.

To calculate $\rho_s(T)$, we need the temperature and angular-dependence of the superconducting gap function, which is taken as [54]. First, for spin-singlet pairing states, the gap function is expressed as

$$\Delta_i(T, \mathbf{k}) = \Delta_i(T) g(\mathbf{k}) \quad (3.9)$$

where $g(\mathbf{k})$ expresses the angular dependence of the superconducting gap. For isotropic s -wave pairing it will take the value of $g = 1$, however for d -wave pairing it will be expressed

as $g = \cos(2\phi)$. For the case of the superfluid density in a cylindrical Fermi surface it will be calculated as

$$\frac{\rho_s(T)}{\rho} = 1 - \frac{1}{2\pi} \int_0^{2\pi} d\phi \cos^2(\phi) \frac{\chi_s(T)}{\chi_n}. \quad (3.10)$$

For the T -dependence of the gap function we have used the one proposed by Gross [55]

$$\Delta_i(T) = \Delta_i(0) \tanh \left(\frac{\pi k_B T_c}{\Delta_i(0)} \sqrt{a \left(\frac{T_c}{T} - 1 \right)} \right), \quad (3.11)$$

where $\Delta_i(0)$ is the value of the gap at zero temperature and depending on the pairing state of the superconductor, $\Delta(0) = 1.76 k_B T_c$ and $a = 1$ in the case of BCS isotropic s -wave and $\Delta(0) = 2.14 k_B T_c$ and $a = 4/3$ for a two-dimensional d -wave superconductor.

The Pauli paramagnetic contribution to the form factor depends on the magnetization contrast, the area of a flux line given by the new paramagnetic coherence length and the number of flux lines per unit area

$$F_{\text{PM}}(B, T) = \eta \left(\frac{2\pi B}{\Phi_0} \right) \left[\left(\frac{\rho_s(T)}{\rho} \right) \chi_n B_{c2}(T) \right] \xi_{\text{PM}}^2(B, T) \quad (3.12)$$

where the constant η is a fitting parameter expected to not be larger than 1, included to correct any approximations made for the magnetization in the core.

Finally, the orbital contribution to the form factor, F_{orb} , has a temperature which may be derived from the relation between the normalized superfluid density and the temperature dependence of the penetration depth, $\rho_s(T)/\rho = (\lambda(0)/\lambda(T))^2$. The orbital F_{orb} and the paramagnetic (Eq. (3.12)) contributions can then be substituted into Eq. (3.4) to give an algebraic model to fit our data as a function of field and temperature.

As shown in Paper III, we fitted the field (Figure 3.12(a)) and temperature (Figure 3.12(b)) dependence of the form factor of CeCu₂Si₂, measured at different fixed temperatures and fields, respectively. We have used single s -wave, two-band s -wave and single d -wave models. However, the last was completely ruled out because it failed to reproduce the low-temperature behaviour.

Fig. 3.12(a) shows the fits versus field at various fixed temperatures, using a single s -wave and a two-band s -wave model, with the latter using the gap values and weights proposed in previous specific heat measurements [36]. In Table I are given the fitting parameters and the root-mean-square deviation between the curves and the data. Both models capture the behaviour up to the peak quite well, but are unable to reproduce the

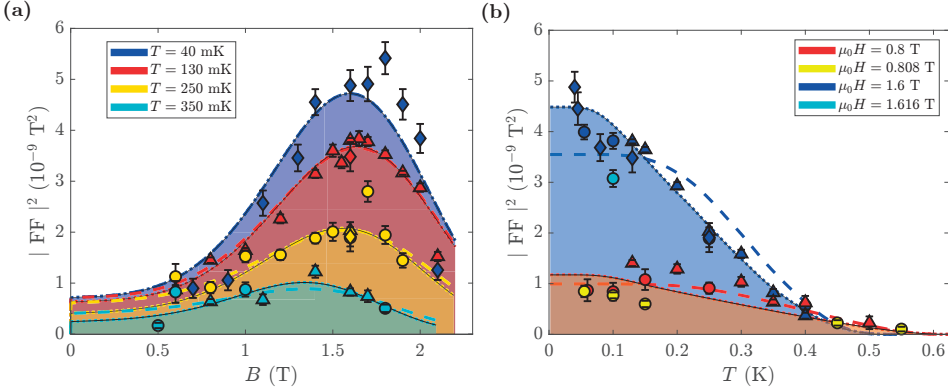


Figure 3.12: (a) Field and (b) temperature dependence of the squared form factor with the results of the fits using our model for paramagnetic effects, with a single s -wave gap (dashed line) and two-gap s -wave model (dotted line). For all fits $\lambda(0) = 13000 \text{ \AA}$.

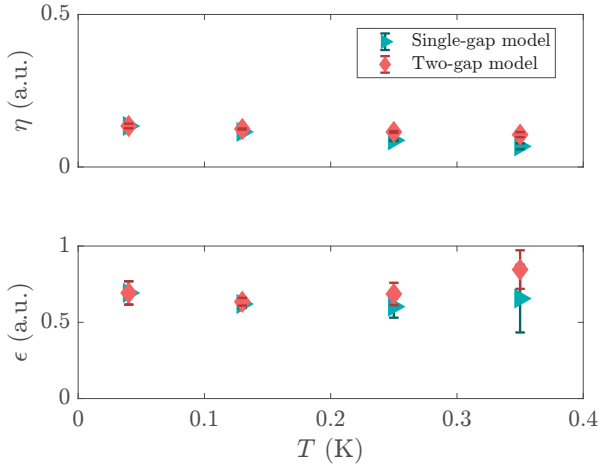


Figure 3.13: Temperature dependence of the fitting parameters η (top) and ϵ (bottom) using our model for paramagnetic effects, with a single s -wave gap and two-gap s -wave model for CeCu_2Si_2 .

sharp drop on the approach to B_{c2} at low temperatures. This could be due to a suppression of Δ between the cores at high fields and low temperatures, or it could be an effect of the FFLO state proposed by Kitagawa *et al.* [45], as the FFLO state is expected to suppress

<i>s</i> -wave: field scans at constant temperature			
<i>T</i> (mK)	η	ϵ	RMSD (10^{-10})
40	0.134(8)	0.69(8)	6.88
130	0.115(2)	0.62(3)	2.49
250	0.088(2)	0.60(7)	2.78
350	0.07(1)	0.7(2)	1.98

<i>(s + s)</i> -wave: field scans at constant temperature			
<i>T</i> (mK)	η	ϵ	RMSD (10^{-10})
40	0.134(8)	0.69(8)	6.88
130	0.125(2)	0.63(3)	2.39
250	0.115(3)	0.69(7)	3.07
350	0.106(8)	0.8(1)	1.86

<i>s</i> -wave: temperature scans at constant field			
<i>B</i> (T)	η	ϵ	RMSD (10^{-10})
0.8	0.07(1)	0.64	2.09
1.6	0.113(2)	0.64	5.58

<i>(s + s)</i> -wave: temperature scans at constant field			
<i>B</i> (T)	η	ϵ	RMSD (10^{-10})
0.8	0.09(1)	0.71	2.89
1.6	0.130(1)	0.71	3.66

Table 3.1: Parameters resulting from the fits and the root-mean-square deviations for field scans in Figure 3.12(a) and temperature scans in Figure 3.12(b) for CeCu₂Si₂. In all cases, we fixed $c = 0.42$.

the form factor [56, 57]. The fitting parameters ϵ and η give sufficient flexibility that the two models fit equally well (Figure 3.13).

In Fig. 3.12(b) we plot the temperature dependence of the form factor of the first order reflections from the VL at $B = 0.8$ T (combined with points at 0.808 T) and

1.6 T (combined with points at 1.616 T). Figure 3.12(b) also shows the fits using the s -wave model at 0.8 T and 1.6 T, and the $s + s$ -wave model again using the values of the gaps and weights proposed by Kittaka *et al.* [36]. The values of the fit parameters are in Table I, including the root-mean-square deviation for each fit. A two-gap model is required to fit heat capacity data in this material [36,40]. For our SANS data, we find that the two-gap model gives parameters that are less temperature-dependent and have better correspondence between field and temperature scans. The rise in the 1.6 T form factor at low temperatures seen in Figure 3.12(b) cannot be reproduced by a single-gap model, so we prefer the two-gap model, although our fits do not enforce it.

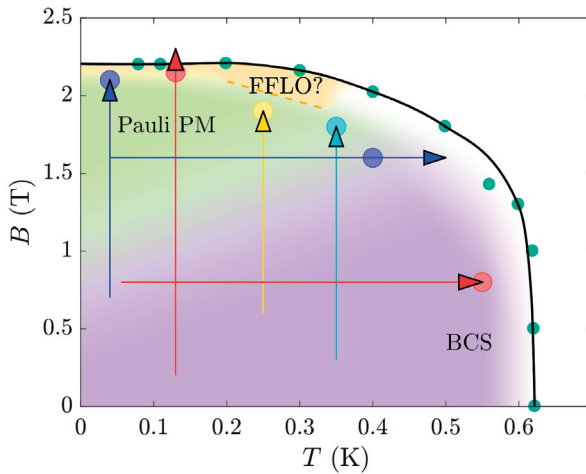


Figure 3.14: B - T phase diagram for superconductivity in CeCu_2Si_2 with $\mathbf{B} \parallel \mathbf{c}$. The different colours highlight the BCS region and where the Pauli paramagnetism is dominant at low temperatures and high fields and the FFLO region appearing close to the upper critical field at low temperatures. The dashed line indicates the limit of the FFLO region proposed by NMR studies [45]. Arrows show the field- and temperature-scans covered by the SANS experiments. Shaded points show the highest field or temperature at which the vortex lattice was visible in each scan. The black line represents the upper critical field B_{c2} as a function of temperature for $\mathbf{B} \parallel \mathbf{c}$ with the green solid points representing experimental data obtained by ac susceptibility [45]. Figure taken from [Paper III](#).

Our measurements of the field-dependence of the form factor represent the second observation of Pauli paramagnetic effects in a heavy-fermion material, after the observations made in CeCoIn_5 [46,58]. Unlike CeCoIn_5 , CeCu_2Si_2 does not show a first-order transition to the normal state at high fields. Both materials have some evidence supporting the existence of a field-induced quantum critical point [59]. We note that rather weaker effects due to the paramagnetism of *localised* f -electrons have also been observed in $\text{TmNi}_2\text{B}_2\text{C}$ [60].

Near B_{c2} at low temperatures the observed intensity drops faster than expected. One possible explanation for this could be that the material enters the postulated FFLO phase, which would suppress the form factor (see Figure 3(b) in Ref. [56] and Figure 5 in Ref. [57]). This observation also matches with previous NMR studies [45] in which an enhancement of $1/T_1T$, observed just below the upper critical field is taken as evidence for the FFLO state (see Fig. 3.14). We see in Fig. 3.12(a) that the maximum peak intensity is shifted towards the upper critical field for decreasing temperature, suggesting a major contribution of PPE close to B_{c2} , before entering the FFLO state which then decreases the intensity abruptly.

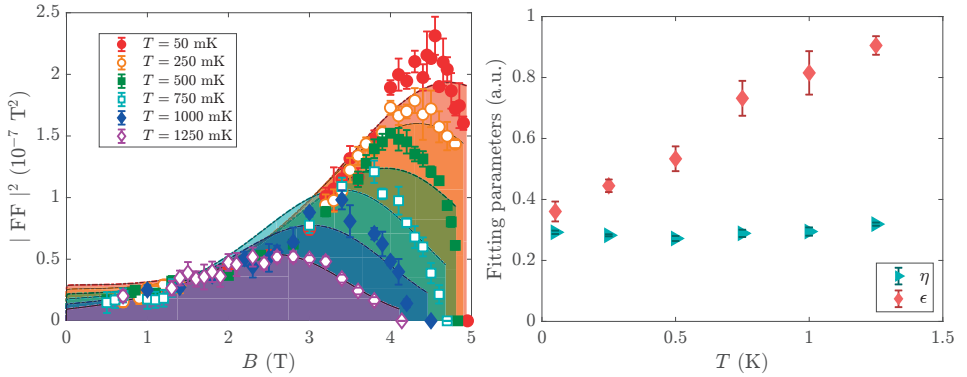


Figure 3.15: (Left) Field dependence of the squared form factor with the results of the fits using our model for paramagnetic effects, with a single d -wave gap. For all fits $\lambda(0) = 5500 \text{ \AA}$ [61] Data provided by J.S.White from Ref. [46]. (Right) Temperature dependence of the fitting parameters η and ϵ using our model for paramagnetic effects, with a d -wave gap model for CeCoIn_5 .

Once we have a fair understanding of our model, we then applied it to other strongly Pauli-limited superconductors in [Paper IV](#). CeCoIn_5 has a similar increase of the form

<i>d</i> -wave: field scans at constant temperature			
T (mK)	η	ϵ	RMSD (10^{-8})
50	0.292(6)	0.36(3)	4.09
250	0.282(3)	0.44(2)	1.07
500	0.272(8)	0.53(4)	2.43
750	0.29(1)	0.73(6)	1.63
1000	0.29(1)	0.82(7)	1.39
1250	0.319(5)	0.91(3)	0.41

Table 3.2: Parameters resulting from the fits and the root-mean-square deviations for field scans in [Figure 3.15](#) (Left) for CeCoIn₅. In all cases, we fixed $c = 0.42$.

factor at high fields and low temperatures [46], and it has been theorized that the superconductivity mechanism is also driven by localized f -electrons. As we did with CeCu₂Si₂, we chose a fixed value for $c = 0.42$, but this time used a d -wave gap and the WHH approximation for the temperature dependence of B_{c2} . As in the case of CeCu₂Si₂, the model does a reasonably good job reproducing the field-dependence of the form factor and finding the peaks at all temperatures, as shown in [Figure 3.15](#) (Left). However, as mentioned before, it is unable to replicate the sudden fall close to the upper critical field. On [Table 3.2](#) we can observe that η stays fairly constant for all the range of temperatures but ϵ is linear-dependent of temperature, suggesting a possible extra temperature contribution to the broadening of the cores ([Figure 3.15](#) (Right)).

3.6. SUMMARY

In this chapter we have summarised how Pauli paramagnetic effects are one of the mechanisms which kill superconductivity and how it can affect the vortex lattice, and then more explicitly our measurements of the vortex lattice using SANS.

We show the SANS measurements performed on the vortex lattice in CeCu_2Si_2 . We reported the field and temperature dependence of the VL form factor of this material and concluded that it shows Pauli paramagnetic effects when approaching to the upper critical field, as was previously observed in CeCoIn_5 .

Since standard models are unable to reproduce the behaviour of the form factor of CeCu_2Si_2 and other Pauli-limited superconductors with field or temperature, we then developed a new expression that includes the Pauli paramagnetic effects on the vortex cores. However, for this new model, it is necessary to use a greater penetration depth, $\lambda(0) = 13000 \text{ \AA}$, than the one reported in previous bibliography. For most field dependencies at temperatures between 40 mK and 350 mK, our results are consistent with both s -wave and two-band $s + s$ -wave superconductivity, although the fits are a little better for the $s + s$ wave mode, where the fitting parameters are also more temperature independent. Our results definitely support the s -wave models, with no d -wave models contribution.

To check that our new model could work for other Pauli-limited superconductors, we also fitted the field dependence of the form factor of CeCoIn_5 for temperatures from 50 to 1250 mK. The Pauli paramagnetic model satisfactorily reproduces the field dependence on CeCoIn_5 assuming d -wave pairing. However, for this case, ϵ is strongly temperature dependent, suggesting that the core size has an additional contribution in this material that is linear in T .

We aim to use this model not only for other Ce-based superconductors but also for strong Pauli-limited superconductors, as the case for $\text{TmNi}_2\text{B}_2\text{C}$, and apply it to other FF temperature dependencies, for example, in CeCoIn_5 .

CHAPTER 4

High-magnetic field studies on the high-temperature superconductor YBCO

The first high- T_c cuprate discovered was $\text{La}_{1.85}\text{Ba}_{0.15}\text{CuO}_4$ (LBCO) by Bednorz and Müller in 1986 [62]. Shortly after, in 1987, superconductivity was observed in a Y-Ba-Cu-O system [63].

$\text{YBa}_2\text{Cu}_3\text{O}_{7-\delta}$ (commonly known as YBCO) is one of the most famous high-temperature, or cuprate, superconductors. This high- κ superconductor has an orthorhombic crystal structure which, like all cuprate superconductors, contains two-dimensional CuO_2 *ab*-plane layers that are the source of the *d*-wave superconductivity that dominates in these materials. However, one consequence of the crystal orthorhombicity is that this *d*-wave order parameter must contain a finite additional *s*-wave component, evidenced by phase-sensitive [64], tunneling [65], and μSR [66] studies. In $\text{YBa}_2\text{Cu}_3\text{O}_{7-\delta}$ there are also one-dimensional CuO chains which exhibit long-range order along the **b**-axis; by changing δ , vacancies are introduced into these CuO chains and this controls the level of hole doping in the CuO_2 planes, and hence the strength of the superconductivity [67].

YBCO was also the first high- T_c superconductor in which the vortex lattice structure was studied using SANS [68]. Over the last 30 years, extensive studies on the vortex lattice have been done as technical developments have allowed higher and higher magnetic field

ranges to be accessed.

In this chapter, we will provide a summary of what is known about the vortex lattice in YBCO, focussing on detwinned $\text{YBa}_2\text{Cu}_3\text{O}_7$ with T_c of ~ 89 K, where the CuO chains are fully occupied. We will then present new results on the field and temperature dependence of the vortex lattice form factor at higher fields than previously measured, and consider how that affects our understanding of the superconductivity in this material (Paper V and Paper VI). The highest field results were taken with TOF SANS, using the data analysis methods developed in Section 2.3.2.1 and Paper I.

4.1. PREVIOUS SANS STUDIES ON YBCO

The vortex lattice in $\text{YBa}_2\text{Cu}_3\text{O}_7$ undergoes a series of structural transitions as the applied magnetic field increases. White *et al.* [69] first reported the full series of first-order transitions in the structure up to 10.8 T at 2 K.

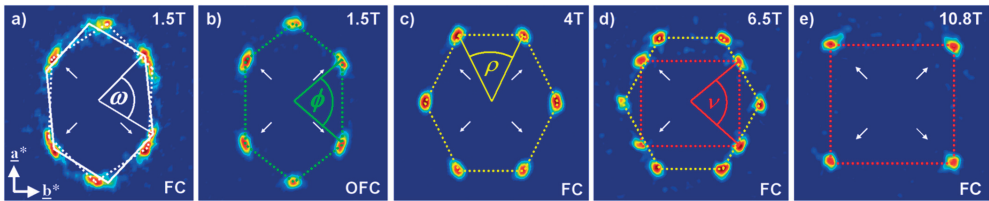


Figure 4.1: VL diffraction patterns of YBCO measured from 1.5 T to 10.8 T with the applied magnetic field parallel to the c -axis of the sample. Picture taken from [69].

As shown in Figure 4.1 (a,b), the vortex lattice is oriented as a distorted hexagonal pattern aligned along the crystal structure of the sample; we refer to this as the low-field structure (LFS). On increasing the magnetic field, the vortex lattice structure rotates by 90° as shown in Figure 4.1 (c), labeled as the intermediate-field structure (IFS). Both the LFS and IFS are stretched along the \mathbf{a} direction of the crystal. When increasing the field, the structure undergoes another VL transition to a rhombic structure, labelled as

high-field structure (HFS), as shown in Figure 4.1 (e). The HFS is distorted along the \mathbf{b} direction of the crystal. In Figure 4.1 (e) both IFS and HFS phases are visible at the same time.

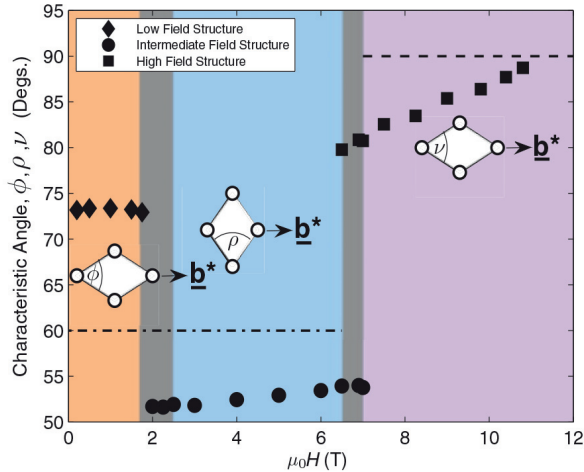


Figure 4.2: Field dependence of the opening angle (specified in Figure 4.1) at 2K for $\text{YBa}_2\text{Cu}_3\text{O}_7$. Dark grey areas denote where the VL structure transitions happen. Figure taken from [48].

We also see, from Figure 4.2, that the opening angle keeps increasing for higher magnetic fields. Trying to find a simple description of the VL transitions in Ref. [48], they realised that no existing model could completely describe the field dependence of the $\text{YBa}_2\text{Cu}_3\text{O}_7$ VL structure. The most suitable model is the one provided by Kogan *et al.* [70,71]. This model considers nonlocal effects coming from the band structure anisotropy as the most likely cause of the field transition between the LFS and the IFS. A similar interpretation might explain the high-field transition from hexagonal to the rhombic structure, even though this transition is not expected from the model. However, it could also be understood as a consequence of the predominantly d -wave gap, because in $\text{YBa}_2\text{Cu}_3\text{O}_7$ the coherence length of the carriers from the CuO chains is expected to be different to that of the carriers in the CuO_2 layers, which will affect the orientation of the superconducting gap nodes, as observed by Kirtley *et al.* [64].

Turning now to the form factor, White *et al.* also measured this at 2 K in $\text{YBa}_2\text{Cu}_3\text{O}_7$ [48]. In Figure 4.3 (Left) is shown the form factor of the different Bragg spots, with the different colours denoting the different VL structures. The location of the reflections with respect to the rocking axis (see Section 2.2.1) is also denoted for the LFS and IFS cases. We can see where the transitions happen at 1.75T and 2.5T and 6.5T and 7T for the low-field and high-field transitions, respectively.

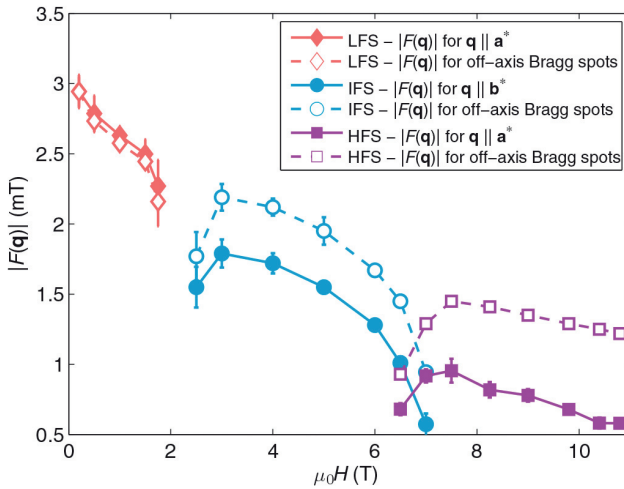


Figure 4.3: Field dependence of the form factor measured at 2 K. Figure taken from [48].

To model the form factor behaviour as a function of magnetic field, the local London model is used, with an anisotropic correction to account for the biaxial anisotropy of $\text{YBa}_2\text{Cu}_3\text{O}_7$

$$F(q) = \frac{\langle B \rangle \exp[-c(q_x^2 \xi_b^2 + q_y^2 \xi_a^2)]}{q_x^2 \lambda_a^2 + q_y^2 \lambda_b^2} \quad (4.1)$$

where $\langle B \rangle$ is the average internal induction, which we will simplify as approximately the applied magnetic field, λ_i is the penetration depth arising from the supercurrents flowing in the direction i , ξ_i is the coherence length in the i -direction and (q_x, q_y) are the Cartesian components of the \mathbf{q} vector. As we explained in Section 2.2.1.1, we introduced a Gaussian cutoff for the finite size of the cores with a value of $c = 0.44$ (Eq. (2.13)).

After fitting the form factor from the Bragg spots with $\mathbf{q} \parallel \mathbf{a}^*$ and then fitting the form factor from the off-axis Bragg spots, White *et al.* found values of ξ_i that are overes-

timated, since they give value of the upper critical field that is too low, and values of λ_i in good agreement with previous (lower-field) SANS studies [72]. The overestimation of ξ_i was explained by White *et al.* as being due to the VL disorder, which can be quantified by introducing the Debye-Waller factor into the measured intensity, $\exp(-q^2\langle u^2\rangle/4)$, where $\langle u^2\rangle$ is the root-mean-square displacement of a vortex along the direction of \mathbf{q} .

The temperature dependence of the form factor at 0.2 T and 5.0 T was also measured by White *et al.* [48] (see Figure 4.4). To fit the LFS data (Figure 4.4 (a)), the modified London model from Eq. (4.1) was used, including the temperature dependence of the penetration depth, $\lambda_{a/b}(T)$, assuming that $1/\lambda_{a/b}^2(T)$ has the same temperature dependence of $\rho_{s,a/b}(T)$ from Eq. (5.3). Assuming a single d -wave gap function, a gap $\Delta_0(0) = 25(2)$ meV was reported that is very similar to the value reported in previous μ SR experiments [66].

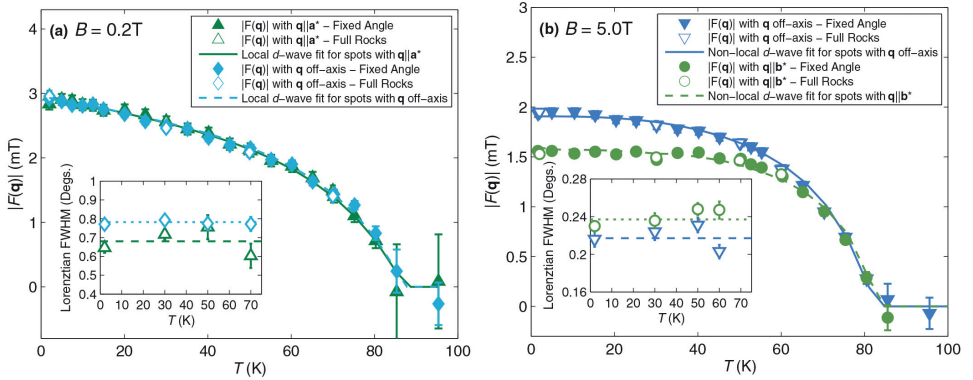


Figure 4.4: Temperature dependence of the form factor for the different Bragg spots in the LFS regime (a) and the IFS (b). Solid and dashed lines correspond to fittings to the data assuming a d -wave gap. The insets correspond to the temperature dependence of the FWHM of the measured rocking curves. Figures taken from [48].

When modelling the temperature dependence of the form factor in the HFS regime, it is clear that d -wave nonlocal effects become much more robust, and the penetration depth dependence should be

$$\frac{1}{\lambda_{a/b}^2(T)} = 1 - [1 - \rho_{s,a/b}(T)] \left(\frac{T_c + T^*}{T_c} \right) \left(\frac{T^2}{T^2 + (T^*)^2} \right) \quad (4.2)$$

where T^* is the intersection temperature between both spot types, where at 5.0 T is $T^* = 51.4$ K. The results of the fit are shown in Figure 4.4 (b). However, the fits give poor values for both λ_i and ξ_i , but we see an increase of $\lambda_i(0)$ and a decrease of $\xi_i(0)$ with increasing field, which is consistent with the observed trend in μ SR studies [73, 74].

Cameron *et al.* [75] provided a continuation of these YBa₂Cu₃O₇ SANS studies, extending the field range from 10.8 T to 16.7 T, exploring the HFS configuration. For these measurements, the London theory with nonlocality corrections also fails to adequately describe the evolution of the vortex lattice along field and temperature.

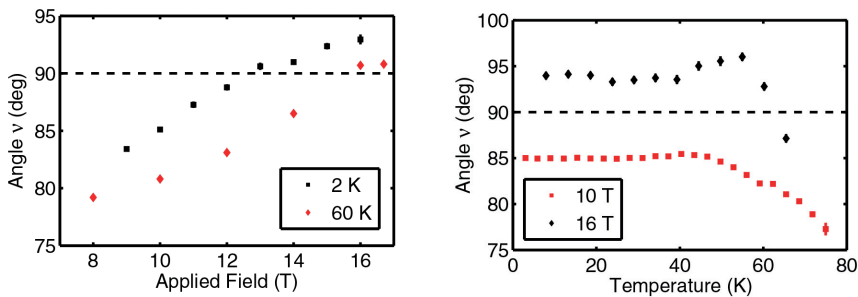


Figure 4.5: Field (left) and temperature (right) dependence of the opening angle. Values were taken at 2 and 60 K and 10 and 16 T, respectively. Pictures taken from [75].

From Figure 4.5 (Left), we observe an increase of the opening angle towards a square structure for increasing magnetic field. At 2 K, the VL structure passes through the square configuration, suggesting that the nodal positions on the chain Fermi surface are moving with the field, which is further discussed in Paper V and by Kirtley *et al.* [64]. Also, in Figure 4.5 (Right), as expected from the suppression of nonlocal effects, the VL structure evolves to a hexagonal structure on approaching T_c .

Furthermore, trying to replicate the behaviour of the field dependence of the form factor by using the modified London model from Eq. (4.1) by using the values of λ_i and ξ_i obtained in Ref. [48], we see in Figure 4.6 (Left) that the fits are not in good agreement with the data. For the temperature dependence data, a similar behaviour as the one observed in Figure 4.4 is also spotted in Figure 4.6 (Right), where the form factor seems constant with temperature up to an *irreversibility temperature* above which the form factor drops

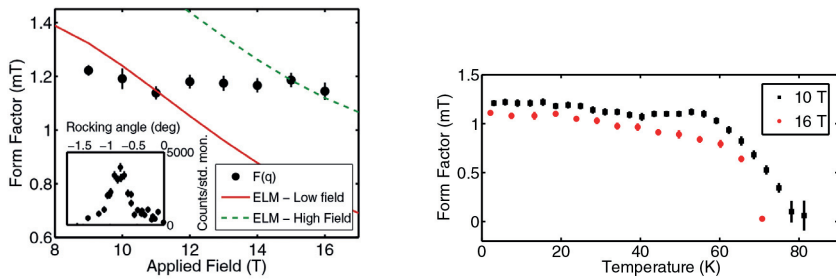


Figure 4.6: Field (left) and temperature (right) dependence of the form factor measured at 2 K and 10 and 16 T, respectively. Pictures taken from [75].

to zero, and nonlocal effects are suppressed. However, we can see a weak temperature dependence at 16 T that nonlocal effects in high fields may explain.

To explore further the temperature and field dependence of the opening angle and the form factor, driven by the CuO chain order parameter, and to complete the VL structure phase diagram, we decided to conclude this series of SANS studies by measuring the VL structure and form factor of $YBa_2Cu_3O_7$ up to 25.9 T (Paper V). Another angle that we pursue is to try to alter the superconductivity in $YBa_2Cu_3O_{7-\delta}$ by chemical doping without altering the CuO chain structures (Paper VI).

4.2. HIGH FIELD SANS STUDIES ON $YBa_2Cu_3O_7$ AND $Ca_xY_{1-x}Ba_2Cu_3O_7$

In high- T_c superconductors, like $YBa_2Cu_3O_{7-\delta}$ (YBCO), the doping level can be used to tune the observed properties. Usually, δ is the doping control parameter in YBCO, which varies the occupancy of the oxygen chains running along the \mathbf{b} -axis of the crystal. Changing the amount of oxygen alters the number of holes available, tuning the superconductivity. However, these changes to the oxygen levels also alter the fraction of chains filled with oxygen, giving rise to additional structural and electronic effects that can be hard to separate. The (d -wave) superconductivity in YBCO develops primarily from the CuO_2 planes, but s -wave superconductivity also develops from the chains [64]; this can be seen

in the distortion of the vortex lattice previously shown in Figure 4.5. We can dope the yttrium site with calcium instead to avoid these complications, resulting in a higher hole concentration than fully over-doped YBCO. The specific effects of including calcium are still under study, as it will also distort the lattice due to the differences in ionic radii [76,77].

For this reason, we performed a set of SANS experiments on a $\text{YBa}_2\text{Cu}_3\text{O}_7$ up to 25.9 T and on a 15% Ca-doped YBCO sample, $\text{Ca}_{0.15}\text{Y}_{0.85}\text{Ba}_2\text{Cu}_3\text{O}_7$, up to 25 T to see if it behaves in the same way as its parent compound.

As a continuation of the previously mentioned SANS studies on $\text{YBa}_2\text{Cu}_3\text{O}_7$, two different experiments were performed in 2016 and 2017 at the High Magnetic Field Facility for Neutron Scattering [78] which consisted of the High Field Magnet (HFM) [79] and the EXtreme Environment Diffractometer (EXED) [80] at the Helmholtz-Zentrum Berlin (HZB). Each of those experiments was focussed on the study of the $\text{YBa}_2\text{Cu}_3\text{O}_7$ flux line lattice at fields up to 25 and 25.9 T, studying the field (HZB 2016 experiment) and temperature (HZB 2017 experiment) behaviour. To supplement these data, we also performed three additional lower-field SANS experiments, at HZB in 2019, ILL in 2021 and PSI in 2021, on a $\text{Ca}_{0.15}\text{Y}_{0.85}\text{Ba}_2\text{Cu}_3\text{O}_7$ sample to provide a full comparison with $\text{YBa}_2\text{Cu}_3\text{O}_7$.

The VL structure can be described by the angle between two diffraction spots, ν , which is bisected by the \mathbf{b}^* direction. Figure 4.7 shows the opening angle, ν , as a function of magnetic field for both compounds, $\text{YBa}_2\text{Cu}_3\text{O}_7$ and $\text{Ca}_{0.15}\text{Y}_{0.85}\text{Ba}_2\text{Cu}_3\text{O}_7$ (see Paper V and Paper VI).

As we can observe in Figure 4.7 (top), for $\text{YBa}_2\text{Cu}_3\text{O}_7$, above 6.5 T, the VL adopts a high-field centered-rectangular arrangement [48, 69, 81], and reduces the anisotropy with increasing field. Between 11 and 12 T, the centred rectangle passes through a square arrangement, and it does not vary much from this value, reaching a maximum value of 100° at high fields, where it seems the vortex lattice stabilizes. This strongly suggests that the VL arrangement is connected to the nodes in the order parameter [64], which would be at 45° if YBCO were a pure d -wave superconductor.

As we have mentioned, in a purely d -wave superconductor, the nodes would lie at exactly 45° to both \mathbf{a} and \mathbf{b} axes. From Figure 4.7 (right), the position of the nearest-neighbor vortex directions are approximately at 45° (within $\pm 5^\circ$) to the \mathbf{a}^* and \mathbf{b}^* axes

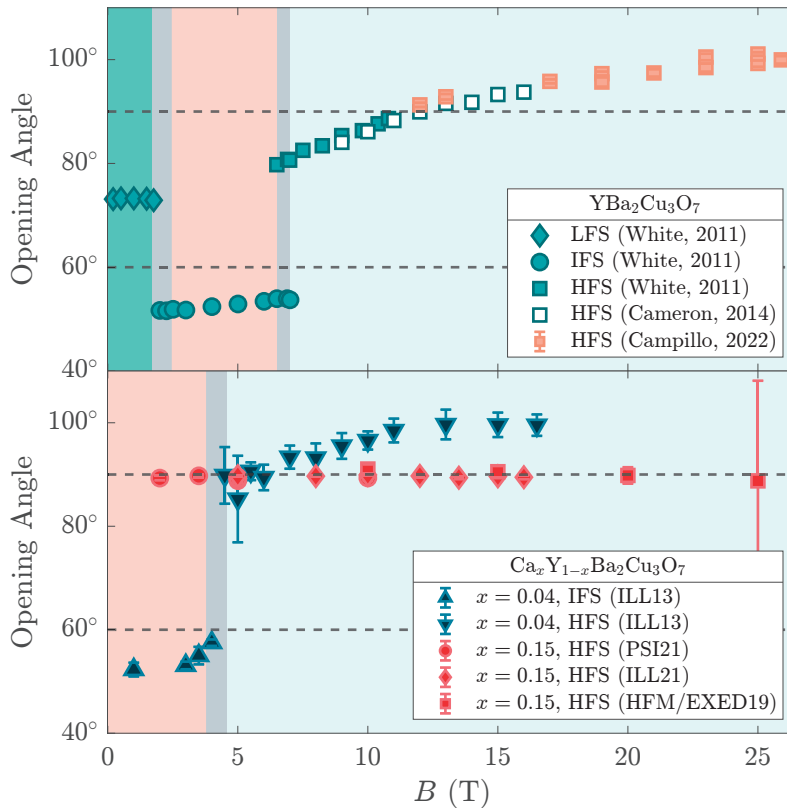


Figure 4.7: The evolution of the vortex lattice structure with magnetic field at base temperature for (top) $\text{YBa}_2\text{Cu}_3\text{O}_7$ and (bottom) $\text{Ca}_x\text{Y}_{1-x}\text{Ba}_2\text{Cu}_3\text{O}_7$. (Top) The orange squared points are from the work presented in this thesis while the other points are drawn from Refs. [48] and [75]. (Bottom) The red symbols are the opening angle of $\text{Ca}_{0.15}\text{Y}_{0.85}\text{Ba}_2\text{Cu}_3\text{O}_7$ and the blue symbols belongs to the opening angle of $\text{Ca}_{0.04}\text{Y}_{0.96}\text{Ba}_2\text{Cu}_3\text{O}_7$.

(or equivalently to the \mathbf{a} and \mathbf{b} axes in real space) along the whole field range. At 25 T it seems to start to deviate from the square arrangement caused by the melting of the vortex line lattice when approaching to the upper critical field of $\text{Ca}_{0.15}\text{Y}_{0.85}\text{Ba}_2\text{Cu}_3\text{O}_7$. We expect that Ca doping will greatly reduce B_{c2} , apart from changing the superconducting behaviour.

Figure 4.7 (right) may be an indication that the superconducting charge carriers along

the \mathbf{b} direction are suppressed by incrementing the calcium doping, due to the increase of holes in the system [77]. Furthermore, it seems that the s -wave superconductivity that may be arised by the CuO chains. However, no field transition is observed from a low-field hexagonal to a high-field rhombic structure, which is a clear indication of a d -wave order parameter.

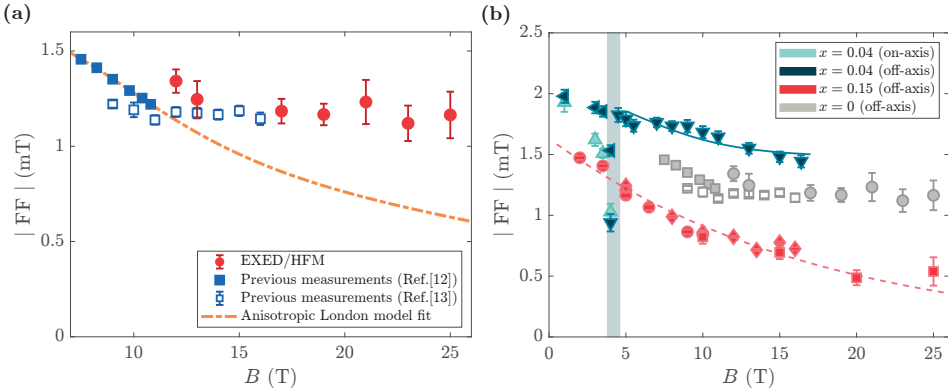


Figure 4.8: (a) The vortex lattice form factor as a function of magnetic field in $\text{YBa}_2\text{Cu}_3\text{O}_7$. The red points are the new data obtained in the experiment at HZB in 2016; the blue points are drawn from Refs. [48, 75]. The orange line is a fit to the blue squares using an anisotropic London model specified in the main text. (b) Field dependence of the vortex lattice form factor in $\text{Ca}_x\text{Y}_{1-x}\text{Ba}_2\text{Cu}_3\text{O}_7$. The $\text{Ca}_{0.15}\text{Y}_{0.85}\text{Ba}_2\text{Cu}_3\text{O}_7$ data were obtained at HZB in 2019 and at ILL and PSI in 2021. The square points in the field dependence have been multiplied by a normalization factor of 1.5 to account for a loss in intensity observed due to a change in the detector between the HZB 2016 and 2017 experiments. This normalization constant has been confirmed by the experiment performed at the same facility in 2019.

Now we turn to the field-dependence of the form factor, shown in Figure 4.8. For fields much less than B_{c2} , it is expected that the form factor will obey a London model, extended to include the effects of overlapping vortex cores of size $\sim \xi$, the coherence length. However, the observed field dependence for $\text{YBa}_2\text{Cu}_3\text{O}_7$ cannot be fit by the London model (see Figure 4.8 (left)), with the VL remaining much more robust at high fields than would be expected from the suppression of spatial Fourier components of the field by VL core

overlap (see Paper V).

In contrast, we observe a constant decay of the VL form factor of $\text{Ca}_{0.15}\text{Y}_{0.85}\text{Ba}_2\text{Cu}_3\text{O}_7$, which can be easily fitted to the Brandt model (Eq. (2.13)). From the fitting we obtain that $B_{c2} = 47(3)$ T, suggesting that the upper critical field is severely reduced due to the effect of the doping, as suggested by Grissonanche *et al.* [82]. These results agree with the reduction in the critical temperature observed in $\text{Ca}_{0.15}\text{Y}_{0.85}\text{Ba}_2\text{Cu}_3\text{O}_7$ samples where $T_c = 57$ K [83].

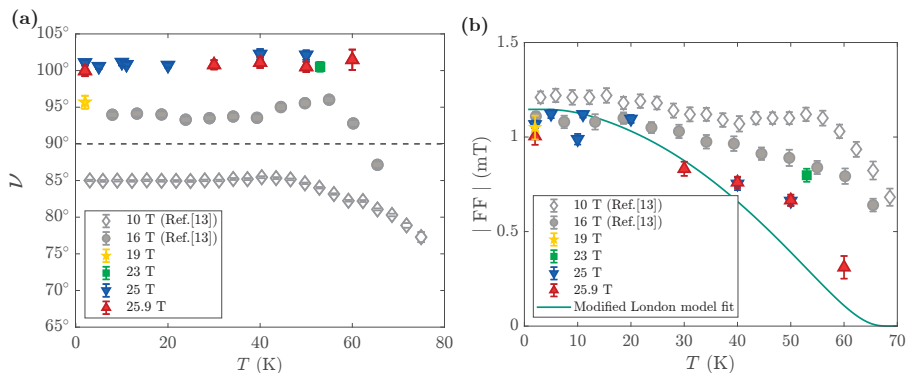


Figure 4.9: (Left) Temperature dependence of the opening angle with temperature at 25, 25.9 T with two single points at 19 T and 23 T. The grey points are from a previous study [75] and are provided for reference. (Right) The temperature dependence of the vortex lattice form factor. The points in color are from this work and the grey points are from Ref. [75] for comparison. The blue line is discussed in the main text. The color points in the temperature dependence have been multiplied by a normalization factor of 1.5 to account for a loss in intensity observed due to a change in the detector between the HZB 2016 and 2017 experiments. This normalization constant has been confirmed by the experiment performed at the same facility in 2019.

By observing the evolution with temperature of the vortex lattice structure at 25 T and 25.9 T in Figure 4.9 (left), the VL is frozen at 100° and there is no evidence of a decrease on approaching T_c . However, during this experiment, the beam did not have enough intensity to measure the vortex lattice closer to its melting point. This may suggest that the change on the vortex lattice structure could happen even closer to T_c , which is in good agreement

with what have been observed in previous SANS studies [48, 75]. It is important to point out that we did not observe any variation between 40° and 60° , as it was seen at 16 T.

Figure 4.9 (right) shows the temperature dependence of the form factor with temperature. It shows a clear decrease when approaching to the upper critical field and this decrease arises at higher temperatures compared with the temperatures dependencies observed at 10 T and 16 T. We have fitted the temperature dependence assuming $d + s$ pairing [54], where

$$\Delta(T, \varphi) = \Delta_{0,d}(T) \cos(2\varphi) + \Delta_{0,s}(T) \quad (4.3)$$

where $\Delta_{0,s}(T) = -\cos(100^\circ)\Delta_{0,d}(T)$ to give nodes at the observed angle. We also assume that $\Delta_{0,d}(0) = 2.14k_B T_c$ [54], with $B_{c2} = 120$ T [84] and $T_c = 70$ K at 25 T [82]. This model also fails to follow the temperature dependence of the form factor at high fields, especially at temperatures above 40 K, indicating again that the expected description breaks down.

It should be pointed out that additional work has been done on $\text{Ca}_{0.04}\text{Y}_{0.96}\text{Ba}_2\text{Cu}_3\text{O}_7$. This information has not been included in this chapter since the data recollection was completed before the beginning of this thesis but temperature and field dependence analysis have been done as a part of Paper VI.

4.3. SUMMARY

In this chapter we have reviewed previous SANS experiments performed on $\text{YBa}_2\text{Cu}_3\text{O}_7$, including the different VL phase transitions along field, the field and temperature dependence of the form factor and the melting point of the VL at different magnetic fields.

As we have pointed out, $\text{YBa}_2\text{Cu}_3\text{O}_7$ is expected to have an upper magnetic field of $B_{c2} \sim 120$ T, so all previous measurements have been constrained by the instrumental limit, not being able to measure the $\text{YBa}_2\text{Cu}_3\text{O}_7$ VL above 17 T. From the measurements performed at HZB at three different experiments in 2016, 2017 and 2019, we were able to measure the VL of $\text{YBa}_2\text{Cu}_3\text{O}_7$ and $\text{Ca}_{0.15}\text{Y}_{0.85}\text{Ba}_2\text{Cu}_3\text{O}_7$ up to 25.9 T.

Our results for $\text{YBa}_2\text{Cu}_3\text{O}_7$ are a clear indication that high magnetic fields tend to destroy superconducting pairing in the carriers traveling along the crystal \mathbf{b} direction (CuO chains) in this material. This leads to a field-dependent change in the superconducting anisotropy, which will be reflected in a change in the angular position of the order-parameter nodes in this orthorhombic ($d+s$)-wave material. In addition, we find that the intensity of the diffraction signal from the vortex lattice hardly falls off at high fields and the standard models do not account for the field and temperature dependencies of the form factor for these fields. We speculate that this may be due to Pauli paramagnetic effects in the vortex cores, and a future aim is to test our model from [Chapter 3](#) on the results from YBCO.

Comparing these results with the ones obtained for $\text{Ca}_{0.15}\text{Y}_{0.85}\text{Ba}_2\text{Cu}_3\text{O}_7$, we see a clear indication that the Ca-doping adds holes into the material, affecting not only the structure but also to the superconductivity of the material. $\text{Ca}_{0.15}\text{Y}_{0.85}\text{Ba}_2\text{Cu}_3\text{O}_7$ does not carry out a phase transition along field, and remains square over the whole field range. Furthermore, the field dependence of the form factor shows an exponential decay along field, that may suggest a reduce in the B_{c2} . Contrary to $\text{YBa}_2\text{Cu}_3\text{O}_7$, this field dependence follows the London model prediction and along with our observations of the vortex lattice opening angle, it seems that adding this much Ca to the sample kills the s -wave contribution of the material. These conclusions are in good agreement of what have been observed in a $\text{Ca}_{0.05}\text{Y}_{0.95}\text{Ba}_2\text{Cu}_3\text{O}_7$ sample, specified in [Paper VI](#).

CHAPTER 5

Small-angle neutron scattering studies on topological superconductor candidates

In particle physics, a Dirac fermion is a spin-1/2 particle with its own antiparticle, with the same mass and spin but opposite charge. All fermions in the standard model are Dirac fermions, which can be expressed with a complex field with different particles and antiparticles. In 1937, Ettore Majorana suggested that Dirac equation could be splitted in two real wave equations, each of those representing a real fermionic field but where every particle represents their own antiparticle. These kind of elemental particles are known as Majorana fermions. By definition, any fermionic state can be expressed as a superposition of two Majorana fermions that are spatially separated.

These kind of particles are expected to be found in condensed matter systems, like superconductors, where quasiparticle excitations (Bogoliubov quasiparticles) are given by a superposition of an electron and hole states. As previously explained in [Section 1.4](#), in BCS theory the s -wave pairing symmetry forms pairs of electrons with opposite spin. The Bogoliubov annihilation operator in a s -wave superconductor is expressed as

$$b = uc_{\uparrow}^{\dagger} + vc_{\downarrow} \tag{5.1}$$

where c_{σ} annihilates a fermion with σ spin projection. In the same way, Majorana fermions

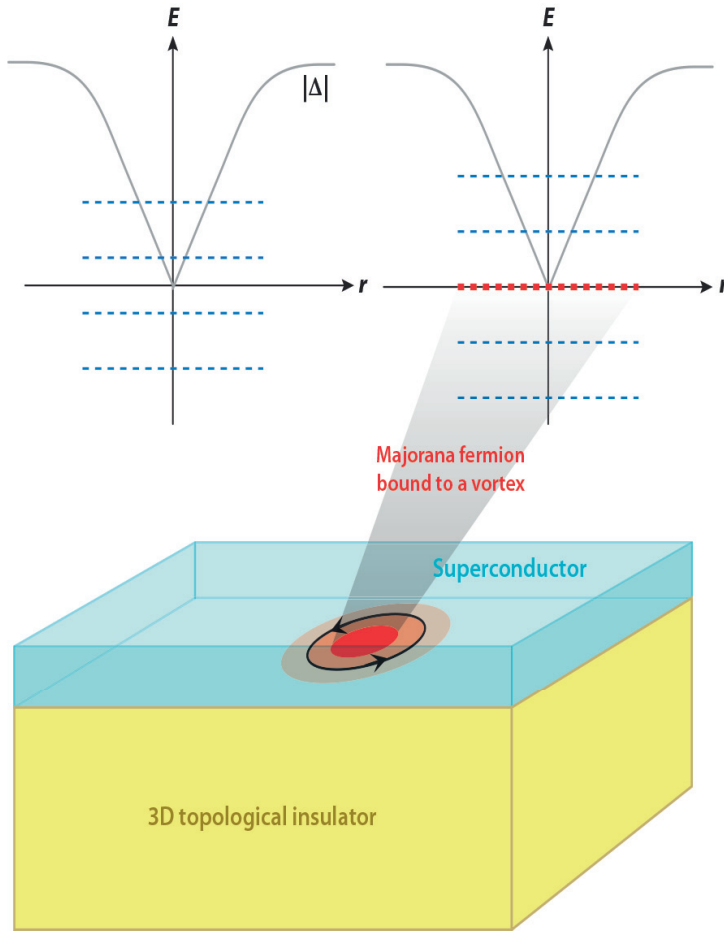


Figure 5.1: (Left) Superconducting pair potential, $\Delta(0)$ (solid gray line), on an s -wave superconductor and subgap states (dashed blue lines) around $E = 0$. (Right) Sequence of energy levels induced on the surface of a 3D topological insulator with a midgap state at $E = 0$, corresponding to the Majorana fermion state (dotted red line). Picture taken from Ref. [85].

can be related to an annihilation operator of the form

$$\gamma = uc_{\sigma}^{\dagger} + u^{*}c_{\sigma}, \quad (5.2)$$

equal to the creation operator $\gamma = \gamma^\dagger$, satisfying the principal characteristic of Majorana fermions. In contrast to Bogoliubov operators, Majorana fermion operators that make up the Majorana fermion have equal spin projections.

Spin degeneracy needs to be broken to give rise to an unpaired Majorana fermion. Because of that, Majorana fermions can arise in vortices and on the edges of superconductors with triplet pairing systems [86]. Then, the topological property for materials with p -wave superconductivity is the existence of spatially separated Majorana fermions [87]. However, conventional s -wave superconductors in combination with strong spin-orbit coupling of a topological insulator could be used, as shown in [Figure 5.1](#). A 3D topological insulator has an insulating bulk and a metallic surface where a layered superconductor is located. This opens up an excitation gap and when applying a magnetic field, the Abrikosov vortex penetrates with subgap states with energies $E_n \approx (n + \alpha)\Delta^2/E_F$, where $n = 0, \pm 1, \pm 2, \dots$. The zero mode solution $E_0 = 0$ would correspond to a Majorana fermion and, at the Fermi level, it accomplishes the requirement $\gamma(0) = \gamma(E) = \gamma^\dagger(-E)$ [85].

Majorana fermions and their potential to store quantum information [85, 88] have attracted a lot of attention for future applications in quantum computation since they lead to bound states which follow non-Abelian statistics, and, in theory, could be used as qubits [87]. This has impeded the research and characterization of s -wave superconductors as possible candidates of topological superconductors.

In this chapter we focus our attention on three particular materials that have been argued to have topological features: PbTaSe_2 , Au_2Pb and $\beta\text{-Bi}_2\text{Pd}$. We will present the most recent discoveries about them and we will discuss our neutron diffraction experiments that were performed in order to throw some light on their pairing mechanisms and superconducting parameters.

5.1. TOPOLOGICAL SUPERCONDUCTOR CANDIDATES

As we mentioned before, for realizing intrinsic topological superconductors, we focus on s -wave superconductors with strong spin-orbit coupling environment. This spin-orbit coupling permits breaking of time-reversal symmetry in the vortex state under certain conditions [89]. However, the superconductor must be fully gapped to permit odd numbers of Majorana bound states in the cores. s -wave superconductors with topological surface states at the Fermi level can show $p_x \pm ip_y$ even when the bulk superconductivity is s -wave [90].

At present, the existence of a natural topological superconductor is still a challenge, but several candidates have been proposed, including PbTaSe_2 , Au_2Pb and $\beta\text{-Bi}_2\text{Pd}$.

5.1.1. PbTaSe_2

In non-centrosymmetric superconductors, the presence of asymmetric spin-orbit coupling arises due to a mixture of spin-singlet and spin-triplet coupling in their superconducting state, although the spin-singlet order parameter is the dominant one. There have been many experiments performed to resolve the pairing system of PbTaSe_2 , including specific heat, electrical resistivity and magnetic susceptibility measurements. These experiments indicate that PbTaSe_2 is a fully gapped BCS s -wave superconductor with a critical temperature of $T_c = 3.8$ K at $H = 0$ T [91] and an upper critical field is $H_{c2} = 0.32$ T at $T = 0$ K [92].

Materials with strong spin-orbit correlations not only show exotic spin systems or can behave as topological insulators, but can also manifest relativistic Dirac electrons. PbTaSe_2 is a notable candidate which has been shown to have a bulk Dirac cone in its band structure. Its unusual electronic structure shows a single-layer Pb sublattice, similar to that observed in graphene, with a Dirac point at K (see Figure 5.2) generating 3D massive Dirac fermions and broken inversion symmetry by large spin-orbit coupling.

Various STM studies have been carried out to determine if the two-dimensional Pb

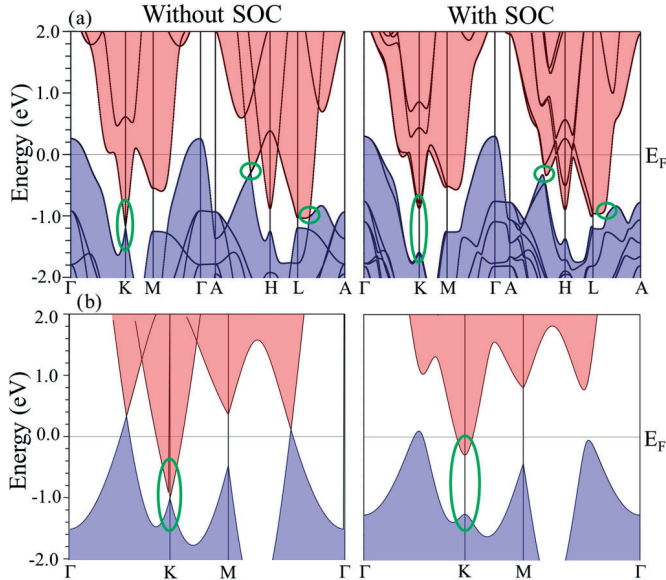


Figure 5.2: (a) Simulation of PbTaSe_2 electronic bands with and without spin-orbit coupling where an opened gap is observed when spin-orbit coupling is included. The Dirac cone at K at band crossings that are gapped are circled in green. (b) Electronic structure of the Pb sublattice with the Dirac cone at K circled in green. Pictures taken from Ref. [91].

sample surface presents topological surface states at the Fermi level. As reported in Ref. [90], a BCS superconducting gap below the bulk T_c is revealed to have a size of $2\Delta \sim 0.90$ meV that follows the expected temperature dependence for a fully-gapped s -wave superconductor. Since for an intrinsic topological superconductor the interface between the surface and the bulk is not clearly defined, the induced gap on the topological superconducting surface is expected to be roughly the same size as the size of the bulk gap size, as is the case in PbTaSe_2 .

5.1.1.1. SANS experiment on PbTaSe_2

The main purpose of our neutron experiment performed at the NG7 SANS instrument at the National Institute of Standards and Technology (NIST) was to study the vortex lattice in an array of PbTaSe_2 samples of less of 0.5 mm of thickness arranged on an

aluminium plate (see Figure 5.3 (Left)). The samples were aligned with the c -axis parallel the field and the neutron beam, and a [110] direction in the horizontal scattering plane. It was installed in a 9 T cryomagnet with cooling by helium exchange gas. After several trials we were not able to observe the vortex lattice. There are several possible reasons for this, including that the vortex lattice was too close to the beam centre to be resolved, that the signal was too weak to be detected, or that sample quality led to a very disordered vortex lattice that we could not resolve.

We also performed temperature scans counting while cooling or warming up at different magnetic fields (see Figure 5.3 (Right)). We could observe a drop in intensity at 0.05 T and 2.5 K. However when we performed three other temperature scans to check if this drop corresponded to any transition to the normal state, we observed this decay in intensity at other fields over and close to H_{c2} , suggesting that the drop in intensity was not related to the transition from the superconducting to the normal state. This increase in intensity was caused by the condensation of the helium exchange gas in the sample can, so that more neutrons could be detected as they were not scattered by the helium gas.

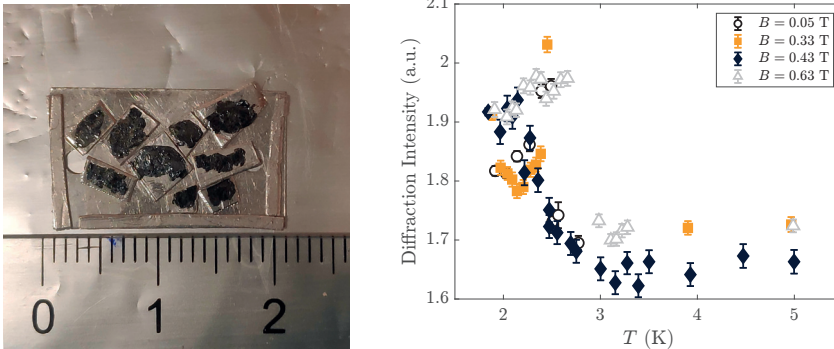


Figure 5.3: (Left) Array of PbTaSe₂ samples of less of 0.5 mm of thickness arranged on an aluminium plate. (Right) Temperature dependence of the total counts on the detector at 0.05 T, 0.33 T, 0.43 T and 0.63 T.

Another group also searched independently for the vortex lattice in this material using the D33 instrument at ILL [93], but no signal from the vortex lattice was observed during this experiment either.

5.1.2. Au₂Pb

As in the case of PbTaSe₂, Au₂Pb has been proposed as a candidate to study the interaction of superconductivity and topological surface states. On cooling, Au₂Pb undergoes two structural phase transitions. Above 100 K it is a cubic Laves phase but below that temperature an unknown crystal structure appears. Then at 55 K, it undergoes a phase transition to the low temperature crystal structure which is primitive orthorhombic and it remains unchanged below 40 K [94] and then finally becoming superconducting below 1.2 K.

Several studies have been carried out on Au₂Pb in its normal and superconducting states [94, 95], showing that the specific heat jump, $\Delta C/(\gamma T_c) = 1.95$, is higher than the BCS value of 1.43 with a weak coupling $\lambda_{ep} = 0.58$. This suggests it is a weakly coupled BCS superconductor that is fully gapped in the bulk.

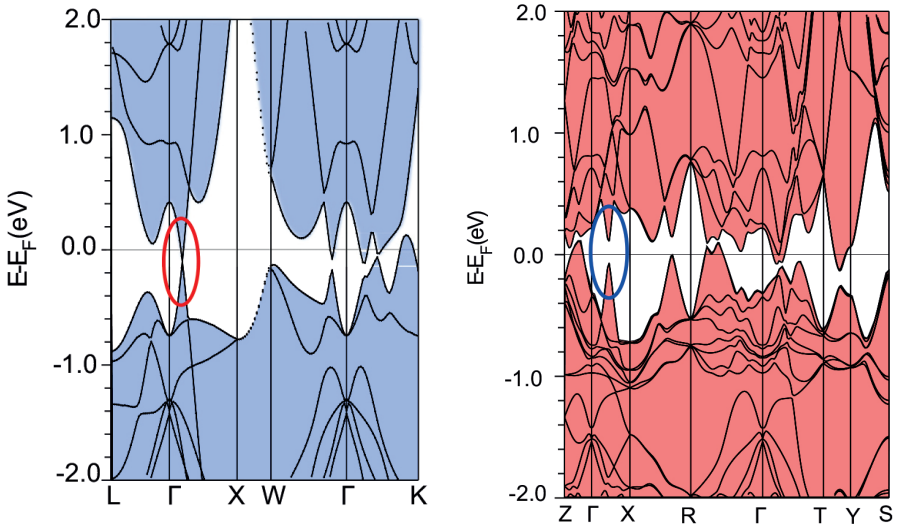


Figure 5.4: Electronic band structure of Au₂Pb (left) in the cubic high temperature phase and (right) in the orthorhombic low temperature phase. The cubic structure has a Dirac cone along $\Gamma - X$ that gets gapped when the crystal is distorted at low temperatures. Pictures taken from Ref. [94].

The calculated electronic bands for Au_2Pb at low and high temperature are shown in Figure 5.4. As we can observe, it is predicted to have a crossing along the $\Gamma - X$ direction at high temperature (> 100 K) but are gapped when transitioning to the low temperature regime (< 40 K), suggesting that there must be massless Dirac electrons around the Fermi level in the cubic phase. Thus Au_2Pb is one of the very few materials predicted to have a 3D Dirac cone at high temperatures. Since an opened gap is observed (Figure 5.4 (Right)), it is a potential topological insulator. Thus Au_2Pb could be an important material in which interaction between superconductivity and topological surface states may be observed.

5.1.2.1. SANS experiment on Au_2Pb

We received time to carry out a small angle neutron scattering study of the vortex lattice of Au_2Pb at D33 in the Institute Laue-Langevin [96], with the aim of investigating the superconducting gap further, to confirm that it is fully gapped, hence meeting the requirements to be a natural topological superconductor candidate. A set of several Au_2Pb samples, grown at the Universidad Autónoma de Madrid, were aligned on an aluminium plate in three different orientations: orienting the $[001]$ crystal direction out of the plate, orienting the $[111]$ direction out of plane and putting the samples in a plate in a random direction (Figure 5.5 (Left)). However, none of the three sets of samples gave a clear signal (Figure 5.5 (Right)) and no rocking curve coming from the vortex lattice could be observed.

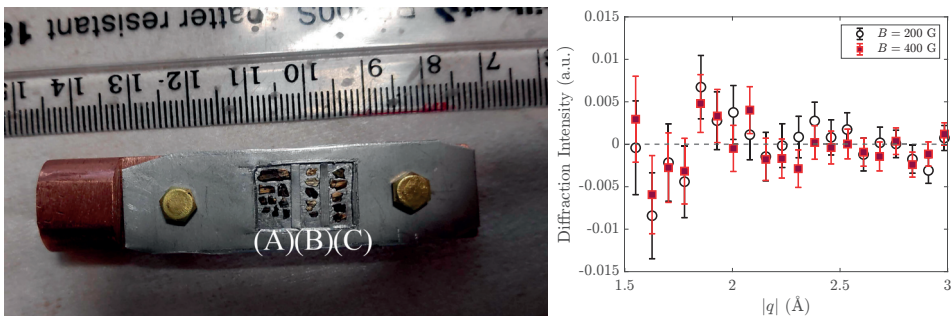


Figure 5.5: (Left) Set of aligned samples of Au_2Pb where the normal crystallographic axis to the plane is (a) $[001]$, (b) $[111]$ and (c) a random direction. (Right) Diffraction intensity in terms of $|q|$ measured at 100 mK and at 200 G and 400 G respectively in set B.

5.1.3. β -Bi₂Pd

Tetragonal β -Bi₂Pd has been proposed to be a multi-gap s -wave superconductor. In recent STM studies [97], a hexagonal vortex lattice was observed, with $T_c = 5$ K, following a single s -wave gap behaviour but showing multigap properties in the mixed state. When measuring the temperature dependence of tunneling conductance at zero field, the data follows a single-gap s -wave behaviour of $\Delta(0) = 0.76$ meV with the expected $\Delta(T)$ from BCS theory. Multigap superconductivity is usually related to a positive curvature of H_{c2} , but such an increase is not observed, and $H_{c2}(T)$ shows the influence of a multiband Fermi surface with a single superconducting gap.

In the literature, there are conflicting reports, using various techniques, with other studies pointing to a standard superconducting gap [98,99]. Some of this work also points to the possible existence of topologically protected surface states [100]. When scanning the superconducting gap size on β -Bi₂Pd thin films, grown by molecular beam epitaxy, two pairs of conductance peaks are revealed at two different energy scales indicating two different superconducting gaps: the smallest one, Δ_b matching with values previously reported 0.76 – 0.92 meV and the new one discovered, Δ_s , revealed from topological surface states (Figure 5.6 (Left)) and vanishes below 6.2 K (Figure 5.6 (Right)). This opens the possibility that Δ_s has its origin at the surface of epitaxial β -Bi₂Pd thin films, due to the existence of topological surface states. This has been previously theorised, where Dirac fermions on the surface of β -Bi₂Pd enhance Δ_b and time reversal symmetry, leading to a larger superconducting gap Δ_s .

Furthermore, when growing β -Bi₂Pd samples with a higher flux ratio, a larger Δ_s emerges with a negligible Δ_b and density of states, leading to a nodeless pairing gap, as a consequence of suppressing bulk superconductivity. This may be a signal of intrinsic topological superconductivity present in the surface of β -Bi₂Pd as an s -wave conventional superconductor.

In Paper VII, specific heat and neutron-scattering measurements were performed to obtain more information about the nature of the superconducting gap in β -Bi₂Pd at higher fields than previously studied in this material.

In the electronic specific heat measurements, at 4.8 K a clear jump is observed revealing

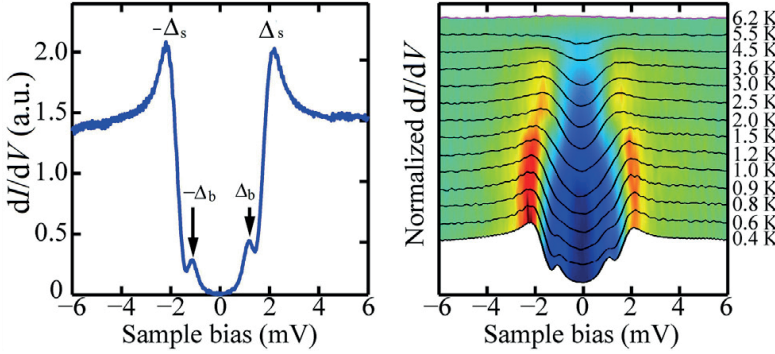


Figure 5.6: (Left) Differential conductance dI/dV spectrum measured on β - Bi_2Pd at 0.4 K, showing two superconducting gaps denoted as Δ_s and Δ_b . (Right) Temperature dependence of dI/dV in β - Bi_2Pd . Pictures taken from Ref. [100].

the critical temperature of the sample, where the flat region at low temperatures indicates a nodeless gap. When fitting the data with different values of the gap with the weak coupling value ($\Delta_0/k_B T_c = 1.76$, blue dotted and dashed line) and with the strong coupling value ($\Delta_0/k_B T_c = 2.0$, green dashed line), we see in [Figure 5.7](#) that the heat capacity follows the strong coupling model.

To check the results found by the specific heat measurements, the vortex lattice of β - Bi_2Pd was measured using SANS, with the magnetic field pointing parallel to the c -axis of the sample, rotated a few degrees away to break the degeneracy of the FLL. As we stayed in [Section 2.4.2](#), we applied Bayesian analysis to obtain an improved visualization of the vortex lattice, as shown in [Figure 2.5](#). However, for the flux line lattice measured at $H = 0.1$ T, the degeneracy is not completely broken and the VL appeared as a ring instead of a six-spot pattern. However, at higher fields, $H = 0.2, 0.3$ and 0.4 T we can observe six clear spots that decrease in intensity with increasing field. In [Figure 5.7](#), at $H = 0.1$ T, there is a plateau up to $0.2T/T_c$ which indicates a full-gap behaviour from the system and then the intensity decreases with increasing temperature as expected. However, the width of the plateau decreases with increasing field and it may be indicating some contribution from a multi-band Fermi surface.

By calculating the form factor obtained from the vortex lattices using the London-

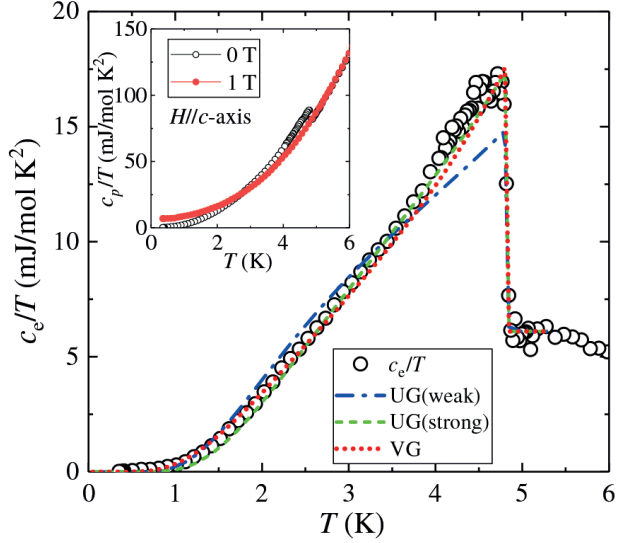


Figure 5.7: Temperature dependence of the electronic specific with fits to different gap models, as specified in the text. Picture taken from [Paper VII](#).

Brandt expression, [Eq. \(2.13\)](#), at different fields, and taking into account that the form is proportional to the superfluid intensity, $|F|^2 = \rho_s^2$, we found that temperature dependence of the intensity cannot be explained with a single gap, suggesting a non-constant gap for different regions of the Fermi surface. For that reason, we used a superfluid density expression for a two-dimensional Fermi surface [54]

$$\rho_s(T) = 1 - \frac{1}{4\pi k_B T} \int_0^{2\pi} d\phi \int_0^{\text{inf}} \cosh^{-2} \left(\frac{\sqrt{\epsilon^2 + \Delta_k^2(\phi, T)}}{2k_B T} \right) d\epsilon \quad (5.3)$$

where the gap function is defined by angular- and temperature-dependent terms, $\Delta_k(\phi, T) = \Delta_k(\phi)\Delta_t(T)$, defining a varying gap value across the Fermi surface $\Delta_k(\phi) = \sqrt{\Delta_A^2 + \Delta_B^2 \cos^2(2\phi)}$, with the *s*-wave ($\Delta_k(\phi) = \Delta_A$) and *d*-wave gap ($\Delta_k(\phi) = \Delta_B \cos(2\phi)$) models combined. The size of the flat-region from [Figure 5.8](#) is mainly determined by the minimum value Δ_A . By fitting the data using the *s*-wave model (either for the weak and the strong coupling cases), the *d*-wave model and the varying model, we find that the varying model is the more appropriate one at low fields. Moreover, the value of Δ_A decreases with field and the behaviour of the specific heat can be well-reproduced with the varying model. From

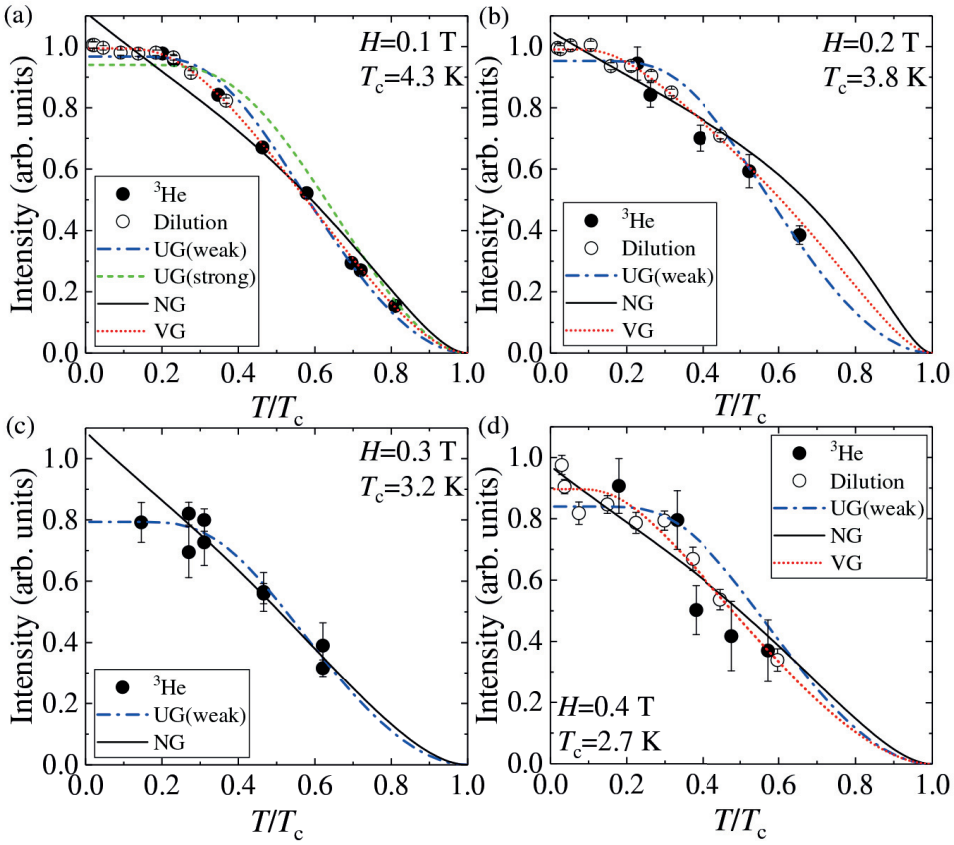


Figure 5.8: Temperature dependence vortex lattice intensities measured at $H = 0.1, 0.2, 0.3$ and 0.4 T. Picture taken from [17].

these recent neutron results we can conclude that β -Bi₂Pd has a non-uniform gap along the Fermi surface and the two-gap model is magnetic-field dependent.

All of this information serves as a preamble to study the characteristic lengths of the superconductor and to investigate the effect of the field orientation on the bulk lattice of β -Bi₂Pd using neutron scattering.

5.2. VL BENDING AND CHARACTERISTIC LENGTHS IN β -Bi₂Pd

Vortex lattices in s -wave superconductors show a variety of structural transitions driven by the orientation of the field as a consequence of the "hairy ball" theorem [101]. There exist different ways in which the flux line lattice can fulfill the "hairy ball" theorem: no preferred FLL orientation is chosen; two or more degenerate structures develop with different orientation; or the FLL changes its shape with the field direction, as seen dramatically in SANS studies of high-purity niobium [101]. For niobium, when the field is parallel to the c -axis, the flux-lattice has a square-arrangement (with two degenerate domains) but when rotating the magnetic field away from [001] the FLL is continuously distorted [3]. In contrast of what have been observed in Nb, there are no VL transitions when rotating the magnetic field in β -Bi₂Pd.

A recent scanning tunnelling microscopy (STM) study [102] looked at the effect of the field orientation on the vortices, by using a vector magnet to control the exact alignment of the field with respect to the sample surface normal. As with other STM studies on this material, when the field is parallel to the surface normal, a standard hexagonal lattice is seen. However, by tilting the sample 80° with respect to the magnetic field, it was found that the vortices had the same shape and size as in the case where the magnetic field was completely normal to the surface, indicating that the vortices must bend below the surface and only the arrangement of vortices varies proportional to $\cos(\theta)$ as shown in [Figure 5.9](#). It is important to point out that the density of bent vortices is the same as if they were straight and the vortices are just shifted by the effect of the direction of the magnetic field.

In [Paper VIII](#), we aimed to study the distortion of the vortex lattice and obtain the values for the penetration depth and the coherence length.

We requested time at D33 in the Institut Laue-Langevin (ILL, France) to investigate the effect of the field orientation on the bulk lattice, and to see if the behaviour in the bulk is as expected based on the inferences made in the STM study [102]. A set of nine samples, prepared at the Universidad Autónoma de Madrid, were aligned on an aluminium plate along the [110] direction with their [001] axes perpendicular to the plane, using the

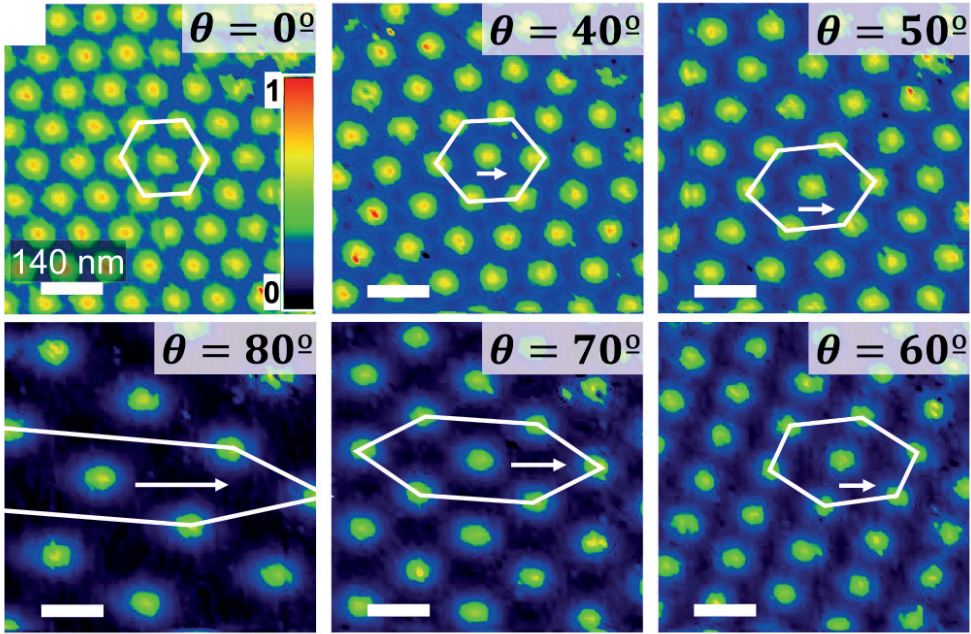


Figure 5.9: STM images of the zero-bias density of states (normalized conductance), as measured at 0.3 T and 0.15 K. The angle noted in each panel indicates the orientation of the field with respect to the sample surface normal. The white arrows indicate the tilt direction. Picture taken from [102].

Laue neutron-diffractometer OrientExpress (ILL). The mosaic sample was installed in a horizontal-field cryomagnet, with a sample base temperature of 1.4 K. An independent SANS experiment was performed on SANS-I at the Heinz Maier-Leibnitz Zentrum (MLZ, Germany) with a single crystal of β -Bi₂Pd. The crystal was mounted on a ³He refrigerator, with its [010]-axis in the vertical direction, also with the [001] out of plane. The results of both independent experiments were combined in [Paper VIII](#). In the rest of this section, the results from our experiment on D33 are highlighted, but the conclusions draw from both experiments.

In both experiments, the sample orientation with respect to the field was altered, and the effect on the bulk vortex lattice observed. In our ILL experiment, we collected neutron diffraction patterns from the vortex lattice at $T = 1.4$ K and $\mu_0 H = 0.1$ T and 0.15 T

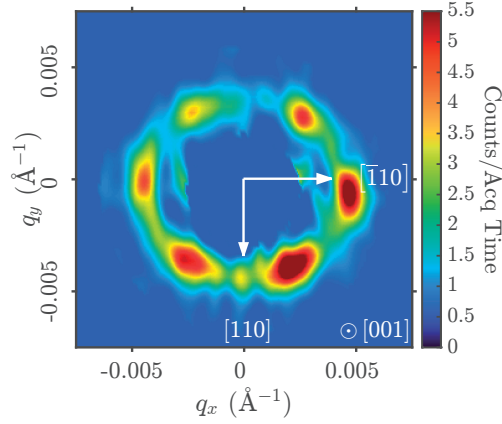


Figure 5.10: Example of the vortex lattice pattern of β -Bi₂Pd at 1.4 K and 0.1 T with $\Omega = 70^\circ$ measured at D33 (ILL). Smoothing was applied to the picture.

for $\Omega = 0^\circ, 30^\circ$ and 70° (see **Figure 5.10**), where Ω is defined to be the angle between the c -axis of the sample and the applied magnetic field. For all field values, both samples provided very similar results (see **Figure 5.11** (a)). As indicated in **Figure 5.11** (b), the total diffracted intensity decreases with temperature, as we expect qualitatively, but this change is not affected by the rotation of the sample with respect to the field.

In the anisotropic London model, the aspect ratio of the ellipse, Γ_{VL} , which circumscribes the vortex lattice is given by the expression

$$\Gamma_{\text{VL}} = A \left(\frac{1}{\gamma_\lambda^2 \sin^2 \Omega + \cos^2 \Omega} \right)^{-1/2} \quad (5.4)$$

where γ_λ and A is a constant introduced for non-perfect hexagonal lattice at $\Omega = 0^\circ$. The result of the fit gives $A = 0.984(5)$ and $\gamma_\lambda = 1.192(9)$. Accordingly, the low-temperature ratio of the penetration depths due to supercurrents flowing along the c -axis and those in the basal plane, λ_c/λ_{ac} is 1.192. In anisotropic Ginzburg-Landau theory, this ratio should also be equal to the ratio H_{c2}^{ab}/H_{c2}^c , which was estimated to have the very similar value of 1.25(4) in the magnetization measurement.

By using the integrated intensities from the top and bottom spots from the VL measured in the MLZ experiment, the dependence of the form factor on field with $H \parallel c$ -axis at $T = 0.87$ K was estimated and therefore, by using the Brandt expression (**Eq. (2.13)**) and

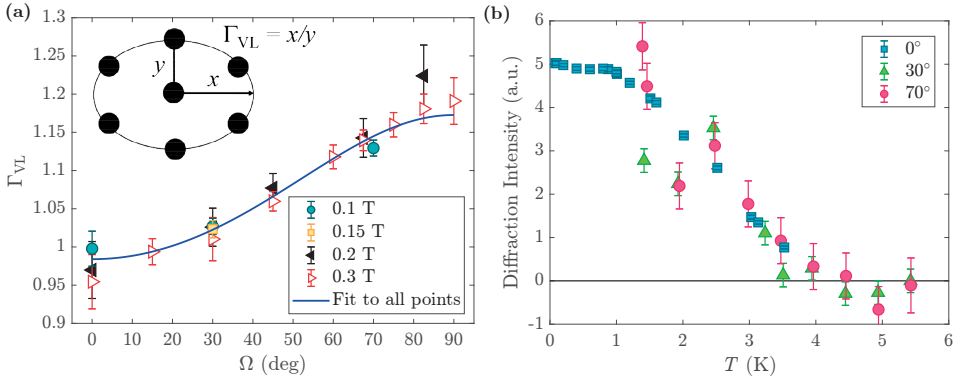


Figure 5.11: (a) Ω -dependence of the aspect ratio of the ellipse which circumscribes the vortex lattice of β - Bi_2Pd . The solid blue line corresponds to the fit to Eq. (5.4). (b) Temperature dependence of the total VL diffracted intensity at $\Omega = 0^\circ, 30^\circ$ and 70° measured at $\mu_0 H = 0.1$ T.

	ab	c
λ (nm)	291(7)	
χ (nm)	24.5(7)	
κ		11.9(4)
$\mu_0 H_{c1}$ (mT)	5.2(2)	5.8(3)
$\mu_0 H_{c2}$ (T)	0.69(3)	0.55(2)

Table 5.1: Superconducting parameters of β - Bi_2Pd obtained by neutron scattering.

choosing $c = 0.44$, we obtained the superconducting characteristic lengths along the basal plane $\lambda_{ab} = 291(7)$ nm and $\xi_{ab} = 24.5(7)$ nm. From those quantities and from the ratio H_{c2}^{ab}/H_{c2}^c obtained from magnetic susceptibility measurements we were able to calculate the rest of superconducting parameters shown in Table 5.1.

5.3. SUMMARY

In this chapter, a brief overview of topological superconductors and how Majorana fermions are expected to be observed in them is given.

We have performed several SANS studies on natural topological superconductor candidates to confirm if they are fully-gapped as expected. From PbTaSe₂ no vortex lattice was observed in our experiment. It is important to remark that another experiment was performed in parallel for the same material at ILL and also the VL could not be observed. This suggests that the transmission of the sample is too low to make the VL visible above the background from the sample holder, and that significantly more sample mass is required to be successful. We also performed a SANS experiment on Au₂Pb, and were also not able to observe its VL. In this case, this was due to experimental difficulties, in particular the low temperature structural transition which made co-alignment of the samples challenging.

Finally, we successfully studied the superconductor β -Bi₂Pd and were able to observe and estimate the VL anisotropy of the superconductor β -Bi₂Pd in the bulk using SANS measurements in the mixed state. Our measurements agree with the measurements performed during the experiment done by our collaborators at MLZ and show that the detected intensity from the VL is invariant under the rotation of the sample with respect to the field direction. Our estimates of superconducting quantities are in good agreement with previous microscopic measurements [97, 103]. However, even though in [Paper VII](#) we reported multiband effects from the field dependence of the two-gap model used, we did not observe any field dependence of the superconducting parameters.

Conclusions

In this thesis we have studied the vortex lattices of several unconventional superconductors like the heavy-fermion superconductor CeCu_2Si_2 , the topological superconductor candidate $\beta\text{-Bi}_2\text{Pd}$ and the high-temperature superconductors $\text{YBa}_2\text{Cu}_3\text{O}_7$ and $\text{Ca}_{0.15}\text{Y}_{0.85}\text{Ba}_2\text{Cu}_3\text{O}_7$, using SANS techniques.

In [Paper VII](#) and [Paper VIII](#) we have carried out a complete study of the field dependence of the superfluid density, penetration depth and coherence length in the superconductor $\beta\text{-Bi}_2\text{Pd}$. We also performed several SANS experiments on other topological superconductor candidates without success. One of the biggest challenges with these experiments has been the alignment of the samples and the sample environment necessary for observing the VL of these materials, especially for the cases of PbTaSe_2 and Au_2Pb .

We have then observed behaviour in both heavy fermion ([Paper III](#)) and cuprate superconductors ([Paper V](#), [Paper VI](#)) that cannot be explained within the extended London model.

In [Paper III](#) on CeCu_2Si_2 , we have been able to measure the form factor across the entirety of the superconducting phase in our S-type sample. As a result, we could confirm the existence of Pauli paramagnetic effects when approaching to B_{c2} , as previously reported in the well-known Ce-based superconductor CeCoIn_5 . There is an active debate about gap symmetry in CeCu_2Si_2 , and our results do not match with a d -wave model. They also favour the existence of a double s -wave gap, but we cannot rule out the single s -wave case.

To make these assessments we have developed a new model ([Paper IV](#)), based on the London model and previous calculations from Eilenberger theory, which is able to reproduce the form factor for both CeCu_2Si_2 and CeCoIn_5 . We would like to test its applicability to other superconductors which may show Pauli paramagnetic behaviour.

In our work on YBCO ([Paper V](#), [Paper VI](#)), there are deviations from the extended

London model at the highest fields measured. These deviations exist also at lower fields, but can be compensated for by changing the penetration depth or coherence length. However, we are now able to show that the observed deviations cannot be explained within the extended London model. We have speculated that Pauli paramagnetic effects may be responsible, and the next step would be to apply the model in [Paper IV](#) to this data.

The particularity of these high field experiments is that they were performed at the HFM/EXED instrument which was able to reach a magnetic field of 25.9 T - ideal for expanding our information about their pairing mechanism and the behaviour of the form factor at the highest field that has ever been reported with SANS. To be able to quantitatively analyse these data, we developed a new protocol for obtaining the form factor of superconductors studied by TOF instruments ([Paper I](#)). This is particularly important for future work in this area, as the number of monochromatic instruments around the world has declined. This method will be applied to other superconductors which have been studied in HFM/EXED, like $(\text{Ba}_{0.5}\text{K}_{0.5})\text{Fe}_2\text{As}_2$.

Bibliography

- [1] H. K. Onnes *Leiden Comn. 120b, 122b, 124c*, 1911.
- [2] W. Meissner and R. Ochsenfeld, “Ein neuer effekt bei eintritt der supraleitfähigkeit,” *Naturwissenschaften*, vol. 21, no. 44, pp. 787–788, 1933.
- [3] S. Mühlbauer, C. Pfeiderer, P. Böni, M. Laver, E. Forgan, D. Fort, U. Keiderling, and G. Behr, “Morphology of the superconducting vortex lattice in ultrapure niobium,” *Physical Review Letters*, vol. 102, no. 13, p. 136408, 2009.
- [4] A. Michels, *Magnetic Small-Angle Neutron Scattering: A Probe for Mesoscale Magnetism Analysis*, vol. 16. Oxford University Press, 2021.
- [5] M. R. Eskildsen, *Small Angle Neutron Scattering Studies of the Flux Line Lattices in the Borocarbide Superconductors*. PhD thesis, Risø National Laboratory, Roskilde, Denmark, 1998.
- [6] D. Christen, F. Tasset, S. Spooner, and H. Mook, “Study of the intermediate mixed state of niobium by small-angle neutron scattering,” *Physical Review B*, vol. 15, no. 9, p. 4506, 1977.
- [7] A. Yaouanc, P. D. de Réotier, and E. Brandt, “Effect of the vortex core on the magnetic field in hard superconductors,” *Physical Review B*, vol. 55, no. 17, p. 11107, 1997.
- [8] M. R. Eskildsen, “Vortex lattices in type-II superconductors studied by small-angle neutron scattering,” *Frontiers of Physics*, vol. 6, no. 4, pp. 398–409, 2011.
- [9] E. Brandt, “Ginsburg-Landau theory of the vortex lattice in type-II superconductors for all values of κ and B ,” *Physica Status Solidi (b)*, vol. 51, no. 1, pp. 345–358, 1972.

- [10] M. Eskildsen, P. Gammel, B. Barber, A. Ramirez, D. Bishop, N. Andersen, K. Mortensen, C. Bolle, C. Lieber, and P. Canfield, “Structural stability of the square flux line lattice in $\text{YNi}_2\text{B}_2\text{C}$ and $\text{LuNi}_2\text{B}_2\text{C}$ studied with small angle neutron scattering,” *Physical Review Letters*, vol. 79, no. 3, p. 487, 1997.
- [11] J. R. Clem, “Simple model for the vortex core in a type II superconductor,” *Journal of Low Temperature Physics*, vol. 18, no. 5, pp. 427–434, 1975.
- [12] Z. Hao, J. R. Clem, M. McElfresh, L. Civale, A. Malozemoff, and F. Holtzberg, “Model for the reversible magnetization of high- κ type-II superconductors: Application to high- T_c superconductors,” *Physical Review B*, vol. 43, no. 4, p. 2844, 1991.
- [13] *Small Angle Neutron Scattering*. No. 1486 in TECDOC Series, Vienna: INTERNATIONAL ATOMIC ENERGY AGENCY, 2006.
- [14] C. D. Dewhurst, GRASP: Graphical Reducation and Analysis SANS Program for Matlab, <https://www.ill.eu/users/support-labs-infrastructure/software-scientific-tools/grasp/>.
- [15] O. Arnold, J.-C. Bilheux, J. Borreguero, A. Buts, S. I. Campbell, L. Chapon, M. Doucet, N. Draper, R. F. Leal, M. Gigg, *et al.*, “Mantid—data analysis and visualization package for neutron scattering and μSR experiments,” *Nuclear Instruments and Methods in Physics Research Section A: Accelerators, Spectrometers, Detectors and Associated Equipment*, vol. 764, pp. 156–166, 2014.
- [16] A. T. Holmes, G. R. Walsh, E. Blackburn, E. M. Forgan, and M. Savey-Bennett, “A 17 T horizontal field cryomagnet with rapid sample change designed for beamline use,” *Review of Scientific Instruments*, vol. 83, no. 2, p. 023904, 2012.
- [17] M. Soda, N. Kagamida, S. Mühlbauer, E. M. Forgan, E. Campillo, M. Kriener, H. Yoshizawa, and H. Kawano-Furukawa, “Field dependence of superfluid density in $\beta\text{-PdBi}_2$,” *Journal of the Physical Society of Japan*, vol. 90, no. 10, p. 104710, 2021.
- [18] E. Campillo, R. Riyat, S. Pollard, P. Jefferies, A. Holmes, R. Cubitt, J. White, J. Gavilano, Z. Huesges, O. Stockert, *et al.*, “Observations of the effect of strong

- Pauli paramagnetism on the vortex lattice in superconducting CeCu_2Si_2 ,” *Physical Review B*, vol. 104, no. 18, p. 184508, 2021.
- [19] E. Jellyman, P. Jefferies, S. Pollard, E. Forgan, E. Blackburn, E. Campillo, A. Holmes, R. Cubitt, J. Gavilano, H. Wang, *et al.*, “Unconventional superconductivity in the nickel chalcogenide superconductor TlNi_2Se_2 ,” *Physical Review B*, vol. 101, no. 13, p. 134523, 2020.
- [20] E. Helfand and N. Werthamer, “Temperature and purity dependence of the superconducting critical field, H_{c2} . II,” *Physical Review*, vol. 147, no. 1, p. 288, 1966.
- [21] P. Fulde, “Cooper pair breaking,” *Modern Physics Letters B*, vol. 24, no. 26, pp. 2601–2624, 2010.
- [22] A. M. Clogston, “Upper limit for the critical field in hard superconductors,” *Physical Review Letters*, vol. 9, no. 6, p. 266, 1962.
- [23] B. Chandrasekhar, “A note on the maximum critical field of high-field superconductors,” *Applied Physics Letters*, vol. 1, no. 1, pp. 7–8, 1962.
- [24] K. Maki, “Effect of Pauli paramagnetism on magnetic properties of high-field superconductors,” *Physical Review*, vol. 148, no. 1, p. 362, 1966.
- [25] S. Khim, B. Lee, J. W. Kim, E. S. Choi, G. Stewart, and K. H. Kim, “Pauli-limiting effects in the upper critical fields of a clean LiFeAs single crystal,” *Physical Review B*, vol. 84, no. 10, p. 104502, 2011.
- [26] M. Kenzelmann, “Exotic magnetic states in Pauli-limited superconductors,” *Reports on Progress in Physics*, vol. 80, no. 3, p. 034501, 2017.
- [27] C. Geibel, C. Schank, S. Thies, H. Kitazawa, C. Bredl, A. Böhm, M. Rau, A. Grauel, R. Caspary, R. Helfrich, *et al.*, “Heavy-fermion superconductivity at $T_c = 2\text{K}$ in the antiferromagnet UPd_2Al_3 ,” *Zeitschrift für Physik B Condensed Matter*, vol. 84, no. 1, pp. 1–2, 1991.
- [28] M. Kenzelmann, T. Strassle, C. Niedermayer, M. Sigrist, B. Padmanabhan, M. Zolliker, A. Bianchi, R. Movshovich, E. D. Bauer, J. L. Sarrao, *et al.*, “Coupled supercon-

- ducting and magnetic order in CeCoIn_5 ,” *Science*, vol. 321, no. 5896, pp. 1652–1654, 2008.
- [29] B. White, J. Thompson, and M. Maple, “Unconventional superconductivity in heavy-fermion compounds,” *Physica C: superconductivity and its applications*, vol. 514, pp. 246–278, 2015.
- [30] O. Stockert, J. Arndt, E. Faulhaber, C. Geibel, H. Jeevan, S. Kirchner, M. Loewenhaupt, K. Schmalzl, W. Schmidt, Q. Si, *et al.*, “Magnetically driven superconductivity in CeCu_2Si_2 ,” *Nature Physics*, vol. 7, no. 2, pp. 119–124, 2011.
- [31] F. Steglich, J. Aarts, C. Bredl, W. Lieke, D. Meschede, W. Franz, and H. Schäfer, “Superconductivity in the presence of strong pauli paramagnetism: CeCu_2Si_2 ,” *Physical Review Letters*, vol. 43, no. 25, p. 1892, 1979.
- [32] F. Steglich, P. Gegenwart, C. Geibel, R. Helfrich, P. Hellmann, M. Lang, A. Link, R. Modler, G. Sparn, N. Büttgen, *et al.*, “New observations concerning magnetism and superconductivity in heavy-fermion metals,” *Physica B: Condensed Matter*, vol. 223, pp. 1–8, 1996.
- [33] K.-i. Ueda, Y. Kitaoka, H. Yamada, Y. Kohori, T. Kohara, and K. Asayama, “ ^{29}Si Knight shift in the heavy-fermion superconductor CeCu_2Si_2 ,” *Journal of the Physical Society of Japan*, vol. 56, no. 3, pp. 867–870, 1987.
- [34] K. Fujiwara, Y. Hata, K. Kobayashi, K. Miyoshi, J. Takeuchi, Y. Shimaoka, H. Kotegawa, T. C. Kobayashi, C. Geibel, and F. Steglich, “High pressure NQR measurement in CeCu_2Si_2 up to sudden disappearance of superconductivity,” *Journal of the Physical Society of Japan*, vol. 77, no. 12, pp. 123711–123711, 2008.
- [35] K. Ishida, Y. Kawasaki, K. Tabuchi, K. Kashima, Y. Kitaoka, K. Asayama, C. Geibel, and F. Steglich, “Evolution from magnetism to unconventional superconductivity in a series of $\text{Ce}_x\text{Cu}_2\text{Si}_2$ compounds probed by Cu NQR,” *Physical Review Letters*, vol. 82, no. 26, p. 5353, 1999.
- [36] S. Kittaka, Y. Aoki, Y. Shimura, T. Sakakibara, S. Seiro, C. Geibel, F. Steglich, H. Ikeda, and K. Machida, “Multiband superconductivity with unexpected defi-

- ciency of nodal quasiparticles in CeCu_2Si_2 ,” *Physical Review Letters*, vol. 112, no. 6, p. 067002, 2014.
- [37] G. Volovik, “Superconductivity with lines of gap nodes: density of states in the vortex,” *JETP Letters*, vol. 58, no. 6, pp. 469–473, 1993.
- [38] N. Nakai, M. Ichioka, and K. Machida, “Field dependence of electronic specific heat in two-band superconductors,” *Journal of the Physical Society of Japan*, vol. 71, no. 1, pp. 23–26, 2002.
- [39] N. Nakai, P. Miranović, M. Ichioka, and K. Machida, “Field dependence of the zero-energy density of states around vortices in an anisotropic-gap superconductor,” *Physical Review B*, vol. 70, no. 10, p. 100503, 2004.
- [40] S. Kittaka, Y. Aoki, Y. Shimura, T. Sakakibara, S. Seiro, C. Geibel, F. Steglich, Y. Tsutsumi, H. Ikeda, and K. Machida, “Thermodynamic study of gap structure and pair-breaking effect by magnetic field in the heavy-fermion superconductor CeCu_2Si_2 ,” *Physical Review B*, vol. 94, no. 5, p. 054514, 2016.
- [41] T. Yamashita, T. Takenaka, Y. Tokiwa, J. A. Wilcox, Y. Mizukami, D. Terazawa, Y. Kasahara, S. Kittaka, T. Sakakibara, M. Konczykowski, *et al.*, “Fully gapped superconductivity with no sign change in the prototypical heavy-fermion CeCu_2Si_2 ,” *Science Advances*, vol. 3, no. 6, p. e1601667, 2017.
- [42] G. Pang, M. Smidman, J. Zhang, L. Jiao, Z. Weng, E. M. Nica, Y. Chen, W. Jiang, Y. Zhang, W. Xie, *et al.*, “Fully gapped d -wave superconductivity in CeCu_2Si_2 ,” *Proceedings of the National Academy of Sciences*, vol. 115, no. 21, pp. 5343–5347, 2018.
- [43] E. Blackburn, R. Cubitt, M. R. Eskildsen, E. M. Forgan, H. Kawano-Furukawa, A. T. Holmes, E. Jellyman, S. Kuhn, L. Lemberger, R. Riyat, and M. Takahashi, “Pauli limited behaviour in an iron-based superconductor?.” doi:10.5291/ILL-DATA.5-42-376, 2016. Institut Laue-Langevin (ILL).
- [44] E. Blackburn, E. Campillo, R. Cubitt, E. M. Forgan, A. T. Holmes, Z. Huesges, E. Jellyman, R. Riyat, and O. Stockert, “Vortex lattice of the heavy fermion su-

- perconductor CeCu_2Si_2 .” doi:10.5291/ILL-DATA.5-42-463, 2018. Institut Laue-Langevin (ILL).
- [45] S. Kitagawa, G. Nakamine, K. Ishida, H. Jeevan, C. Geibel, and F. Steglich, “Evidence for the presence of the Fulde-Ferrell-Larkin-Ovchinnikov state in CeCu_2Si_2 revealed using ^{63}Cu NMR,” *Physical Review Letters*, vol. 121, no. 15, p. 157004, 2018.
- [46] J. S. White, P. Das, M. R. Eskildsen, L. DeBeer-Schmitt, E. M. Forgan, A. D. Bianchi, M. Kenzelmann, M. Zolliker, S. Gerber, J. L. Gavilano, *et al.*, “Observations of Pauli paramagnetic effects on the flux line lattice in CeCoIn_5 ,” *New Journal of Physics*, vol. 12, no. 2, p. 023026, 2010.
- [47] M. Ichioka and K. Machida, “Vortex states in superconductors with strong Pauli-paramagnetic effect,” *Physical Review B*, vol. 76, no. 6, p. 064502, 2007.
- [48] J. White, R. Heslop, A. Holmes, E. Forgan, V. Hinkov, N. Egetenmeyer, J. Gavilano, M. Laver, C. Dewhurst, R. Cubitt, *et al.*, “Magnetic-field-induced nonlocal effects on the vortex interactions in twin-free $\text{YBa}_2\text{Cu}_3\text{O}_7$,” *Physical Review B*, vol. 84, no. 10, p. 104519, 2011.
- [49] E. Campillo, M. Bartkowiak, R. Riyat, E. Jellyman, A. S. Cameron, A. T. Holmes, O. Prokhnenko, W.-D. Stein, A. Erb, E. M. Forgan, and E. Blackburn, “Deviations from the extended London model in $\text{Yba}_2\text{Cu}_3\text{O}_7$,” *arXiv:2203.01705*, 2022.
- [50] M. Ichioka. Private communication, 2021.
- [51] L. Kramer and W. Pesch, “Core structure and low-energy spectrum of isolated vortex lines in clean superconductors at $T \ll T_c$,” *Zeitschrift für Physik*, vol. 269, no. 1, pp. 59–64, 1974.
- [52] N. Werthamer, E. Helfand, and P. Hohenberg, “Temperature and purity dependence of the superconducting critical field, H_{c2} . III. Electron spin and spin-orbit effects,” *Physical Review*, vol. 147, no. 1, p. 295, 1966.
- [53] K. Yosida, “Paramagnetic susceptibility in superconductors,” *Physical Review*, vol. 110, no. 3, p. 769, 1958.

- [54] R. Prozorov and R. W. Giannetta, “Magnetic penetration depth in unconventional superconductors,” *Superconductor Science and Technology*, vol. 19, no. 8, p. R41, 2006.
- [55] F. Gross, B. Chandrasekhar, D. Einzel, K. Andres, P. Hirschfeld, H. Ott, J. Beuers, Z. Fisk, and J. Smith, “Anomalous temperature dependence of the magnetic field penetration depth in superconducting UBe_{13} ,” *Zeitschrift für Physik B Condensed Matter*, vol. 64, no. 2, pp. 175–188, 1986.
- [56] K. M. Suzuki, Y. Tsutsumi, N. Nakai, M. Ichioka, and K. Machida, “Field evolution of the Fulde-Ferrell-Larkin-Ovchinnikov state in a superconductor with strong Pauli effects,” *Journal of the Physical Society of Japan*, vol. 80, no. 12, p. 123706, 2011.
- [57] K. M. Suzuki, K. Machida, Y. Tsutsumi, and M. Ichioka, “Microscopic Eilenberger theory of Fulde-Ferrell-Larkin-Ovchinnikov states in the presence of vortices,” *Physical Review B*, vol. 101, no. 21, p. 214516, 2020.
- [58] A. D. Bianchi, M. Kenzelmann, L. DeBeer-Schmitt, J. S. White, E. M. Forgan, J. Mesot, M. Zolliker, J. Kohlbrecher, R. Movshovich, E. D. Bauer, *et al.*, “Superconducting vortices in CeCoIn_5 : Toward the Pauli-limiting field,” *Science*, vol. 319, no. 5860, pp. 177–180, 2008.
- [59] P. Gegenwart, C. Langhammer, C. Geibel, R. Helfrich, M. Lang, G. Sparn, F. Steglich, R. Horn, L. Donnevert, A. Link, *et al.*, “Breakup of heavy fermions on the brink of “phase A” in CeCu_2Si_2 ,” *Physical Review Letters*, vol. 81, no. 7, p. 1501, 1998.
- [60] L. DeBeer-Schmitt, M. R. Eskildsen, M. Ichioka, K. Machida, N. Jenkins, C. Dewhurst, A. B. Abrahamsen, S. Bud’ko, and P. Canfield, “Pauli paramagnetic effects on vortices in superconducting $\text{TmNi}_2\text{B}_2\text{C}$,” *Physical Review Letters*, vol. 99, no. 16, p. 167001, 2007.
- [61] S. Özcan, D. Broun, B. Morgan, R. Haselwimmer, J. Sarrao, S. Kamal, C. Bidinosti, P. Turner, M. Raudsepp, and J. Waldram, “London penetration depth measurements

- of the heavy-fermion superconductor CeCoIn_5 near a magnetic quantum critical point,” *EPL (Europhysics Letters)*, vol. 62, no. 3, p. 412, 2003.
- [62] J. G. Bednorz and K. A. Müller, “Possible high T_c superconductivity in the Ba-La-Cu-O system,” *Zeitschrift für Physik B Condensed Matter*, vol. 64, no. 2, pp. 189–193, 1986.
- [63] M.-K. Wu, J. R. Ashburn, C. Torng, P.-H. Hor, R. L. Meng, L. Gao, Z. J. Huang, Y. Wang, and a. Chu, “Superconductivity at 93 K in a new mixed-phase Y-Ba-Cu-O compound system at ambient pressure,” *Physical review letters*, vol. 58, no. 9, p. 908, 1987.
- [64] J. Kirtley, C. Tsuei, C. Verwijs, S. Harkema, H. Hilgenkamp, *et al.*, “Angle-resolved phase-sensitive determination of the in-plane gap symmetry in $\text{YBa}_2\text{Cu}_3\text{O}_{7-\delta}$,” *Nature Physics*, vol. 2, no. 3, pp. 190–194, 2006.
- [65] H. Smilde, A. A. Golubov, G. Rijnders, J. Dekkers, S. Harkema, D. Blank, H. Rogalla, H. Hilgenkamp, *et al.*, “Admixtures to d -wave gap symmetry in untwinned $\text{YBa}_2\text{Cu}_3\text{O}_7$ superconducting films measured by angle-resolved electron tunneling,” *Physical review letters*, vol. 95, no. 25, p. 257001, 2005.
- [66] R. Khasanov, S. Strässle, D. Di Castro, T. Masui, S. Miyasaka, S. Tajima, A. Bussmann-Holder, and H. Keller, “Multiple gap symmetries for the order parameter of cuprate superconductors from penetration depth measurements,” *Physical Review Letters*, vol. 99, no. 23, p. 237601, 2007.
- [67] M. v. Zimmermann, J. Schneider, T. Frello, N. Andersen, J. Madsen, M. Käll, H. Poulsen, R. Liang, P. Dosanjh, and W. Hardy, “Oxygen-ordering superstructures in underdoped $\text{YBa}_2\text{Cu}_3\text{O}_{6+x}$ studied by hard x-ray diffraction,” *Physical Review B*, vol. 68, no. 10, p. 104515, 2003.
- [68] E. Forgan, D. M. Fault, H. Mook, P. Timmins, H. Keller, S. Sutton, and J. Abell, “Observation by neutron diffraction of the magnetic flux lattice in single-crystal $\text{YBa}_2\text{Cu}_3\text{O}_{7-\delta}$,” *Nature*, vol. 343, no. 6260, pp. 735–737, 1990.

- [69] J. White, V. Hinkov, R. Heslop, R. Lycett, E. Forgan, C. Bowell, S. Strässle, A. B. Abrahamsen, M. Laver, C. Dewhurst, *et al.*, “Fermi surface and order parameter driven vortex lattice structure transitions in twin-free $\text{YBa}_2\text{Cu}_3\text{O}_7$,” *Physical Review Letters*, vol. 102, no. 9, p. 097001, 2009.
- [70] V. Kogan, M. Bullock, B. Harmon, P. Miranović, L. Dobrosavljević-Grujić, P. Gammel, and D. Bishop, “Vortex lattice transitions in borocarbides,” *Physical Review B*, vol. 55, no. 14, p. R8693, 1997.
- [71] V. G. Kogan, P. Miranović, L. Dobrosavljević-Grujić, W. Pickett, and D. Christen, “Vortex lattices in cubic superconductors,” *Physical Review Letters*, vol. 79, no. 4, p. 741, 1997.
- [72] S. Johnson, E. Forgan, S. Lloyd, C. Aegerter, S. Lee, R. Cubitt, P. Kealey, C. Ager, S. Tajima, A. Rykov, *et al.*, “Flux-line lattice structures in untwinned $\text{YBa}_2\text{Cu}_3\text{O}_{7-\delta}$,” *Physical review letters*, vol. 82, no. 13, p. 2792, 1999.
- [73] J. Sonier, R. Kiefl, J. Brewer, D. Bonn, S. Dunsiger, W. Hardy, R. Liang, W. MacFarlane, T. Riseman, D. Noakes, *et al.*, “Magnetic field dependence of the london penetration depth in the vortex state of $\text{YBa}_2\text{Cu}_3\text{O}_{6.95}$,” *Physical Review B*, vol. 55, no. 17, p. 11789, 1997.
- [74] J. Sonier, J. Brewer, R. Kiefl, G. Morris, R. Miller, D. Bonn, J. Chakhalian, R. Heffner, W. Hardy, and R. Liang, “Field induced reduction of the low-temperature superfluid density in $\text{YBa}_2\text{Cu}_3\text{O}_{6.95}$,” *Physical review letters*, vol. 83, no. 20, p. 4156, 1999.
- [75] A. Cameron, J. White, A. Holmes, E. Blackburn, E. M. Forgan, R. Riyat, T. Loew, C. Dewhurst, and A. Erb, “High magnetic field studies of the vortex lattice structure in $\text{YBa}_2\text{Cu}_3\text{O}_7$,” *Physical Review B*, vol. 90, no. 5, p. 054502, 2014.
- [76] E. Liarokapis, D. Palles, D. Lampakis, G. Böttger, K. Conder, and E. Kaldis, “Phase separation in fully oxygenated $\text{Y}_{1-y}\text{Ca}_y\text{Ba}_2\text{Cu}_3\text{O}_x$ compounds,” *Physical Review B*, vol. 71, no. 1, p. 014303, 2005.

- [77] N.-C. Yeh, C.-T. Chen, G. Hammerl, J. Mannhart, A. Schmehl, C. W. Schneider, R. R. Schulz, S. Tajima, K. Yoshida, D. Garrigus, *et al.*, “Evidence of doping-dependent pairing symmetry in cuprate superconductors,” *Physical Review Letters*, vol. 87, no. 8, p. 087003, 2001.
- [78] O. Prokhnenko, P. Smeibidl, W.-D. Stein, M. Bartkowiak, and S. N., “HFM/EXED: The High Magnetic Field Facility for Neutron Scattering at BER II,” *Journal of Large-Scale Research Facilities*, vol. 3, p. A115, 2017.
- [79] P. Smeibidl, M. Bird, H. Ehmler, I. Dixon, J. Heinrich, M. Hoffmann, S. Kempfer, S. Bole, J. Toth, O. Prokhnenko, and B. Lake, “First Hybrid Magnet for Neutron Scattering at Helmholtz-Zentrum Berlin,” *IEEE Transactions on Applied Superconductivity*, vol. 26, p. 4301606, 2016.
- [80] O. Prokhnenko, W.-D. Stein, H.-J. Bleif, M. Fromme, M. Bartkowiak, and T. Wilpert, “Time-of-flight Extreme Environment Diffractometer at the Helmholtz-Zentrum Berlin,” *Rev. Sci. Instrum.*, vol. 86, p. 033102, 2015.
- [81] S. P. Brown, D. Charalambous, E. C. Jones, E. M. Forgan, P. G. Kealey, A. Erb, and J. Kohlbrecher, “Triangular to square flux lattice phase transition in $\text{YBa}_2\text{Cu}_3\text{O}_7$,” *Phys. Rev. Lett.*, vol. 92, p. 067004, 2004.
- [82] G. Grissonnanche, O. Cyr-Choinière, F. Laliberté, S. René de Cotret, A. Juneau-Fecteau, S. Dufour-Beauséjour, M.-E. Delage, D. LeBoeuf, J. Chang, B. Ramshaw, *et al.*, “Direct measurement of the upper critical field in cuprate superconductors,” *Nature Communications*, vol. 5, no. 1, pp. 1–8, 2014.
- [83] C. Bernhard and J. L. Tallon, “Thermoelectric power of $\text{Y}_{1-x}\text{Ca}_x\text{Ba}_2\text{Cu}_3\text{O}_{7-\delta}$: Contributions from CuO_2 planes and CuO chains,” *Physical Review B*, vol. 54, no. 14, p. 10201, 1996.
- [84] T. Sekitani, Y. H. Matsuda, and N. Miura, “Measurement of the upper critical field of optimally-doped $\text{YBa}_2\text{Cu}_3\text{O}_{7-\delta}$ in megagauss magnetic fields,” *New Journal of Physics*, vol. 9, no. 3, p. 47, 2007.

- [85] C. Beenakker, “Search for Majorana fermions in superconductors,” *Annu. Rev. Condens. Matter Phys.*, vol. 4, no. 1, pp. 113–136, 2013.
- [86] S. D. Sarma, C. Nayak, and S. Tewari, “Proposal to stabilize and detect half-quantum vortices in strontium ruthenate thin films: Non-Abelian braiding statistics of vortices in a $p_x + ip_y$ superconductor,” *Physical Review B*, vol. 73, no. 22, p. 220502, 2006.
- [87] M. Leijnse and K. Flensberg, “Introduction to topological superconductivity and Majorana fermions,” *Semiconductor Science and Technology*, vol. 27, no. 12, p. 124003, 2012.
- [88] A. Y. Kitaev, “Unpaired Majorana fermions in quantum wires,” *Physics-uspekhi*, vol. 44, no. 10S, p. 131, 2001.
- [89] M. Sato and Y. Ando, “Topological superconductors: a review,” *Reports on Progress in Physics*, vol. 80, no. 7, p. 076501, 2017.
- [90] S.-Y. Guan, P.-J. Chen, and T.-M. Chuang, “Topological surface states and superconductivity in non-centrosymmetric PbTaSe_2 ,” *Japanese Journal of Applied Physics*, 2021.
- [91] M. N. Ali, Q. D. Gibson, T. Klimczuk, and R. Cava, “Noncentrosymmetric superconductor with a bulk three-dimensional Dirac cone gapped by strong spin-orbit coupling,” *Physical Review B*, vol. 89, no. 2, p. 020505, 2014.
- [92] C.-L. Zhang, Z. Yuan, G. Bian, S.-Y. Xu, X. Zhang, M. Z. Hasan, and S. Jia, “Superconducting properties in single crystals of the topological nodal semimetal PbTaSe_2 ,” *Physical Review B*, vol. 93, no. 5, p. 054520, 2016.
- [93] A. Cameron, R. Cubitt, C. Dewhurst, and D. Inosov, “Study of the vortex lattice in the noncentrosymmetric superconductor PbTaSe_2 .” doi:10.5291/ILL-DATA.5-42-513, 2020. Institut Laue-Langevin (ILL).
- [94] L. M. Schoop, L. S. Xie, R. Chen, Q. D. Gibson, S. H. Lapidus, I. Kimchi, M. Hirschberger, N. Haldolaarachchige, M. N. Ali, C. A. Belvin, *et al.*, “Dirac metal to topological metal transition at a structural phase change in Au_2Pb and prediction of

- z_2 topology for the superconductor,” *Physical Review B*, vol. 91, no. 21, p. 214517, 2015.
- [95] Y. Xing, H. Wang, C.-K. Li, X. Zhang, J. Liu, Y. Zhang, J. Luo, Z. Wang, Y. Wang, L. Ling, *et al.*, “Superconductivity in topologically nontrivial material Au_2Pb ,” *npj Quantum Materials*, vol. 1, no. 1, pp. 1–8, 2016.
- [96] E. Campillo, A. Alshemi, E. Blackburn, R. Cubitt, E. M. Forgan, I. Guillamón, L. Shen, H. Suderow, and D. M. Vasiukov, “Vortex lattice study of Au_2Pb , a candidate topological superconductor.” doi:10.5291/ILL-DATA.5-42-520, 2020. Institut Laue-Langevin (ILL).
- [97] E. Herrera, I. Guillamón, J. A. Galvis, A. Correa, A. Fente, R. F. Lucas, F. J. Mompeán, M. García-Hernández, S. Vieira, J.-P. Brison, *et al.*, “Magnetic field dependence of the density of states in the multiband superconductor $\beta\text{-Bi}_2\text{Pd}$,” *Physical Review B*, vol. 92, no. 5, p. 054507, 2015.
- [98] J. Kačmarčík, Z. Pribulová, T. Samuely, P. Szabó, V. Cambel, J. Šoltýs, E. Herrera, H. Suderow, A. Correa-Orellana, D. Prabhakaran, *et al.*, “Single-gap superconductivity in $\beta\text{-Bi}_2\text{Pd}$,” *Physical Review B*, vol. 93, no. 14, p. 144502, 2016.
- [99] K. Iwaya, Y. Kohsaka, K. Okawa, T. Machida, M. Bahramy, T. Hanaguri, and T. Sasagawa, “Full-gap superconductivity in spin-polarised surface states of topological semimetal $\beta\text{-PdBi}_2$,” *Nature Communications*, vol. 8, no. 1, pp. 1–7, 2017.
- [100] Y.-F. Lv, W.-L. Wang, Y.-M. Zhang, H. Ding, W. Li, L. Wang, K. He, C.-L. Song, X.-C. Ma, and Q.-K. Xue, “Experimental signature of topological superconductivity and Majorana zero modes on $\beta\text{-Bi}_2\text{Pd}$ thin films,” *Science Bulletin*, vol. 62, no. 12, pp. 852–856, 2017.
- [101] M. Laver and E. M. Forgan, “Magnetic flux lines in type-II superconductors and the ‘hairy ball’ theorem,” *Nature Communications*, vol. 1, no. 1, pp. 1–4, 2010.
- [102] E. Herrera, I. Guillamón, J. Galvis, A. Correa, A. Fente, S. Vieira, H. Suderow, A. Y. Martynovich, and V. G. Kogan, “Subsurface bending and reorientation of

tilted vortex lattices in bulk isotropic superconductors due to Coulomb-like repulsion at the surface,” *Physical Review B*, vol. 96, no. 18, p. 184502, 2017.

- [103] P. Biswas, D. Mazzone, R. Sibille, E. Pomjakushina, K. Conder, H. Luetkens, C. Baines, J. Gavilano, M. Kenzelmann, A. Amato, *et al.*, “Fully gapped superconductivity in the topological superconductor β -PdBi₂,” *Physical Review B*, vol. 93, no. 22, p. 220504, 2016.



ISBN 978-91-8039-207-5
Synchrotron Radiation Research Division
Department of Physics
Faculty of Science
Lund University

